A Robust Fibre Laser System for Electro-Optic Electron Bunch Profile Measurements at FLASH

Dissertation

zur Erlangung des Doktorgrades
des Fachbereichs Physik
der Universität Hamburg

vorgelegt von

Laurens-Georg Wissmann
aus Bielefeld

Hamburg

2012

Gutachter der Dissertation	PD Dr. Bernhard Schmidt Prof. Dr. Günter Huber
Gutachter der Disputation	PD Dr. Bernhardt Schmidt Dr. Jens Osterhoff
Vorsitzender des Prüfungsausschusses	Dr. Georg Steinbrück
Vorsitzender des Promotionsausschusses	Prof. Dr. Peter Hauschildt
Dekan der Fakultät für Mathematik, Informatik und Naturwissenschaften	Prof. Dr. Heinrich Graener

Abstract

For the electro-optic measurement of electron bunch profiles at FLASH a robust ytterbium doped fibre laser (YDFL) system has been developped consisting of a laser oscillator and a two-staged amplifier. The oscillator is designed to meet the specifications of high reliability and low noise operation. The amplifier makes use of tailored nonlinearity to enhance the spectral bandwidth of the output laser pulses. Active repetition rate control enables sub-picosecond synchronisation of the laser to the accelerator reference RF. Using a two-stage gating scheme the output pulse train repetition rate is adopted to the accelerator repetition rate. An experimental site used for electro-optic electron bunch diagnostics has been redesigned to support single-shot bunch profile measurements based on spectral decoding. An exisiting bunch profile monitor with a similar laser system was upgraded and electro-optic bunch profile measurements were conducted, allowing for a comparison with measurements done with other longitudinal electron bunch diagnostics and with former measurements.

Ytterbium fibre laser, electro-optic effect, longitudinal electron bunch diagnostic, linear accelerator, FLASH

Zusammenfassung

Für die elektro-optische Messung der Ladungsverteilung von Elektronenpaketen bei FLASH wurde ein Ytterbium-dotiertes Faserlaser-System bestehend aus einem Oszillator und einem zweistufigen Verstärker gebaut und in Betrieb genommen. Das Design des Oszillators wurde auf einen zuverlässigen Betrieb und sub-picosekunden-genaue Synchronisation hin optimiert. Der Verstärker nutzt kontrolliert auftretende Nichtlinearitäten zur Verbreiterung des optischen Spektrums. Eine aktive Regelung der Pulswiederhohlrate des Oszillators ermöglicht eine phasenstarre Kopplung desselben an die Referenzfrequenz des Beschleunigers. Mithilfe eines zweistufigen Pulswählverfahrens kann die Pulswiederhohlrate des Lasersystems auf die Wiederhohlrate des Beschleunigers angepasst werden. Eine Experimentierstation für elektro-optische Strahldiagnose wurde umgebaut, um spektral dekodierte Einzelschussmessungen zu ermöglichen. Ein zweiter Strahlmonitor mit einem ähnlichen Lasersystem wurde erweitert, mit dem elektro-optische Messungen an Elektronenpaketen durchgeführt wurden, die mit anderen Messmethoden der longitudinalen Diagnostik und auch älteren Messungen verglichen werden können.

Ytterbium-Faserlaser, Pockelseffekt, Elektro-optische Strahldiagnose, Longitudinales Ladungsprofil, Linearbeschleuniger, FLASH, ultrakurze Elektronenpakete

Contents

1 Introduction **3**

2 Fundamental Concepts **7**

2.1 Light in Waveguides 7

2.1.1 Concept of a Waveguide 8

2.1.2 The Wave Equation 9

2.1.3 Transversal Fibre Modes 10

2.1.4 Derivation of the Nonlinear Schrödinger Equation 13

2.1.5 Applying the Nonlinear Schrödinger Equation 16

2.1.6 Dispersion and Chirp 18

2.1.7 Self-Phase Modulation (SPM) 20

2.1.8 Cross Phase Modulation (XPM) 22

2.2 Rare Earth doped Fibre Lasers 23

2.2.1 Two Pages of Fibre Laser History 23

2.2.2 Laser Basics 24

2.2.3 Ytterbium as Active Medium 25

2.2.4 Amplification and Gain 27

2.2.5 Fibre Laser 28

2.2.6 Dispersion Management 29

2.2.7 Mode Locking 30

2.2.8 Nonlinear Polarisation Evolution 32

2.2.9 Multipulsing 32

2.2.10 Laser Noise 33

2.3 Electro-Optic Electron Bunch Detection 35

2.3.1 Electric Field of a Relativistic Bunch 35

2.3.2 Birefringence 37

2.3.3 Pockels Effect . . . 39
2.3.4 Measurement Geometry . . . 41
2.3.5 Propagation in a Crystal . . . 43
2.3.6 EO Techniques . . . 49
2.3.7 Setups for Electro Optic Detection . . . 52

3 The FLASH Accelerator 57
3.1 The Linear Accelerator . . . 57
3.1.1 The Electron Gun . . . 57
3.1.2 Accelerating Modules . . . 58
3.1.3 Bunch Compression . . . 59
3.1.4 3.9 GHz Module . . . 60
3.1.5 SASE process . . . 61
3.1.6 Timing of the Bunches . . . 62
3.2 Longitudinal Diagnostics . . . 64
3.2.1 Transverse Deflecting Structure . . . 64
3.2.2 Beam Compression Monitors . . . 66
3.2.3 CTR Spectroscopy . . . 67
3.2.4 Electro-Optical Devices . . . 68

4 Experimental Setup 71
4.1 Ytterbium Doped Fibre Laser System . . . 71
4.1.1 Oscillator . . . 71
4.1.2 Synchronisation . . . 76
4.1.3 Amplifier and Gating . . . 78
4.2 EO at 140 m . . . 83
4.2.1 The Laser Transfer Line . . . 83
4.2.2 Setup in the Tunnel and the Vacuum Chamber . . . 84
4.2.3 Readout and Temporal Overlap . . . 86
4.3 EO at BC2 . . . 88
4.3.1 General design . . . 88
4.3.2 Laser system . . . 89
4.3.3 The Electro-Optic Frontend . . . 90
4.3.4 Timing Overlap and Triggering . . . 92

5 Characterisation of the YDFL System **95**
5.1 Oscillator 95
5.1.1 Starting Up the Oscillator 95
5.1.2 Modelock Search 96
5.1.3 Pulsed Operation 98
5.1.4 Noise Performance of the YDFL 103
5.1.5 Long Time Stability 107
5.2 Amplifier Stages 111
5.2.1 Shot-to-Shot Fluctuations 113
5.2.2 Spectral Bandwidth 116
5.2.3 Spectrum Features 117
5.2.4 Amplifier Operation Settings 119

6 EO Measurements **121**
6.1 EO at 140 m 121
6.2 EO at BC2 126
6.2.1 Time Calibration 126
6.2.2 Low Charge Ability 127
6.2.3 Electron Bunch Profile Measurements 128

7 Summary and Outlook **135**

Chapter 1

Introduction

Optical lasers have started a technical revolution in the last five decades. From micromachining and laser welding to optical data networks, from atom traps to inertia fusion - lasers play a key role. Different developments have taken place since the advent of the laser in 1960: More different laser media were found, providing access to an ever larger wavelength range. Pulsed lasers were invented, reaching for higher peak powers in ever shorter times. Since the realisation of modelocked lasers pulse durations on the order of ten fs (1 fs $=10^{-15}$ s) were available, and with the technique of high harmonic generation pulse durations in the attosecond range (1 as = 10^{-18} s) have been realised. Another line of development has followed the industrial demands for a high reliability of lasers. Though of inferior performance in terms of pulse duration, the environmental stability and excellent beam quality make fibre lasers a valuable alternative to bulk-optic solid state lasers especially for cw operation. Pulsed fibre lasers have become of major interest due to their application in optical data networks which lead to drastically increasing data transmission rates in long-haul telecommunication networks over the last two decades which in turn lead to a price decline of fibre laser components.

However not directly accessible with conventional lasers is the wavelength range extending from the deep UV to shorter wavelengths as no appropriate gain media exist. High harmonic generation suffers from low efficiency. For the deep UV and soft x-ray region, highest brilliance (photons per time, solid angle and relative bandwidth) is achieved with accelerator based light sources. These fourth generation light sources rely on highly relativistic, short electron

bunches that are guided through an undulator, a magnetic structure forcing the electron bunch on a wavelike trajectory. The electron bunch starts to emit synchroton radiation at each bend according to the undulator design wavelength which induces an energy modulation on the electron bunch (microbunching). This leads to a coherent emission of light pulses with a high peak brilliance and a tunable wavelength depending on the undulator design and the electron bunch energy. This self-enhancing process is called SASE (Self Amplification of Spontaneous Emission).

FLASH, the free-electron laser at Hamburg, is such a high-gain SASE-FEL where the light pulses are produced and amplified in a single pass through the undulator. It is capable of producing light pulses with a central wavelength of 4.12 nm, an average pulse energy of 70 μJ and a duration of tens of femtoseconds. High-quality, compressed electron bunches with a typical length of ≈ 100 fs and a peak current of more than 1 kA with minimal emittance are needed. This challenging task can only be fulfilled with linear accelerators. Well designed diagnostics are needed to set up the accelerator for SASE conditions. The most precise longitudinal diagnostic tool in use at FLASH for several years by now is the transverse deflecting structure (TDS) which enables the measurement of electron bunches as short as 25 fs. However, it is desirable to have single-shot, non-invasive electron bunch diagnostics at one's disposal. Such a diagnostic device can be build utilising the electro-optic effect which is the induced birefringence in an optically active crystal by an external electric field.

Former electro-optic bunch profile measurements successfully reconstructed electron bunches profiles as short as 60 fs with the single-shot technique of electro-optic temporal decoding (EOTD) [75]. However, EOTD requires the use of a large-scale, mJ class fs laser system. A different approach was chosen to design a reliably working, parasitic single-shot electron bunch monitor deploying the technique of electro-optic spectral decoding (EOSD) [12]. The laser pulses used for EOSD need to have a large optical bandwidth while the actual pulse duration is not of cardinal interest which makes fibre lasers a candidate for this task.

In this thesis, an ytterbium-doped fibre laser system was built and comissioned that fullfills the specifications of pulse energy, spectral bandwidth, low

noise operation, and reliability, starting from a prototype designed earlier [83]. The oscillator was designed to allow for long-time synchronisation to the accelerators reference frequency. A two-stage amplifier design including pulse pickers enables a variety of output repetition rates and pulse durations to accomodate different electro-optic setups. Furthermore electron bunch profile measurements using the already existing, upgraded electron bunch monitor downstream the first bunch compressor have been conducted.

This thesis is structured as follows: A chapter on the fundamental concepts covers the laser pulse propagation in optical fibres, gives some information about rare-earth fibre lasers with an emphasis on the actual system presented in this thesis, and the electro-optic electron bunch detection. The next chapter deals with FLASH and the longitudinal diagnostics used in the accelerator. Then the experimental setup of the laser system and the two electro-optic measurent stations at FLASH is delineated, followed by a chapter on the characterisation of the laser system and a chapter on electro-optic measurements at FLASH. To conclude, a summary and an outlook are given.

Chapter 2

Fundamental Concepts

This chapter is meant to provide a basic understanding of the theoretical background of the laser system built and the electron bunch diagnostic scheme used in this thesis. In the first part the technical realisation of a lightwave guide is described and the propagation of light pulses in optical fibres is discussed. The linear and nonlinear effects occuring in fibres are introduced. The second part deals with rare earth fibre lasers, with a strong emphasis on ytterbium doped fibre lasers including the mechanism of pulse formation. The third part is dedicated to the Pockels effect and its application to electron bunch analysis which is the subject of this thesis. Also different experimental realisations are introduced here.

2.1 Light in Waveguides

To provide a sound base for the discussion of the nonlinear effects that occur when a short pulse travels through an optical fibre, a general propagation equation is derived (called the Nonlinear Schrödinger Equation, NLS) from the wave equation that is obtained from the Maxwell equations. Then, disregarding nonlinearities in the first place, the pulse evolution governed by the chromatic dispersion is treated, and the concept of chirped pulses is introduced. As a second step, the self-phase modulation (SPM) as the most important nonlinear effect occuring in this thesis is treated. The effect of cross-phase modulation (XPM) is also discussed. All considerations made in this section are based on [4] unless otherwise noted.

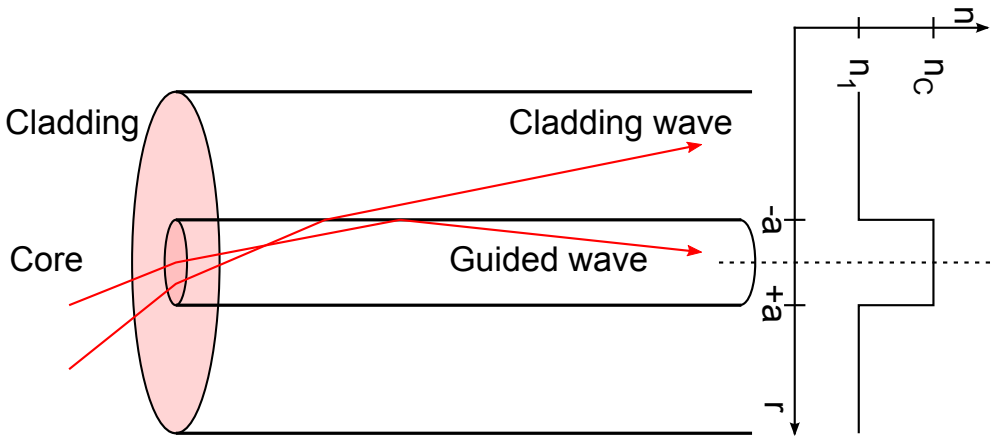

Figure 2.1: Sketch of a step-index fibre. Only the core and the cladding are shown, coating and jacket follow outwards for fibre protection. r: radius, a: core radius, n: index of refraction, n_1: ...of the cladding, n_C: ...of the core. Cladding waves are highly damped, only the guided wave is transmitted.

2.1.1 Concept of a Waveguide

An optical waveguide relies on the total internal reflection of a light wave on the boundary layer of a fibre core to a cladding that has a different index of refraction (see fig. 2.1). The core radius a and the difference of the indices of refraction of the core n_C and the cladding n_1 define the angle under which light can be coupled into the fibre (the numerical aperture, NA). Light that is coupled into the fibre under a larger angle will leave the core and become a cladding wave which is highly damped. Only the guided wave is transmitted over a considerable distance. Around the cladding a coating and a jacket follow for protection. Fibres made from fused silica - the industry standard - have losses of lower than 0.5 dB/km for light of a wavelength of 1.55 µm. This loss is limited by the fundamental Rayleigh (material) scattering process. There is a multiplicity of different fibres availabe. Among these, graded-index fibres are used for multimode (MM) fibres allowing guidance for light of different wavelengths. Single-mode (SM) fibres only transmit the fundamental mode of light of the design wavelength (see 2.1.3). Polarisation maintaining (PM) fibres allow for the transmittion of a certain polarisation state. Furthermore, several kinds of doped fibres have been created to realise active elements such as amplifiers giving way to all-fibre lasers.

2.1.2 The Wave Equation

Light is an electro-magnetic wave, the starting point for all considerations in the chapter are the Maxwell equations, given in their differential form, with the usual variable names, and the material equations:

$$\nabla \cdot \mathbf{D} = \rho \tag{2.1a}$$

$$\nabla \cdot \mathbf{B} = 0 \tag{2.1b}$$

$$\nabla \times \mathbf{E} = -\frac{\partial \mathbf{B}}{\partial t} \tag{2.1c}$$

$$\nabla \times \mathbf{H} = \mathbf{j} + \frac{\partial \mathbf{D}}{\partial t} \tag{2.1d}$$

$$\mathbf{D} = \epsilon_0 \mathbf{E} + \mathbf{P} \tag{2.1e}$$

$$\mathbf{B} = \mu_0 \mathbf{H} + \mathbf{M} \tag{2.1f}$$

Here, $\mathbf{P}$ stands for the electric polarisation, $\mathbf{M}$ for the magnetisation (which is zero in the case of a non-magnetisable glass fibre), and ϵ_0 and μ_0 are the electric and magnetic permeability, respectively. By taking the rotation of eq. 2.1c on both sides, replacing $\mathbf{B}$ by $\mu_0\mathbf{H}$ using the second material equation, and the rotation of $\mathbf{H}$ on the right side using eq. 2.1d with $\boldsymbol{j} = 0$, and subsequent substition of $\mathbf{D}$ using the first material equation, one arrives at

$$\nabla \times (\nabla \times \mathbf{E}) = -\mu_0\epsilon_0 \frac{\partial^2 \mathbf{E}}{\partial t^2} - \mu_0 \frac{\partial^2 \mathbf{P}}{\partial t^2}. \tag{2.2}$$

The polarisation $\mathbf{P}$ describes the response of any dielectric to electromagnetic waves and becomes nonlinear for intense electromagnetic fields. Its nonlinearity originates from an anharmonic response of the electrons bound to the atoms when an external field is applied. It can be expanded into a series to satisfy the general relation

$$\boldsymbol{P} = \epsilon_0 \big(\chi^{(1)} \cdot \boldsymbol{E} + \chi^{(2)} \vdots \boldsymbol{EE} + \chi^{(3)} \vdots \boldsymbol{EEE} + \dots \big). \tag{2.3}$$

The second-order susceptibility $\chi^{(2)}$ (a tensor of rank 2+1) is only non-zero for a medium that does not possess inversion symmetry on a molecular level (optically anisotropic media). It is responsible for effects like second harmonic generation (SHG), sum frequency generation (SFG) or the Pockels effect (the linear electro-optic effect, in distinction to the quadratic electro-optic effect or Kerr effect). Optical fibres are made of fused silica which has an inversion

centre (it is optically isotropic). As $\chi^{(2)}$ becomes zero, $\chi^{(3)}$ (a tensor of rank 3+1) needs to be considered. There are nonlinear effects resulting in the creation of new frequencies (third harmonic generation, THG, four-wave mixing, FWM, and self-steepening) which are not considered in this thesis. Through $\chi^{(3)}$ the refractive index becomes intensity dependent (named nonlinear refraction) which causes self-phase modulation (SPM, see sec. 2.1.7) or cross-phase modulation (XPM, sec. 2.1.8) which is of importance for the pulse formation in the presented laser system (see sec. 2.2.8).

To further evaluate eq. 2.2, the polarisation is split in a linear and a nonlinear part, where only $\chi^{(3)}$ is considered for the nonlinear polarisation.

$$\boldsymbol{P} = \epsilon_0\big(\chi^{(1)} \cdot \boldsymbol{E} + \chi^{(3)} \vdots \boldsymbol{EEE} + \dots\big) \approx \mathbf{P}_L + \mathbf{P}_{NL} \tag{2.4}$$

Using the general relation $\nabla \times (\nabla \times \mathbf{A}) = \nabla(\nabla \cdot \mathbf{A}) - \nabla^2\mathbf{A}$ for any vector $\mathbf{A}$ with $\nabla \cdot \mathbf{E} = 0$ in optical fibres for the electric field vector $\mathbf{E}$ and ${}^1/_c = \epsilon_0\mu_0$, c the velocity of light, we arrive at the general wave equation:

$$\nabla^2\mathbf{E} - \frac{1}{c^2}\frac{\partial^2\mathbf{E}}{\partial t^2} = \mu_0\frac{\partial^2\mathbf{P}_L}{\partial t^2} + \mu_0\frac{\partial^2\mathbf{P}_{NL}}{\partial t^2}. \tag{2.5}$$

Starting with this equation, the propagable transversal modes are considered in the next section. Having established a mode distribution, a general propagation equation will be derived.

2.1.3 Transversal Fibre Modes

The modes a fibre can sustain depend on the design parameters, namely, the core radius a and the refractive indices n_1 of the core and n_c of the cladding. Owing to the cylindric symmetry we start with a homogenised form ($\boldsymbol{P} = 0$) of the wave equation 2.5 in cylindrical coordinates (ρ, ϕ, z) in frequency space.

$$\frac{\partial^2\tilde{\boldsymbol{E}}}{\partial\rho^2} + \frac{1}{\rho}\frac{\partial\tilde{\boldsymbol{E}}}{\partial\rho} + \frac{1}{\rho^2}\frac{\partial^2\tilde{\boldsymbol{E}}}{\partial\phi^2} + \frac{\partial^2\tilde{\boldsymbol{E}}}{\partial z^2} + n^2k_0^2\tilde{\boldsymbol{E}} = 0 \tag{2.6}$$

Here, k_0 denotes the vacuum wave number $k_0 = \omega/c_0 = 2\pi/\lambda_0$ and $\tilde{\boldsymbol{E}}$ is the Fourier transform of the electric field according to

$$\boldsymbol{E}(\boldsymbol{r}, t) = \frac{1}{2\pi}\int_{-\infty}^{\infty}\tilde{\boldsymbol{E}}(\boldsymbol{r}, \omega)\exp(-i\omega t)\mathrm{d}\omega. \tag{2.7}$$

And similar for $\boldsymbol{H}(\boldsymbol{r},t)$. As both $\boldsymbol{H}$ and $\boldsymbol{E}$ satisfy the Maxwell equations 2.1a-2.1d, only two components are independent ($\tilde{E}_z$ and $\tilde{H}_z$, the longitudinal components of the electric and the magnetic field are taken), and the wave equation is solved by separation of variables

$$\tilde{E}_z(r,\omega) = A(\omega)F(\rho)\exp(im\phi)\exp(i\beta z). \tag{2.8}$$

with A only depending on the frequency, $\beta = \beta(\omega)$ the propagation constant, m an integer, and $F(\rho)$ a solution to

$$\frac{dF}{d\rho^2} + \frac{1}{\rho}\frac{dF}{d\rho} + \left(n^2k_0^2 - \beta^2 - \frac{m^2}{\rho^2}\right)F = 0, \tag{2.9}$$

where n is the refractive index n_c for $\rho > a$ and n_1 for $\rho < a$. A physically meaningful solution to this is found in the Bessel function $F(\rho) = J_m(\sqrt{(n_1^2k_0^2 - \beta^2)}\,\rho)$ in the core and an exponentially decaying modified Bessel function $F(\rho) = K_m(\sqrt{(\beta^2 - n_c^2k_0^2)}\,\rho)$ in the cladding. With the boundary conditions that $\tilde{\boldsymbol{E}}$ and $\tilde{\boldsymbol{H}}$ need to be continuous at $\rho = a$ an eigenvalue equation can be formulated. It is solved by many combinations of J_m and K_m, denoted as β_{mn}, where each pair of m, n corresponds to a specific mode in the fibre. We restrict ourselves to the investigation of fibres only allowing for one mode (single-mode fibres, SMF). This fundamental mode turns out to be the HE_{11} mode which has non-zero electric field components in all three directions. Of these, either the x or y component dominates, while the z component is negligible. Single mode fibre can thus sustain two orthogonally polarised modes which are mathematically degenerate but in practice have different propagation velocities due to fibre imperfections. There are polarisation-maintaining fibres (PM) that break the symmetry purposly. If the light is polarised along the x-axis we find for the electric field of the HE_{11} fundamental mode

$$\tilde{\boldsymbol{E}}(\boldsymbol{r},\omega) = \boldsymbol{x}\left(A(\omega)F(x,y)\exp(i\beta(\omega)z)\right), \tag{2.10}$$

with the transverse component inside the core being

$$F(x,y) = J_0(\sqrt{(n_1^2k_0^2 - \beta^2)}\rho) \approx \exp(-(x^2+y^2)/w^2), \tag{2.11}$$

and exponentially decaying outside the core. The frequency dependence of the propagation constant $\beta(\omega)$ results from the variation of the refractive indices n_1 and n_c (chromatic dispersion, see 2.1.6) and the frequency dependence of

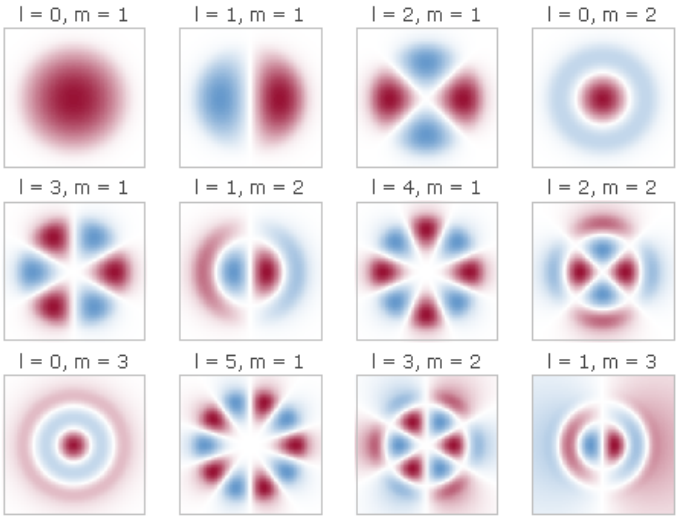

Figure 2.2: Intensity profiles of different fibre modes. Shown are superpositions of basic modes (see text) denoted as longitudinally polarised (LP) modes $\mathrm{LP}_{m,l}$ where m, l count the radial and azimuthal knots (taken from [24]). In this thesis only fibres supporting the LP_{01} mode are regarded.

$p = \sqrt{(n_1^2 k_0^2 - \beta^2)}$ (refered to as waveguide dispersion). In the case of light of the wavelength regarded in this thesis (1030 nm), the latter can be neglected: far away from the zero-dispersion wavelength (about 1.3 µm for fused silica), the chromatic dispersion always dominates. The exact solution in eq. 2.11 is approximated by a width adapted gaussian shape.

To decide whether light of a given wavelength λ propagates through a given fibre in one or more modes, the concept of the normalised frequency V is helpful.

$$V = k_0 a NA = 2\pi/\lambda a \sqrt{n_1^2 - n_c^2} \tag{2.12}$$

NA denotes the numerical aperture of the fibre core which can be expressed by the difference of the squares of the refractive indices of the core and the cladding and a is the radius of the core. A critical normalised frequency V_c can be obtained using $J_0(V_c) = 0$ with J_0 the lowest-mode Bessel function, corresponding to $V_c \approx 2.405$. If V becomes lower than V_c (the wavelength of the launched light higher than λ_c obtained using 2.12) only the HE_{11} mode can propagate through the fibre. Any other mode is below cutoff. In a given fibre that is designed to be single-mode for a specific wavelength, light with a considerably lower wavelength will propagate in different modes that overlap.

The fibre becomes a multi-mode fibre. On the other hand, V can not be made arbitrarily small as bending losses then grow even for the guided mode.

In weakly guiding fibres (with a small refractive index difference, $n_c - n_1 \approx 0.003$), the different basic modes (longitudinal and horizontal, magnetic and electric) are degenerate and linear superpositions are regarded. The fundamental mode HE_{11} found above corresponds to the LP_{01} mode, where LP stands for linearly polarised, and the subscripts $l,\ m$ count radial and azimuthal knots. In fig. 2.2, the intensity profiles of different modes are shown (taken from [24]).

2.1.4 Derivation of the Nonlinear Schrödinger Equation

The goal of this section is to derive a general equation that describes the propagation of optical pulses in a dispersive fibre, taking all important nonlinear effects into account. The starting point is eq. 2.5. Some assumptions can be made when pulses longer than 1 ps are of interest. First, pulses of this length have a peak power that does not change the refractive index by a large amount ($< 10^{-6}$). Thus, the nonlinear polarisation P_{NL} can be treated as a small perturbation to P_L. Second, these pulses do not have extremely broad optical spectra (if the field is centered around ω_0, and $\Delta\omega$ is the spectral width, $\frac{\Delta\omega}{\omega_0} << 1$) and are thus treated to be quasi-monochromatic. Third, the polarisation is assumed to stay constant over the fibre length, and fourth, the slowly varying enveloppe approximation (SVEA) is used to seperate the rapid field oscillation from the pulse enveloppe evolution resulting in

$$\boldsymbol{E}(\mathbf{r},t) = \frac{1}{2}\hat{x}\Big[\big(\underbrace{E(\mathbf{r},t)}_{\text{Slowly varying}}\ \underbrace{\exp(-i\omega_0 t)}_{\text{Rapid oscillation}}\big) + c.c.\Big]. \tag{2.13}$$

Here, $\hat{x}$ denotes the polarisation unit vector, and $E(\mathbf{r},t)$ is the slowly varying function. The polarisation components are expressed similarly by

$$\boldsymbol{P}_L(\mathbf{r},t) = \frac{1}{2}\hat{x}\left[(P_L(\mathbf{r},t)\exp(-i\omega_0 t)) + c.c.\right] \tag{2.14a}$$

$$\boldsymbol{P}_{NL}(\mathbf{r},t) = \frac{1}{2}\hat{x}\left[(P_{NL}(\mathbf{r},t)\exp(-i\omega_0 t)) + c.c.\right]. \tag{2.14b}$$

The first goal is to find expressions for P_L and P_{NL} in terms of the slowly varying function $E(\mathbf{r},t)$ (or its Fourier transform). This is done using eq. 2.4. For the nonlinear part it is assumed that the material answer to the excitation by the electric field is instantaneous which is justified for pulses of ≥ 1 ps length

(The time scale of the vibrational response in fused silica is about 60 fs). This assumption leads to

$$\boldsymbol{P}_{NL}(\mathbf{r},t) = \epsilon_0 \chi^{(3)} \vdots E(\mathbf{r},t)E(\mathbf{r},t)E(\mathbf{r},t). \tag{2.15}$$

When evaluating this using eq. 2.13 a term with the third-harmonic oscillation frequency $3\omega_0$ occurs which is omitted as this requires phase matching which generally is negligible in optical fibres. It results in

$$P_{NL}(\mathbf{r},t) \approx \epsilon_0 \epsilon_{NL} E(\mathbf{r},t) \tag{2.16}$$

where the nonlinear contribution is expressed using

$$\epsilon_{NL} = \frac{3}{4}\chi^{(3)}|E(\mathbf{r},t)|^2. \tag{2.17}$$

With this, a wave equation for the slowly varying function can be obtained. Formulated in frequency space, this wave equation can be solved by separation of variables, resulting in an equation for the mode distribution $F(x,y)$ and one for the enveloppe function $\tilde{A}(z,\omega)$:

$$\frac{\partial^2 F}{\partial x^2} + \frac{\partial^2 F}{\partial y^2} + [\epsilon(\omega)k_0^2 - \tilde{\beta}]F = 0 \tag{2.18a}$$

$$2i\beta_0 \frac{\partial \tilde{A}}{\partial z} + (\tilde{\beta}^2 - \beta_0^2)\tilde{A} = 0, \tag{2.18b}$$

where the dielectric constant $\epsilon(\omega)$ contains the linear contribution as well as the nonlinear part from eq. 2.17. The mode distribution for the fundamental mode has been found to be approximated by a gaussian in chapter 2.1.3. In a similar approach, the wave number $\tilde{\beta}$ is found by solving using the eigenvalue equation 2.18a. In a pertubative Ansatz, the mode distribution is found for $\epsilon = n^2$. The mode distribution is not changed by then including the nonlinear contribution $\epsilon = n^2 + 2n\delta n$, but the eigenvalues $\tilde{\beta}$ become

$$\tilde{\beta}(\omega) = \beta(\omega) + \Delta\beta(\omega). \tag{2.19}$$

The wavenumbers can be used to rewrite 2.18b as

$$\frac{\partial \tilde{A}}{\partial z} = i[\beta(\omega) + \Delta\beta(\omega) - \beta_0]\tilde{A}. \tag{2.20}$$

The wavenumber can be evaluated around ω_0 yielding

$$\beta(\omega) = \beta_0 + (\omega - \omega_0)\beta_1 + \frac{1}{2}(\omega - \omega_0)^2\beta_2 + \frac{1}{6}(\omega - \omega_0)^3\beta_3 + \dots \tag{2.21a}$$

$$\text{with } \beta_m = \left(\frac{d^m \beta}{d\omega^m}\right)_{\omega=\omega_0} \text{ for } m = 1, 2, \dots \ . \tag{2.21b}$$

Due to the assumption of quasi-monochromatic pulses, the expansion series can be cropped after the quadratic term. A similar expansion is used for $\Delta\omega$ where only the leading term $\Delta\beta_0$ is used for the same reason. With these simplifications, eq. 2.20 can be transformed by the fourier transformation

$$A(z,t) = \frac{1}{2\pi}\int_{-\infty}^{\infty} \tilde{A}(z,\omega-\omega_0)\exp(i(\omega-\omega_0)t)\mathrm{d}\omega \tag{2.22}$$

during which $(\omega-\omega_0)$ is replaced by $i(^{\partial}/_{\partial t})$ resulting in an equation for $A(z,t)$

$$\frac{\partial A}{\partial z} + \beta_1\frac{\partial A}{\partial t} + \frac{i\beta_2}{2}\frac{\partial^2 A}{\partial t^2} = i\Delta\beta_0 A. \tag{2.23}$$

The parameter $\Delta\beta_0$ on the right side contains the fibre losses and the nonlinear refractive index n_2 and is the leading term of the wavenumber eigenvalue adaptation from eq. 2.18b. It can be expressed by

$$\Delta\beta_0 = \frac{i\alpha}{2} + \gamma(\omega_0)|A|^2 \tag{2.24}$$

with the nonlinear parameter γ

$$\gamma(\omega_0) = \frac{n_2(\omega_0)\omega_0}{cA_{eff}}. \tag{2.25}$$

A_{eff} can be calculated from the mode distribution $F(x,y)$ and equals πw^2 if the gaussian approximation is used (with w being the width of the fitted gaussian). The term containing α describes fibre losses, while the nonlinearities caused by the intensity depending refractive index n_2 are contained in the γ parameter. Eq. 2.23 can then be rewritten as

$$\frac{\partial A}{\partial z} + \beta_1\frac{\partial A}{\partial t} + \frac{i\beta_2}{2}\frac{\partial^2 A}{\partial t^2} + \frac{\alpha}{2}A = i\gamma(\omega_0)|A|^2 A. \tag{2.26}$$

This equation describes the propagation of picosecond pulses through a single mode optical fibre including fibre losses and nonlinearities as well as chromatic dispersion effects. The pulse enveloppe travels with the group velocity ($\beta_1 = 1/v_g$) and broadens due to the group velocity dispersion (β_2 is the GVD parameter). A coordinate transformation $T = t - z/v_g = t - \beta_1 z$, translating the time coordinate into the restframe moving with the pulse, and by omitting the loss term, the Nonlinear Schrödinger Equation (NLS) is yielded:

$$i\frac{\partial A}{\partial z} + \frac{i\alpha}{2}A - \frac{\beta_2}{2}\frac{\partial^2 A}{\partial T^2} + \gamma\left|A\right|^2 A = 0. \tag{2.27}$$

The NLS permits to study third-order nonlinear effects and is suitable for the investigation of so-called optical solitons. Solitons are shape conserving solutions of the NLS that can propagate in a fibre whos GVD index is smaller than zero ($\beta_2 < 0$). The chromatic dispersion is then balanced by the nonlinear self-phase modulation. Solitons are important for telecommunication networks.

If even shorter pulses are to be investigated, an extended version of the NLS can be derived. The assumption of quasi-monochromatic pulses needs to be relaxed, and higher order terms of the wavenumber expansion will enter the equation. Also the delayed material response to the exciting electric field needs to be reconsidered, leading to Raman scattering. For pulses as short as 100 fs, the following equation known as the extended NLS can be given [4]:

$$\frac{\partial A}{\partial z}+\frac{\alpha}{2}A+\frac{i\beta_2}{2}\frac{\partial^2 A}{\partial T^2}-\frac{\beta_3}{6}\frac{\partial^3 A}{\partial T^3} = i\gamma\Big(|A|^2A+\frac{i}{\omega_0}\frac{\partial}{\partial T}(|A|^2A)-T_RA\frac{\partial|A|^2}{\partial T}\Big). \quad (2.28)$$

Where the term containing β_3 is included from the expansion of the propagation constant and governs the effect of third order dispersion (TOD). This becomes important as the bandwidth of the short pulses increases. The term proportional to $1/\omega_0$ is responsible for the effect of self-steepening. T_R denotes the first moment of the nonlinear response function and induces the nonlinear Raman frequency shift and the intrapulse Raman scattering.

2.1.5 Applying the Nonlinear Schrödinger Equation

It can be useful to focus on one aspect of the pulse propagation in the first place and then broaden the scope successively. For an estimation which effects are important in a given setup, length scales according to the single terms in eq. 2.27 can be defined. By defining a time scale normalised to the width of the input pulse T_0 according to

$$\tau = \frac{T}{T_0} = \frac{t - z/v_g}{T_0} \quad (2.29)$$

and introducing a normalised amplitude $U(z,\tau)$

$$A(z,\tau) = \sqrt{P_0}\exp(-\alpha z/2)U(z,\tau) \quad (2.30)$$

(P_0 is the peak power of the pulse) equation 2.27 can be rewritten as

$$i\frac{\partial U}{\partial z} = \frac{\mathrm{sgn}(\beta_2)}{2L_D}\frac{\partial^2 U}{\partial \tau^2} - \frac{\exp(-\alpha z)}{L_{NL}}|U|^2U. \quad (2.31)$$

Here, $\mathrm{sgn}(\beta_2) = \pm 1$ depending on the sign of the GVD parameter. Also the dispersion length L_D and the nonlinear length L_{NL} have been introduced:

$$L_D = \frac{T_0^2}{|\beta_2|}, \qquad L_{NL} = \frac{1}{\gamma P_0}. \tag{2.32}$$

With these length scales, an estimation can be made which effects govern the pulse evolution in the fibre of length L. Four different cases have to be considered:

1. $L << L_D$ and $L << L_{NL}$: In this regime, neither an influence of the dispersion nor of the self-phase modulation has to be considered. The pulse maintains its shape while it propagates through the fibre. This is the case for long pulses with a low peak power ($T_0 > 100$ ps, $P_0 < 1$ mW).

2. $L \approx L_D$ and $L << L_{NL}$: In this regime, the effects of group velocity dispersion (GVD) govern the pulse evolution. The second term on the right side of eq. 2.31 can be neglected. A detailed study on this case can be found in the next section, as the GVD parameter at the considered wavelengths of 1030 nm is generally larger than at wavelengths used for telecommunication purposes (around 1550 nm). This regime is encountered for pulses of low peak power ($P_0 << 1$ W) but with a considerable spectral bandwidth corresponding to pulse durations around 1 ps.

3. $L << L_D$ and $L \approx L_{NL}$: If the launched pulses are rather long ($T_0 >$ 100 ps), but the peak power is in the region of 1 W or more, a regime in which dispersive effects can be neglected is entered. The left term in eq. 2.31 can be neglected. The pulse propagation is governed by the effect of self-phase modulation (SPM) which leads to new spectral components. An investigation is presented in section 2.1.7.

4. $L \approx L_D$ and $L \approx L_{NL}$: Qualitatively new effects occur in the interplay of dispersion and SPM. The sign of the GVD parameter plays a key role, for $\beta_2 < 0$, the fibre can support optical solitons. These can be of help for understanding the pulse propagation in the presented stretched-pulse laser system.

2.1.6 Dispersion and Chirp

Considering the regime of dispersion governed pulse propagation ($L_D/L_{NL} = \gamma P_0 T_0^2/|\beta_2| << 1$), equation 2.27 can be modified by setting $\gamma = 0$ and introducing a normalised amplitude as in eq. 2.30 leading to

$$i\frac{\partial U}{\partial z} = \frac{\beta_2}{2}\frac{\partial^2 U}{\partial T^2}. \tag{2.33}$$

This equation can be solved by Fourier transformation. If a transform-limited pulse of gaussian shape ($U(z=0,T) = \exp(T^2/2T_0^2)$) is launched into a fibre, the amplitude $U(z,T)$ at any point in the fibre is given by

$$U(z,T) = \frac{T_0}{\sqrt{T_0^2 - i\beta_2 z}} \exp\left(-\frac{T^2}{2(T_0^2 - i\beta_2 z)}\right). \tag{2.34}$$

It can be seen from this equation that the pulse remains its gaussian shape but its width increases with z as $T_1 = T_0\sqrt{1 + z/L_D}$. Having travelled through a fibre a distance of $z = L_D$, the pulse broadens by a factor of $\sqrt{2}$. Such a situation is depicted in fig. 2.3. The broadening can be understood as the GVD acts differently on the spectral components of the laser pulse leading to a phase modulation. This phase modulation is called chirp. The spectral components travel at a slightly different speed, in a normal (material) dispersion regime (wich will only be considered in this thesis), the red components travel faster than the blue components. A time delay in the arrival of the individual frequency components leads to pulse broadening. The chirp imposed on the pulses by GVD is perfectly linear and called up-chirp or positive chirp if it results from traveling through a normal dispersion fibre. Note that the spectrum of a chirped pulse does not differ from the spectrum of the same, unchirped pulse. A chirp parameter C can be given resulting from a correction in the time-bandwidth product according to $\Delta\omega = \sqrt{(1+C^2)}/T_0$. If the spectral bandwidth $\Delta\omega$ and the pulse width T_0 are separately measured, the chirp can be calculated. Considering the launch of chirped pulses in a fibre of length z in a second step, the amplitude can be written as

$$U(z=0,T) = \exp\left(-\frac{1+iC}{2}\frac{T^2}{T_0^2}\right) \tag{2.35}$$

with C the chirp factor. The amplitude of the pulse evolves as

$$U(z,T) = \frac{T_0}{\sqrt{T_0^2 - i\beta_2 z(1+iC)}} \exp\Big(-\frac{(1+iC)T^2}{2(T_0^2 - i\beta_2 z(1+iC))}\Big). \tag{2.36}$$

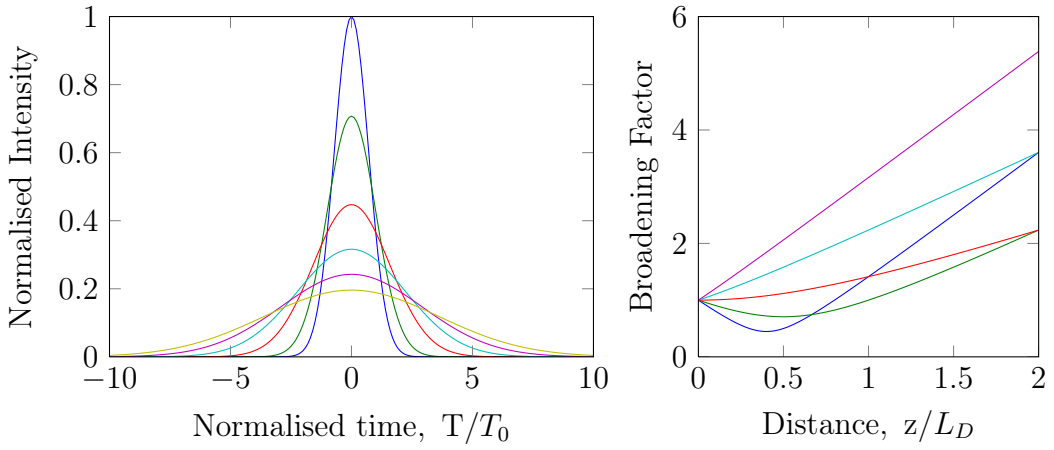

Figure 2.3: Left: Pulse shape of an initially unchirped laser pulse while propagating through a fibre (shown are six steps from $z = 0$ to $z = 5L_D$). Right: Evaluation of the broadening factor of pulses with different amounts of initial chirp. Note, a compression may occur for negative initial chirp factors (blue, green).

A broadening factor can be introduced that gives the relative pulse width of the propagating pulse to the launched pulse:

$$\frac{T_1}{T_0} = \sqrt{\left(1 + \frac{C\beta_2 z}{T_0^2}\right)^2 + \left(\frac{\beta_2 z}{T_0^2}\right)^2}. \tag{2.37}$$

For $C = 0$ the unchirped case is regained. The pulse width in the fibre now depends on the signs of β_2 and C. In this thesis only the case $\beta_2 > 0$ is of interest. There can be two different cases, $C > 0$ (positive or up-chirp) and $C < 0$ (negative or down-chirp). Starting with the first case, the broadening factor is always larger than one, the pulse broadens all along the fibre. Interesting is the latter case: If the launched pulse has a negative chirp ($C < 0$), the broadening factor may become smaller than one at some point, which corresponds to a pulse compression. Assuming the launched pulse has a purely linear chirp, the pulse will be compressed down to the transform limit. The situation is depicted in fig. 2.3, where $C = 0$ is plotted in red, the most positive chirp in purple, and the interesting negative case in blue.

For short pulses ($T_0 < 1$ ps), the next order of dispersion may be influencing the pulse propagation, as the spectral bandwidth grows (The effect of third-

order dispersion (TOD) even needs to be considered when $\beta_2 \approx 0$ for longer pulses). The term with β_3 from the extended Schrödinger equation 2.28 is used, while γ is set to zero and the same procedure as for obtaining eq. 2.33 is followed resulting in

$$i\frac{\partial U}{\partial z} = \frac{\beta_2}{2}\frac{\partial^2 U}{\partial T^2} + \frac{i\beta_3}{6}\frac{\partial^3 U}{\partial T^3}. \tag{2.38}$$

A length scale $L'_D = T_0^3/|\beta_3|$ associated with the third order dispersion can be defined and compared to L_D. For times on the order of $T_0 = 0.1$ ps, the TOD length scale becomes $L'_D \approx 10$ m. It is important to notice that the pulse shape is changed by TOD, in difference to the effect of GVD. Instead, oscillations appear at the trailing edge (for $\beta_3 > 0$) or at the leading edge (for $\beta_3 < 0$). These oscillations are deeply modulated for $\beta_2 = 0$ and quickly become less pronounced for finite values of β_2.

2.1.7 Self-Phase Modulation (SPM)

In difference to effects of second-order dispersion (GVD), the temporal shape of a pulse travelling through an optical fibre in the nonlinear regime is not altered, but additional frequency components are created changing the pulse spectrum. A pulse is in the nonlinear regime when $L << L_D$ and $L \approx L_{NL}$. Dispersive effects can be neglected here. This regime is encountered for high peak power, but not too short pulses ($T_0 > 50$ ps). Starting again with the normalised NLS equation (2.31), and discarding the β_2 term, we obtain

$$\frac{\partial U}{\partial z} = \frac{i\exp(-\alpha z)}{L_{NL}}|U|^2 U. \tag{2.39}$$

Here, as usual, α accounts for fibre losses and $L_{NL} = 1/\gamma P_0$ is the nonlinear length. Splitting the amplitude $U(L,T)$ in a part V not varying with z and a phase term, $U(L,T) = V\exp(i\phi_{NL})$, eq. 2.39 can be solved. By evaluating the phase term, we find

$$U(L,T) = U(0,T)\exp\left(i\phi_{NL}(L,T)\right) \text{ with} \tag{2.40a}$$

$$\phi_{NL}(L,T) = |U(0,T)|^2\,\frac{(1-\exp(-\alpha L)/\alpha)}{L_{NL}}. \tag{2.40b}$$

The numerator in eq. 2.40b can be thought of as an effective length $L_{eff} = (1-\exp(-\alpha L)/\alpha)$ that is shorter than L due to fibre losses. As can be seen

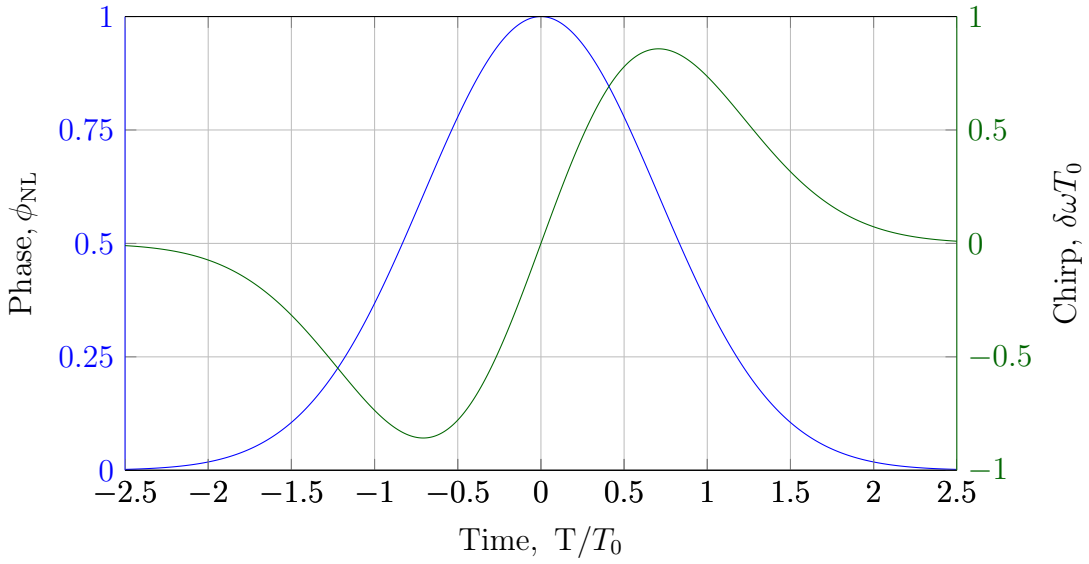

Figure 2.4: Effect of SPM on an initially unchirped gaussian pulse propagated through a fibre until $L_{NL} = L_{eff}$. In blue, the nonlinear phase shift is plotted, which continuously grows while the pulse propagates. In green, the frequency chirp (see eq. 2.41) is plotted.

from eq. 2.40a, SPM induces an intensity dependent phase shift, while the pulse shape remains constant. The phase shift grows while the pulse propagates through the fibre. The phase shift is also time dependent, leading to a variation in the instantaneous frequency of the optical field, a chirp. The difference $\delta\omega$ is given by

$$\delta\omega(T) = -\frac{\partial\phi_{NL}}{\partial T} = -\frac{L_{eff}}{L_{NL}}\frac{\partial}{\partial T}\left|U(0,T)\right|^2 . \tag{2.41}$$

The chirp leads to a continuous production of new frequency components. These broaden the spectrum of an initially unchirped pulse over its initial width. The strength of the effect depends on the exact shape of the input pulse. A flat-top pulse would not lead to new frequency components in the central part of the pulse, while at steep edges, the strong temporal variation leads to a pronounced frequency chirp. Note that the chirp is negative near the leading edge of the pulse (red shift) and positive near its trailing edge (blue shift).

The influence of SPM on the shape of the spectrum of a pulse is strongly depending on its initial shape and the accumulated nonlinear phase shift. For

a large phase shift (travelling distance z much larger than L_{NL}), the spectrum gains an oscillatory structure over the whole range. The number of peaks M depends on the maximum phase shift ϕ_{max} and is approximately given by $M \approx \phi_{max}/\pi + 1/2$. Another important influence is the initial chirp of the launched pulse. In case of a positively chirped pulse, the SPM chirp adds up to it, leading to a less strong pronounciation of the nonlinear effect. In case of a negatively chirped starting pulse, the nonlinear chirp will cancel the initial chirp at some point (at least for some parts of the pulse), leading to an enhanced oscillatory structure or even SPM pulse compression.

2.1.8 Cross Phase Modulation (XPM)

Self phase modulation describes the effect that an optical field propagating along a fibre changes its own phase by changing the refractive index of the fibre under certain conditions [37]. If more than one pulse is launched into a fibre, the phase of one field will be affected by the change of the refractive index caused by another field. This effect is referred to as cross phase modulation. Considering two copropagating pulses U_1 and U_2 of the same central wavelength, the combined nonlinear phase shift of SPM and XPM can be written to be

$$\phi_i^{NL} = \gamma L_{eff}(|U_i(0,T)|^2 + \frac{2}{3}|U_{3-i}(0,T)|^2), \text{ for } i = 1,2. \tag{2.42}$$

The first term describes SPM, the second term XPM, which is less effective by a factor of 2/3 in silica fibre. In the case of input pulses with different central wavelengths the nonlinear parameter γ is adapetd accordingly. In difference to SPM, the chirp induced through XPM can be asymmetric, leading to one-sided distortions of the optical spectrum. The effect of XPM is important for the mode lock mechanism of nonlinear polarisation evolation (see 2.2.8), where the two polarisation eigenstates of a pulse interact via XPM. In general, XPM can degrade the performance of WDM telecommunication networks, but can on the other hand be utilised for ultrafast optical switching (with switching times below 10 ps) [68].

2.2 Rare Earth doped Fibre Lasers

This section deals with lasers in general, giving a description of their short history, and then concentrates on the working principle of passively mode locked fibre lasers as such a laser has been build as part of this thesis. An emphasis is laid on the nonlinearities unique in fibre lasers and their importance for a pulsed laser operation.

2.2.1 Two Pages of Fibre Laser History

The first laser, a ruby laser, has been build by Th. Maiman in 1960 [48], only one year later, the first fibre laser cavity has been proposed [70] and build [69], using a step-index fibre doped with neodymium 3^+ ions (then still called 'Optical Maser'). Note that in 1960, fibres were extremely lossy, with losses of $\approx$ 1000 dB/km. The invention of fibres with losses below 20 dB/km in 1966 (theoretical desciption by Kao, [40], and their realisation in 1970, [52]) made them interesting for telecommunication networks, which gave this field of research a strong impulse. Nowadays the fundamental loss limits of fused silica fibres are approached (0.15 dB/km @ 1550 nm, [19]). The development of fibre lasers went on, different dopants were tested, an important milestone was the invention of longitudinal pumping offering high conversion efficiency [13]. In 1987, the erbium-doped amplifier (EDFA) was invented [55], which made purely optical long-haul telecommunication networks possible. The first ytterbium-doped fibre laser was build in 1962 [22], but compared to neodymium as active ion, ytterbium seemed less attractive. This changed as larger output powers and better conversion efficiencies became more important. The development went further bringing up fibre lasers with a high cw output (where ytterbium is attractive due to its small quantum defect) and pulsed fibre lasers for ultimate peak powers with ever shorter pulse durations (where the broad emission spectrum of ytterbium allows for a broad optical spectrum). The waveguide provides efficient pumping and good beam quality with good thermal management, making it interesting for cw laser applications in material processing, for example. Here, nonlinearities pose a threat to the beam quality and can even lead to damages. To supress nonlinearities in these systems, large mode area (LMA) fibres are used, also enabling higher powers

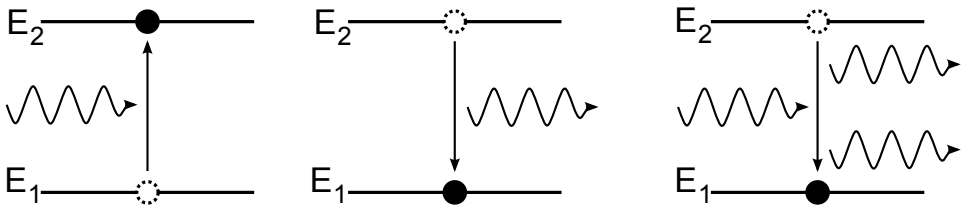

Figure 2.5: Interaction of light and matter. A photon of energy $\Delta E = E_2 - E_1 = h\nu$ can be absorbed (left), spontaneously emitted (middle) or emitted after stimulation (right). In the latter case two identical photons are emitted.

before the damage threshold is reached [45]. The wallplug efficiency is greatly enhanced by semiconductor laser diodes matched to the main absorbtion band at 975 nm and the use of double-clad fibers (DCF) [71]. Output powers of more than 1 kW and conversion efficiencies of up to 80% have been reached [39].

Pulsed fibre lasers can be classified by the mechanism that leads to pulsed laser operation. Q-switching has been proposed in 1961 [31], with which pulse durations down to the ns range can be realised. The relatively long pulses allow for high average power. Highest peak powers are achieved with very short pulses produced by mode locking - the phase locking of multiple axial modes of a laser cavity. First reported in 1964 for ruby lasers ([26] active mode locking, [56] passive mode locking), the first passively mode locked fibre laser was built in 1995 [77]. In [29] a comprehensive overview on history and theory of mode locking is given. The pulse durations today produced by ytterbium doped fibre lasers and subsequent compression external to the laser cavity are well below 50 fs [35], [87].

2.2.2 Laser Basics

In general three things are needed to build a laser: An active medium in which stimulated emission occurs, a resonator for the frequency selection and the power buildup, and a pump delivering energy to the active medium creating a population inversion (see fig. 2.6). The process of stimulated emission is one of three possible ways of photons to interact with atoms (highly nonlinear interaction such as ionisation not taken into account) [21], all three take place

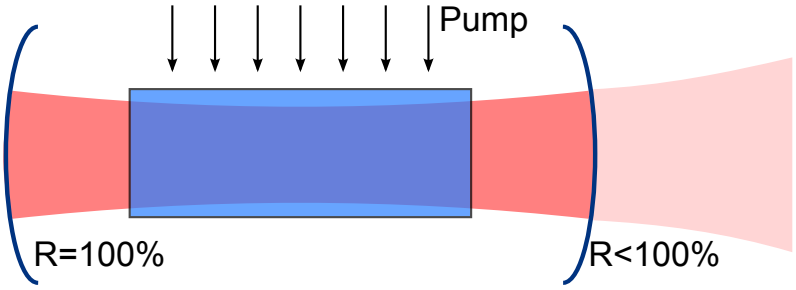

Figure 2.6: Sketch of a laser. Any laser is composed of an active medium (blue) delivering gain, a resonator, and an energy pump. Typically one resonator mirror reflects less than 100% of the incident light, thus the laser light couples out here.

in a laser: The others are spontaneous emission (which is needed to start the laser emission) and absorbtion (which is needed to absorb the pump power when optically pumped). In fig. 2.5 the three processes are sketched. The photon energy is just $\Delta E = E_2 - E_1 = h\nu$ for each process. Every medium supports a multitude of adjacent wavelengths participating in these processes. This leads to a material specific gain bandwidth. Inside the resonator light of a certain wavelength is reflected back and forth between the end mirrors. In the active medium an avalanche process is started leading to a power buildup in the laser cavity by the process of stimulated emission, if the upper energy level has a higher population than the lower one (population inversion). In a two energy level medium in thermal equilibrium, there can be no population inversion, as the population densities follow a Boltzmann distribution (see [53]). Laser media can be classified in three - and four level media; sometimes this even depends on the specific wavelengths used for the lasing process: The same medium can be of three level and/or four level nature depending on the pump and laser wavelength. These are called quasi-three level media.

2.2.3 Ytterbium as Active Medium

For the case of ytterbium ions doped into a glass host, the absorption and emission coefficients in their dependency on the wavelength have been measured by means of spectroscopy, the results are shown in figure 2.7 (taken from [62]). A strong absorption and emission band at 975 nm (A) is obvious. A broader sec-

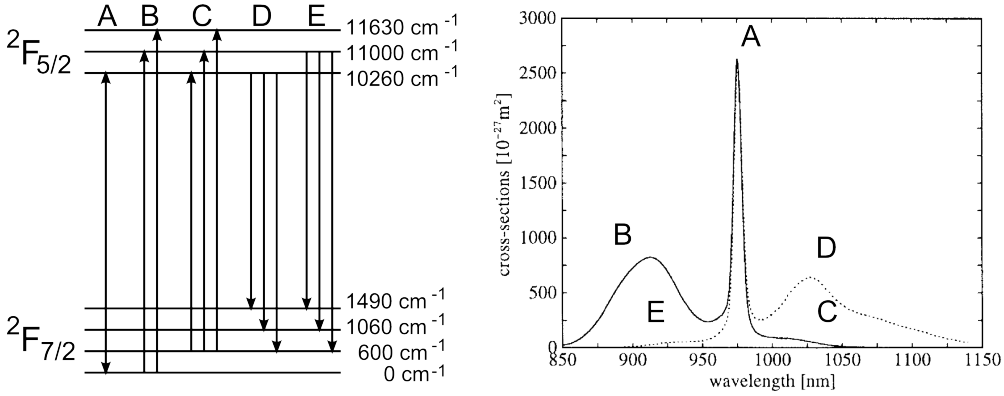

Figure 2.7: The energy levels (left) of Yb^{3+} are split by the Stark effect. The individual transitions (A-E) can be attributed to single peaks in the absorption/emission cross section spectrum (right, from [62], solid line: absorption cs, dashed line: emission cs) in germanosilicate glass. The splitting is blurred due to the glass host.

ond absorption line is around 915 nm (B), whereas a second emission peak can be seen at 1030 nm (D). The emission bandwidth extends from 980 to 1100 nm for this second emission band. The corresponding term scheme is depicted in fig. 2.7 on the left. When pumped at 915 nm (B), a four level laser process can be achieved: Electrons decay nonradiatively into the lowest level of the upper energy band, then radiate by stimulated emission and therby decay into one of the upper levels of the lower energy band (D), and then further drop down to the ground state again. When pumped at 975 nm (A), a quasi-three level laser is build. The spectrum of the emitted radiation will be correlated to the emission coefficient cross section for this process (D). The lifetime of the electrons in the lowest level of each energy band is high, while the nonradiative decay inside the same energy band is a very fast process. In the case of ytterbium, the lifetime in the lowest level of the upper energy band is on the order of 1 ms, also depending on the given fibre. An important effect is that pump light emission can occcur at 975 nm depending on the population density in the upper energy level, and that excited state reabsorption plays a non-negligible role at the 1030 nm emission wavelength; both effects need to be compensated for by a higher pump power.

2.2.4 Amplification and Gain

To describe the laser effect, a rate equation model for the population N_1 and N_2 of the lower and upper laser level, respectively, is used. The procedure follows [3]. It assumes a four-level laser system in which the upper pump state instantaneously decays into the upper laser level, it further neglects amplified spontaneous emission (ASE) and excited-state absorption as well as differences between emission and absorption cross sections. The solution for a quasi-three-level system is similar, but the calculation somewhat more difficult. Inserting cross sections, pump power, and cavity losses, it should give a threshold at which the lasing activity starts and a conversion efficiency of pump to laser light. Using the rates W_P for the transition from the lower pump level to the upper laser level and W_S for upper laser level to the ground state (ignoring the radiationless decays), the excited-state density $N_2(z,t)$ along the fibre (with the length coordinate z, $[N_2(z,t)] = 1/m^3$) is obtained:

$$\frac{\partial N_2}{\partial t} = W_P N_t - W_S N_2 - \frac{N_2}{T_1} \tag{2.43a}$$

$$W_P = \frac{\Gamma_P\ \sigma_P\ P_P}{a_P\ h\ \nu_P}, \quad W_S = \frac{\Gamma_S\ \sigma_S\ P_S}{a_S\ h\ \nu_S}, \tag{2.43b}$$

where $N_{tot} = N_t = N_1 + N_2$ is the total ion density per volume, $\Gamma_{P,S}$ are the overlap factors of pump and signal mode areas $a_{P,S}$ with the doped fibre region, respectively, and $\sigma_{P,S}$ the corresponding cross sections for the pump and signal wavelengths $\nu_{P,S}$, respectively. The fluorescence time T_1 is about 1 ms for ytterbium. Using $P'_P = P_P/P_P^{sat}$ and $P'_S = P_S/P_S^{sat}$, the steady-state solution for the above equation is given by

$$N_2 = \frac{P'_P}{1 + P'_S} N_t \tag{2.44a}$$

$$\text{with} \quad P_P^{sat} = \frac{a_P h \nu_P}{\Gamma_P \sigma_P T_1}, \ P_S^{sat} = \frac{a_S h \nu_S}{\Gamma_S \sigma_S T_1}. \tag{2.44b}$$

The population densities are needed to calculate the single-pass amplification factor $G = \exp\left(\int_L^0 g(z)\mathrm{d}z\right)$ with

$$g(z) = \sigma_S(N_2(z) - N_1(z)). \tag{2.45}$$

Below the laser threshold gain saturation can be neglected, thus $P_S/P_S^{sat} << 1$. Using an exponential decrease of the pump power along the gain fibre, $P_P(z) =$

$P_P(0)\exp(-\alpha_P z)$, where α_P stands for pump losses, eq. 2.45 can be integrated to yield the pump power needed for the threshold

$$P_P(0) = \frac{\alpha_{cav} L}{1 - \exp(-\alpha_P L)} \left(\frac{\alpha_P}{\alpha_S}\right) P_P^{sat}. \tag{2.46}$$

Here, $\alpha_P = \sigma_P N_t$ and $\alpha_S = \sigma_S N_t$ are the absorption coefficients of the pump and the laser light, respectively. The threshold condition of the gain equaling the total cavity losses has implicitly been used here. Writing the threshold power in terms of the absorbed pump power $P_{abs} = P_P(0)(1 - \exp(-\alpha_P L))$, we obtain

$$P_{th} = P_{abs} = \alpha_{cav} L \frac{\alpha_P}{\alpha_S} P_P^{sat} = \alpha_{cav} L \frac{\alpha_P \; h \; \nu_P}{\Gamma_s \; \sigma_S \; T1}. \tag{2.47}$$

Having obtained the laser threshold from the model, a few further calculations lead to the slope efficiency η_S (which is the efficiency of the power conversion above the laser threshold), defined as the ratio $\eta_S = \partial P_{out}/\partial P_{abs}$, where the output power P_{out} is the outcoupled part (reflectivity R at the output port) of the intracavity laser power $P_{out} = (1 - R)P_S = \eta_S(P_{abs} - P_{th})$. The slope efficiency is found to be

$$\eta_S = \left(\frac{1 - R}{\alpha_{cav}}\right) \left(\frac{a_S \; h \; \nu_S}{a_P \; h \; \nu_P}\right). \tag{2.48}$$

It is a measure of the efficiency with which the laser converts pump light into laser light in cw operation. The laser threshold and the slope efficiency are important characteristics of any laser oscillator.

2.2.5 Fibre Laser

A class of ring- and σ-cavity fibre lasers with a very simple setup has emerged over the last twenty years ([77],[58]). They feature a good beam quality in pulsed operation with large bandwidth, short duration pulses (compressed about 100 fs) by passive mode locking (see below). Different dopants supplying a variety of central wavelengths are in use. Under the rare earth dopants, most commonly used is erbium for lasers used in telecommunication technology, and ytterbium for high power lasers. The typical setup consists of a single-mode fibre cavity including the gain fibre with the dopant (for example any rare earth ions), a wavelength division multiplexer (WDM) to deliver the pump light to the active medium, an output coupler, a dispersion management device and a

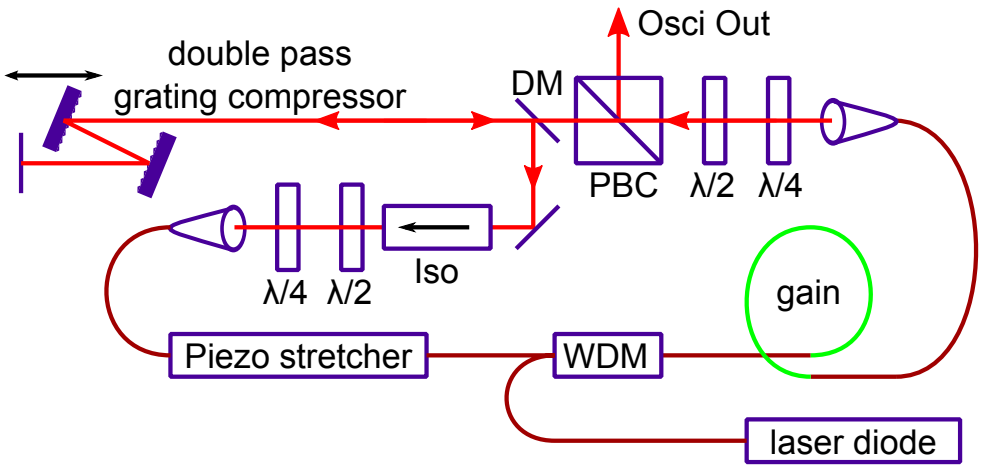

Figure 2.8: Sketch of an unidirectional fibre ring laser as used in this thesis. WDM: wavelength division multiplexer, $\lambda/4$ and $\lambda/2$: waveplate retarders, PBC: polarising beam cube, DM: dichroic mirror, Iso: isolator.

modelock initiator. Depending on the realisation of the mode locking, a modulator or some kind of saturable absorber is included. The former allows for robust mode lock starting, the latter for larger bandwidths. The setup used in this thesis is depicted in fig. 2.8. For details of the technical realisation see section 4.1.1, the characterisation of the laser oscillator can be found in sec. 5.1.

2.2.6 Dispersion Management

Depending on the dispersion that a laser pulse travelling around the cavity experiences, different pulse propagation regimes can be realised [33]. In the anomalous dispersion regime ($\beta_2 < 0$), standing waves can develop that travel around the cavity without changing their shape and width (see item four in the list in 2.1.6). These are called (optical) solitons and occur with setup-depending, finite energies at which a balancing of nonlinear chirp through SPM and dispersion occurs (for SPM see 2.1.7, for solitons see [27]). Soliton lasers have an output of characteristic sech^2-shaped pulses. They are widely build from erbium doped lasers as the main emission bandwidth of erbium (1550 nm) lies in the anomalous dispersion region for fused silica fibres. The solitons emitted by these oscillators can propagate through suited fibre over very long

distances wihtout changing their shape, resulting in a very low cross talk in data transmissions. If the central laser wavelength lies in the normal dispersion regime of fused silica as is the case for ytterbium lasers, only the net dispersion of the cavity can be controlled. This is done by means of bulk optics (grating or prism compressor, multi-pass stretched mirror) or fibre devices (dispersion compensating fibre, DCF, or specially taylored photonic crystal fibre, PCF). This leads to a breathing of the pulse while it propagates around the cavity. Considering the sketch in 2.8, this is: In the normal dispersion (i.e., fibre) part, it will go through a width minimum, and start to broaden. The nonlinear effects (SPM, XPM) will be maximal behind the gain fibre where the pulse is still relatively short but the pulses have a high energy. In the free-space part, only the grating compressor needs to be considered, which overcompensates the positive chirp of the pulse and delivers it negatively chirped into the fibre part again. There, it will shorten, until it reaches its width minimum, and the next turn begins (see fig. 2.3 in sec. 2.1.6). Lasers operating in this mode are either similariton lasers (named after the self-similar shape evolution during amplification) near zero net dispersion or, in the case of more positive net dispersion, stretched-pulse lasers. The different modelock regimes have each different advantages and drawbacks in terms of robustness against double pulsing, low noise operation, output power and output chirp, and pulse lengths [44].

2.2.7 Mode Locking

Lasers like the one depicted in fig. 2.8 deliver pulses due to the process of mode locking. In a mode locked laser adjacent longitudinal modes (with a cavity depending frequency spacing $\Delta\nu = c/L_{opt}$) add up with a fixed phase relation. The total optical field can be written as $E(t) = \sum_{m=-M}^{M} E_m \exp(i\phi_m - i\omega_m t)$, E_m, ϕ_m and ω_m denote the amplitude, phase and frequency, respectively, of a mode m out of $2M+1$ modes in total. For mode locking, the phase difference between any two adjacent modes needs to be equal, $\phi = \phi_m - \phi_{m-1}$. It can be thought of as a beat of all the contributing frequencies, the more there are, the shorter the pulse becomes. The intensity in a modelocked laser, assuming all modes have the same amplitude, can be calculated from the sum over all

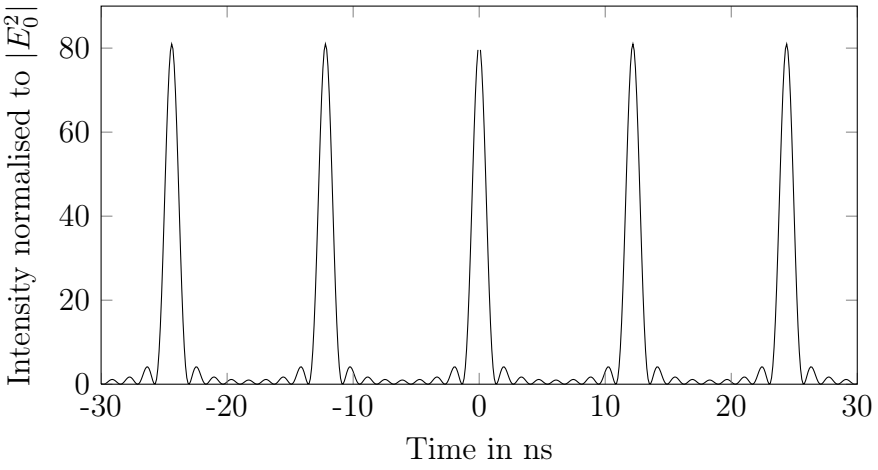

Figure 2.9: Pulse train formed when nine modes of equal amplitude $E_0 = 1$ are mode locked.

modes.

$$|E(t)|^2 = \frac{\sin^2[(2M+1)\pi\Delta\nu t + \phi/2]}{\sin^2(\pi\Delta\nu t + \phi/2)} E_0^2 \tag{2.49}$$

A plot is seen in fig. 2.9. Here, the amplitude of each mode equals one ($E_0 = 1$). The mode spacing has been set to 82 MHz, and the number of modes participating is $2M + 1 = 9$. It can be seen that the resulting pulse train has a repetition rate of just $t_R = 1/\nu$, which is the roundtrip time in the resonator. In a time domain picture, there is one pulse building up in the cavity, and every time it passes the output coupler, a part of it is emitted. The time-domain picture can also help to understand the realisation of mode locking: If an (external or internal) modulation of the cavity loss is facilited and repeated for every roundtrip, the laser will tend to emit light when the loss is low. The threshold eventually lowers for the pulsed operation, and this amplitude modulation of the optical field inside the cavity will build up until full pulsing. The time domain theory of mode locking deploys an extension of the nonlinear Schrödinger equation (NLS) 2.27 which describes the propagation of pulses through a (passive) fibre. The NLS needs to be extended by the cavity losses and an additional time-dependent loss (introduced by the modulator/saturable absorber) as well as the gain. This master equation of mode locking [28] can be solved under periodic boundary conditions yielding different pulse shapes depending on the applied nonlinear parameters.

2.2.8 Nonlinear Polarisation Evolution

An elegant way to achieve mode locking without the use of external modulators is nonlinear polarisation evolution (NPE) [9]. This process uses an intensity-dependent change of the polarisation state that occurs due to SPM and XPM (sec. 2.1.7, sec. 2.1.8, [32]). In total, a fast saturable absorber is added to the cavity, that leads to a favoring of high intensity fields propagating through the cavity. The contributing components in the laser cavity (see again fig. 2.8) are the output port (a polarising beam cube) that only transmits the horizontally polarised part of the incident light, the polarisation controllers ($\lambda/2$ and $\lambda/4$ wave plates) and the single-mode fibre itself. Looking at the the time domain again reveals the working principle. Behind the beam cube, a pulse that has come up from noise is horizontally polarised. It will be set to an arbitrary but well defined elliptical polarisation before it enters the fibre. In the fibre the polarisation will undergor changes imparted by SPM and XPM. Due to the higher intensity in the centre of the pulse the polarisation will develop differently than that of the pulse wings (the nonlinear polarisation shift depends on the intensity) [41]. Having left the fibre, the polarisation of the centre of the pulse is being set by the polarisation controllers to horizontally. Thus, the centre can pass the output port undisturbed, while the wings that have a slightly different polarisation are being reflected out to some extent. In result the pulse has been slightly shortened after one roundtrip - just what an saturable absorber does. The mode lock starts from noise when the correct wave plate setting is found. This indeed may take a while [59].

2.2.9 Multipulsing

Unfortunately, the above depicted laser cavity layout is under certain circumstances susceptible to multipulsing. This can be easiest to understand in the case of the soliton regime. A fundamental soliton has a specific amount of energy that makes it just fit to the fibre where it propagates through. The pulse energy determines the SPM that is needed to counteract the dispersion in the specific fibre. In a soliton laser, the energy of a soliton will vary (due to amplification in the gain fibre and cavity losses), but by a relatively small amount. A gain too strong will lead to wavebreaking, the soliton emits light of

continuous wavelength. If even more energy is stored in the gain fibre, there might be a second soliton propagating through the cavity - a double pulse state of operation [86], [60]. Such a double- and multipulse operation might also occur in stretched-pulse lasers, especially at high pump powers, as the startup from noise allows for this ambiguity [49]. Double pulses might be difficult to detect.

2.2.10 Laser Noise

The output pulse train of passively mode locked lasers can be remarkably stable in terms of amplitude and frequency stability [64], [72]. Good noise properties are important for the laser used in this thesis as its repetition rate must be locked to the accelerating frequency of the accelerator. The timing jitter between the bunches and the laser must be kept smaller than the length of the electron bunches (150 fs rms), leading to an integrated arrival time jitter of the free-running laser above the stabilisation cut-off frequency of less than 50 fs. The multiple mechanisms leading to noise need careful numerical simulation [30]. Noise reduction is the reason why soliton lasers are limited in terms of laser pulse energy - wavebreaking needs to be avoided. Different types of noise need to be regarded as there are coupling conditions fulfilled in different laser setups [61]. Different types of noise are discerned:

- The optical phase noise,
- The carrier-enveloppe offset phase noise which is not of interest in this thesis,
- The noise in the arrival time of the laser pulses (also called frequency noise)
- and their shape which can also vary, connected to the phase,
- where likely an amplitude variation is included.

Two different kinds of noise are regarded in this thesis. First, the frequency noise (or phase noise) leading to an arrival time jitter is regarded. The rms

timing jitter δt_{rms} in a specific interval $[f_1, f_2]$ is given by

$$\delta t_{rms} = \frac{\sqrt{2}}{2\pi f_c}\sqrt{\int_{f_1}^{f_2} \mathcal{L}_\phi}, \tag{2.50}$$

where f_c is the carrier frequency (one harmonic of the laser pulse train's fourier comb), and $\mathcal{L}_\phi$ is the single side-band timing jitter spectral density. This quantity is measured directly with a signal source-analyser (SSA) used in this thesis, see also [66]. The timing jitter spectral density describes the strength of the measured deviation of the arrival time of laser pulses from an imaginary pulse train with perfect repetition rate. It depends on the measurement bandwidth. This measurement is done for several offset frequencies from the carrier, thus yielding a spectral density.

Second, the amplitude noise itself is of interest, as depending on the electro-optic setup the amplitude noise will influence the signal to noise ratio of the EO experiment. Noise measurements are an important part of the characterisation of the oscillator. Similar to the timing jitter, a voltage spectral density $\mathcal{L}_V(f_i)$ is retrieved by a SSA whose input signal is the voltage V_0 of a low-pass filtered and amplified signal from a low-bandwidth photodiode. The relative intensity noise δ_{RIN} is the given by

$$\delta_{RIN}(f_1, f_2) = \frac{1}{V_0}\sqrt{2\int_{f_1}^{f_2} 10^{\mathcal{L}_V(f_i)/10}\mathrm{d}f_i} \tag{2.51}$$

where f_i is the offset frequency. A detailed theoretical and practical introduction to and meticulously conducted noise measurements can be found in [67].

2.3 Electro-Optic Electron Bunch Detection

This section deals with the fundamental concepts of the electro-optic effect in crystals and its application to electron bunch length measurements. It is organised as follows: First, the electric field of an electron bunch passing by at a relativistic velocity is considered. Then static birefringence is explained, and the formalism used for this is applied to the case of induced birefringence. The measurement geometry and the properties of the crystal used are considered in the next section, before EO measurement techniques and commonly applied setups are introduced.

2.3.1 Electric Field of a Relativistic Bunch

The purpose of longitudinal electron bunch diagnostics is to map the bunch charge (density) over the longitudinal time or length coordinate. Using electro-optic methods, it is the field of the relativistic electron bunch which is accessible to measurements. The electric field of a bunch of electrons is then retrieved from the field of a single electron and the longitudinal line charge density. We start with the radial electric field of a single electron at rest (the procedure described here can be found in [16], App. 1):

$$\boldsymbol{E}(\boldsymbol{r}) = \frac{q}{4\pi\epsilon_0 r^2}\frac{\boldsymbol{r}}{r} \quad \text{where} \quad \boldsymbol{r} = \begin{pmatrix} x \\ y \\ z \end{pmatrix}. \tag{2.52}$$

Here, q is the charge, ϵ_0 is the vacuum permittivity, and $\boldsymbol{r}$ the radius vector in cartesian coordinates. This spherically symmetric field needs to be Lorentz transformed by

$$\boldsymbol{E}'(\boldsymbol{r}) = \gamma(\boldsymbol{E} + \boldsymbol{v} \times \boldsymbol{B}) + (1-\gamma)\frac{\boldsymbol{E}\boldsymbol{v}}{v^2}\boldsymbol{v} \tag{2.53}$$

and

$$\boldsymbol{r}' = \begin{pmatrix} x' \\ y' \\ z' \end{pmatrix} = \begin{pmatrix} x \\ y \\ \gamma(z - v_z t) \end{pmatrix} \tag{2.54}$$

where the magnetic field $\boldsymbol{B} = 0$, $\gamma = 1/\sqrt{1 - v^2/c^2}$, and $\boldsymbol{v} = (0, 0, v_z)$. The electron moves at a speed v_z close to the speed of light c in the z direction.

The transformed field appears as

$$\boldsymbol{E}'(\boldsymbol{r}') = \frac{\gamma q}{4\pi\epsilon_0}\frac{1}{(|\boldsymbol{r}'|)^{\frac{3}{2}}}\begin{pmatrix} x \\ y \\ z - v_z t \end{pmatrix} \tag{2.55}$$

with $|\boldsymbol{r}'| = x^2 + y^2 + \gamma^2(z - v_z t)^2$ in coordinates of the non-moving system. We are only interested in the longitudinal component on the z-axis and the orthogonal r-component and thus change to cylindrical coordinates $\boldsymbol{r} = (r, \varphi, z)$ with $r = \sqrt{x^2 + y^2}$ and $\varphi = \arctan(y/x)$ and find

$$\boldsymbol{E}'(\boldsymbol{r}') = \frac{\gamma q}{4\pi\epsilon_0}\frac{1}{(|\boldsymbol{r}_r|)^{\frac{3}{2}}}\begin{pmatrix} r \\ 0 \\ -v_z t \end{pmatrix} \tag{2.56}$$

where $\boldsymbol{r} = \boldsymbol{r'} = (0, 0, 0)$ at $t = 0$. Here, $|\boldsymbol{r}_r| = x^2 + y^2 + (\gamma v_z t)^2$. If we perform a Fourier transform

$$\tilde{E}_r(r, \omega) = \mathcal{F}\{E_r(r, t)\} = \frac{1}{\sqrt{2\pi}}\int_{-\infty}^{\infty} E_r(r, t)\exp(-i\omega t)\mathrm{d}t \tag{2.57a}$$

$$E_r(r, t) = \mathcal{F}^{-1}\{\tilde{E}_r(r, \omega)\} = \frac{1}{\sqrt{2\pi}}\int_{-\infty}^{\infty} \tilde{E}_r(r, \omega)\exp(i\omega t)\mathrm{d}\omega \tag{2.57b}$$

(the back transformation is given with eq. 2.57b), the frequency components of the electron seen by an observer at $z = 0$ in a distance r can be calculated to be

$$\tilde{E}_r(r, \omega) = \frac{q\omega}{(2\pi)^{3/2}\epsilon_0\beta^2\gamma c^2}K_1\left(\frac{\omega}{\beta\gamma c}r\right). \tag{2.58}$$

Here, $\beta = v/c$ and K_1 denotes the modified Bessel function. For v approaching c, β approaches 1, and γ becomes large (in the case of FLASH, $\gamma \approx 1000$ behind the last accelerating module). The longitudinal field component can be omitted for large γ as it is smaller than the radial field components by a factor of $1/\gamma$.

The (radial) electric field $E_{r,Q}$ of a bunch of electrons is computed by folding the electric field of a single electron E_r with a line charge distribution $Q(t)$, ($[Q(t)] = 1/\mathrm{m}$), moving along the z-axis (a bunch with a negligible radial expansion is assumed) yielding

$$E_{r,Q}(r, t) = (E_r * Q)(r, t) = \int_{-\infty}^{\infty} E_r(r, t - s)Q(t)\mathrm{d}s. \tag{2.59}$$

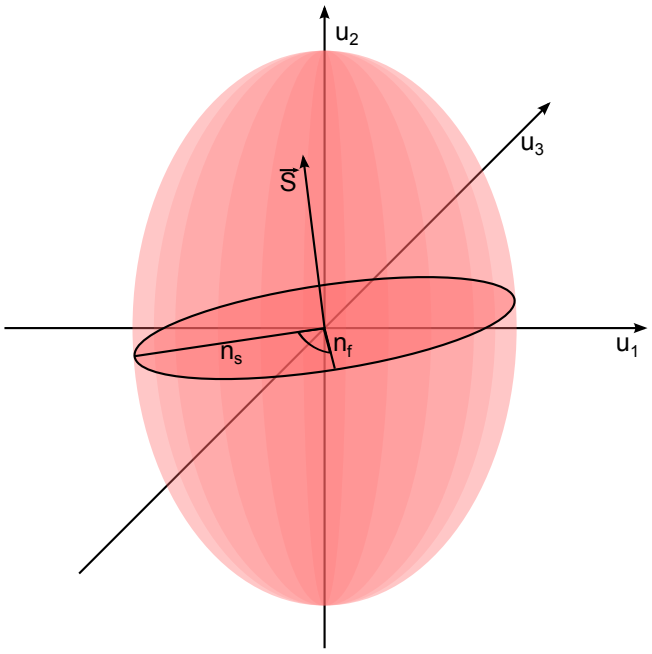

Figure 2.10: Sketch of the index ellipsoid as defined by eq. 2.65. An electromagnetic wave traversing the crystal defines an intersection plane orthogonal to its propagation direction $\vec{S}$. The resulting plane is an ellipse with two axes of length $2n_s$ and $2n_f$.

The frequency components corresponding to such a relativistic electron bunch are given by

$$\tilde{E}_{r,Q}(\omega) = \mathcal{F}\{(E_r * Q)(t)\} = \mathcal{F}\{(E_r(t))\} \cdot \mathcal{F}\{Q(t)\} \tag{2.60}$$

It can be stated that in the laboratory frame the electric field of the passing electron bunch appears to be a THz pulse with frequency components of up to a few THz. Higher frequencies stem from shorter features in the line charge distribution $Q(t)$. The chosen crystal has to handle this bandwidth.

2.3.2 Birefringence

The effect of some crystals splitting an arbitrarily polarised light wave in its two components and adding a spatial displacement between them as they propagate through it is called birefringence. It has already been described in 1669 by Rasmus Bartholin who observed it in calcite [7]. This treatment follows [75]. These crystals are called optically anisotrop. To understand this effect we start

with the material equation for the electric flux density

$$\boldsymbol{D} = \epsilon_0 \boldsymbol{E} + \boldsymbol{P} \tag{2.61}$$

where $\boldsymbol{E}$ is the electric field of the light applied to the crystal and $\boldsymbol{P}$ is the polarisation of the crystal atoms in reaction to the field. In an isotropic crystal, the field vector of $\boldsymbol{P}$ is always parallel to $\boldsymbol{E}$, leading to $\boldsymbol{D} = \epsilon_0(1 + \epsilon_r)\boldsymbol{E}$ with ϵ_r denoting the scalar permittivity of the crystal. In an anisotropic crystal the polarisation can have any orientation given by $P_i = \epsilon_0 \chi_{ij} E_j$ for each component P_i of the polarisation $\boldsymbol{P}$, where the χ_{ij} make up the susceptibility tensor (of rank 2). It is generally possible to translate into a principal axis system so that the susceptibility tensor only has nonzero entries on its diagonal, $\chi_{ij} = 0$ for $i \neq j$, so we can write eq. 2.61 as

$$D_i = \epsilon_0 \sum_j \epsilon_{ij} E_j, \tag{2.62}$$

where the permittivity tensor $\epsilon_{ij} = 1 + \chi_{ij}$ is introduced. The phase velocity of a plane electromagnetic wave in a crystal is given by $v_p = c/\sqrt{\epsilon} = c/n$ with n the index of refraction. In an optically anisotropic crystal, two orthogonal optic axes $\boldsymbol{U}_s$ and $\boldsymbol{U}_f$ with different refractive indices (n_s and n_f) are found, with 's' for slow and 'f' for fast. If we consider a linearly polarised wave entering the crystal with a polarisation parallel to one of the main axes, there will be no birefringence but a slightly different propagation time through the crystal depending on whether it enters parallel to the fast or the slow axis. If the polarised light enters the crystal with a polarisation not parallel to one of the main axes, the light will be decomposed in its two polarisation components. They propagate with different velocities through the crystal, leading to a phase shift between the two components, and thus a change of the polarisation state. To determine the indices of refraction n_s and n_f, a construction called the index ellipsoid is used. Starting from the energy density w of an electric field and using eq. 2.62, we find

$$w = \frac{1}{2}\boldsymbol{E}\boldsymbol{D} = \frac{1}{2}\epsilon_0 \sum_{i,j} E_i \epsilon_{ij} E_j, \tag{2.63}$$

or, in a coordinate system in which the permittivity tensor becomes diagonal,

$$\frac{D_1^2}{\epsilon_1} + \frac{D_2^2}{\epsilon_2} + \frac{D_3^2}{\epsilon_3} = 2\epsilon_0 w \tag{2.64}$$

where $\epsilon_i = \epsilon_{ii}$ for $i = 1, 2, 3$. The main refractive indices are $n_i = \sqrt{\epsilon_i}$. Using them and a vector $u = \boldsymbol{D}/\sqrt{2\epsilon_0 w}$, eq. 2.64 can be normalised to

$$\frac{u_1^2}{n_1^2} + \frac{u_2^2}{n_2^2} + \frac{u_3^2}{n_3^2} = 1. \tag{2.65}$$

This equation defines an ellipsoid in space (see fig. 2.10). The main axes of this index ellipsoid are parallel to the optical axes of the crystal and have a length of $2n_i$. Eq. 2.65 can be written in a vector form

$$\boldsymbol{u} \cdot \boldsymbol{\eta} \cdot \boldsymbol{u} = 1 \text{ with } \boldsymbol{\eta} = \boldsymbol{\epsilon}^{-1} = \begin{pmatrix} \frac{1}{n_1^2} & 0 & 0 \\ 0 & \frac{1}{n_2^2} & 0 \\ 0 & 0 & \frac{1}{n_3^2} \end{pmatrix}. \tag{2.66}$$

Here the impermeability tensor $\boldsymbol{\eta}$ has been introduced. A plane wave traversing the crystal defines an intersection plane orthogonal to its popagation direction $\vec{S}$ in the index ellipsoid. The intersection plane forms an ellipse with two axes that have a length of $2n_s$ and $2n_f$, respectively.

2.3.3 Pockels Effect

The considerations in the before section apply to optically anisotropic material in which a light wave always experiences birefringence due to the polarisation of the atoms in response to the optical field. This polarisation in eq. 2.61 is assumed to be linear which is valid for weak electric fields (here: low light intensities). Now, the effect of an external electric field $\boldsymbol{E}_{external}$ different from the light that is applied to the crystal is considered. In the case of a strong electric field (here, a THz wave) the Taylor expansion of $\boldsymbol{P}$ (eq. 2.3, repeated here) can be used with $\boldsymbol{E} = \boldsymbol{E}_{external}$:

$$\boldsymbol{P} = \epsilon_0 \big(\chi^{(1)} \cdot \boldsymbol{E} + \chi^{(2)} \vdots \boldsymbol{EE} + \chi^{(3)} \vdots \boldsymbol{EEE} + \dots \big). \tag{2.67}$$

Then, not only the linear term with $\chi^{(1)}$, but also the next term with the second-order susceptibility $\chi^{(2)} \cdot \boldsymbol{E}$ has to be considered. This term depends on the electric field and will lead to a change of the refractive index, and the resulting induced birefringence is called the Pockels effect. The electric field of the electron bunch traversing the electro-optic crystal has frequency components over a large bandwidth. To understand the process of induced

birefringence, it is useful to first restrict oneself to the propagation of a single-frequency THz wave in the EO crystal. Induced birefringence can occur in optically anisotropic crystals ($\chi^{(1)}$ is a tensor of rank 2) and also in optically isotropic crystals ($\chi^{(1)}$ is a scalar), i.e., with a vanishing field the crystal is not birefringent any more. The next order of nonlinear effects (the Kerr effect) caused by even stronger electric fields is not regarded in this chapter as for the applied field strengths in this thesis the components $\chi^{(3)}\vdots\boldsymbol{EEE}$ are too small (in the case of external electric fields, in the case of laser pulse propagation in fibres it is considered). The index of refraction needs to be recalculated taking the $\chi^{(2)} \cdot \boldsymbol{EE}$ part proportional to the field into account. We consider the impermeability tensor $\boldsymbol{\eta}$ which has components

$$\eta_{ij} = \eta_{ij}(0) + r_{ijk}E_k \tag{2.68}$$

when we expand around $\boldsymbol{E} = 0$ and disregard the higher orders. r_{ij} are the Pockels coefficients that characterise the strength of the Pockels effect in a given material, and the $\eta_{ij}(0)$ make up the unchanged impermeability tensor from eq. 2.66. The new components of the impermeability tensor can be used to rewrite eq. 2.66 yielding

$$\boldsymbol{u} \cdot \boldsymbol{\eta}(\boldsymbol{E}) \cdot \boldsymbol{u} = \sum_{i,j=1,2,3} \left(\epsilon^{-1}\delta_{i,j} + \sum_{k=1,2,3} r_{ijk}E_k \right) u_i u_j = 1. \tag{2.69}$$

As the $\boldsymbol{r}$ tensor is symmetric, a simplification from a tensor of rank three to a tensor of rank two can generally be made, yielding the components of the electro-optic tensor r_{ik}. Depending on the crystal used for experiments, this tensor will further simplify. In this thesis, the crystal type considered is gallium phosphide (GaP). Two features of GaP are important for the descrition of induced birefringence: Due to the zinkblende crystal structure ($\bar{4}$3m), there is only one independent entry in the electro-optic tensor ($r_{41} = r_{52} = r_{63}$). And, as the birefringence of GaP ceases when no external electric field is applied (it is optically isotropic), the diagonal components of the $\boldsymbol{\eta}(0)$ tensor are all equal to $(\frac{1}{n_0^2})$, so using eq. 2.68, equation 2.69 can be written in the form

$$\boldsymbol{u} \cdot \boldsymbol{\eta}(\boldsymbol{E}) \cdot \boldsymbol{u} = \frac{1}{n_0^2}(u_1^2 + u_2^2 + u_3^2) + 2r_{41}(E_1u_2u_3 + E_2u_3u_1 + E_3u_1u_2) = 1. \tag{2.70}$$

$$\begin{array}{l|l} (1,1) \rightarrow 1 & r_{11k} \rightarrow r_{1k} \\ (2,2) \rightarrow 2 & r_{22k} \rightarrow r_{2k} \\ (3,3) \rightarrow 3 & r_{33k} \rightarrow r_{3k} \\ (2,3) \rightarrow 4 & r_{23k} \rightarrow r_{4k} \\ (1,3) \rightarrow 5 & r_{13k} \rightarrow r_{5k} \\ (1,2) \rightarrow 6 & r_{12k} \rightarrow r_{6k} \end{array} \Bigg\| \rightarrow \boldsymbol{r} = \begin{pmatrix} 0 & 0 & 0 \\ 0 & 0 & 0 \\ 0 & 0 & 0 \\ r_{41} & 0 & 0 \\ 0 & r_{41} & 0 \\ 0 & 0 & r_{41} \end{pmatrix}$$

Table 2.1: Usual notation change for the the reduction of the electro-optic tensor of rank three to a six-by-three matrix. Due to an optically isotropic crystal considered in this thesis and crystal symmetry, only one entry is independent, and the matrix on the right is retrieved.

This equation describes the index ellipsoid of GaP with an arbitrary external electric field applied. With it, the principal indices of refraction can be retrieved which define the phase (and group) velocities.

2.3.4 Measurement Geometry

To find the index of refraction for the fast and the slow axis, the actual measurement geometry has to be considered. Only the geometry used in practice is regarded here. It leads to the strongest difference of refractive indices induced by the electric field of the electron bunch. As in the case of the natural birefringence, the eigenvalues of the $\boldsymbol{\eta}$ tensor have to be determined. In the case of the induced birefringence, the $\boldsymbol{\eta}$ tensor as defined in eq. 2.68 has to be considered. To this end, a principal axis coordinate transformation has to be performed from the laboratory system to a system where the X and Y axes lie in the intersection plane of the index ellipsoid. The incident electric field of the electron bunch $\boldsymbol{E}_{THz}$ propagates orthogonal to this plane, so the field vector lies in it, and may enclose any angle α with the X axis. It can be generally shown for crystals of zinkblende structure that the geometry leading to the strongest effect is cutting the crystal parallel to the (110)-plane [18]. In fig. 2.11 the situation is depicted. The new coordinate system has the base vectors $X = 1/\sqrt{2}[\bar{1}10]$, $Y = [001]$, $Z = 1/\sqrt{2}[1\bar{1}0]$, that is, the new coordinate system is turned around the Y axis by 45°. The electric field vector $\boldsymbol{E}_{THz}$ in

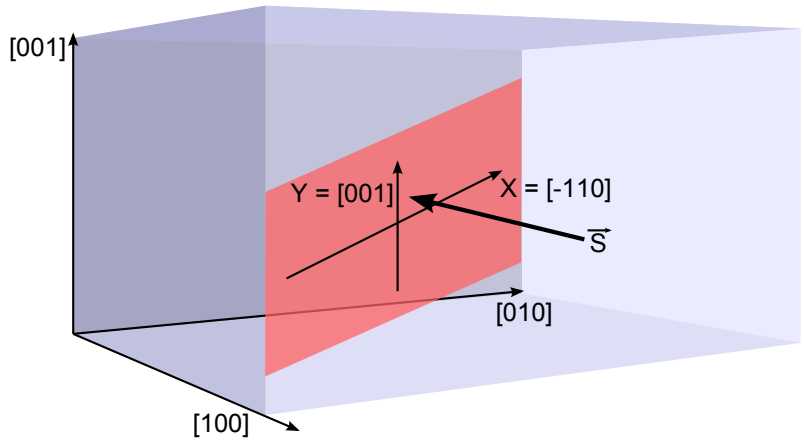

Figure 2.11: The crystals used are cut in the (110)-plane in which the new coordinates X = [-110] and Y = [001] are chosen for a principal axes transformation. The electric field vector lies in this plane, the propagation direction of the field is $\vec{S}$.

the crystal base coordinate system can be written as

$$\boldsymbol{E}_{THz} = E_{THz,0} \exp\left(-i\omega_{THz} t\right) \begin{pmatrix} -\frac{1}{\sqrt{2}} \cos\left(\alpha\right) \\ \frac{1}{\sqrt{2}} \cos\left(\alpha\right) \\ \sin\left(\alpha\right) \end{pmatrix} \tag{2.71}$$

with $E_{THz,0}$ the amplitude of the electric field and ω_{THz} the frequency of the THz field. The $\boldsymbol{\eta}$ tensor takes the form

$$\boldsymbol{\eta}(\boldsymbol{E}_{THz}) = \frac{1}{n_0^2} \begin{pmatrix} 1 & 0 & 0 \\ 0 & 1 & 0 \\ 0 & 0 & 1 \end{pmatrix} + r_{41} E_{THz} \begin{pmatrix} 0 & \sin\left(\alpha\right) & \frac{\cos\left(\alpha\right)}{\sqrt{2}} \\ \sin\left(\alpha\right) & 0 & -\frac{\cos\left(\alpha\right)}{\sqrt{2}} \\ \frac{\cos\left(\alpha\right)}{\sqrt{2}} & -\frac{\cos\left(\alpha\right)}{\sqrt{2}} & 0 \end{pmatrix}. \tag{2.72}$$

The eigenvalues $\lambda_{1,2,3}$ of $\boldsymbol{\eta}(\boldsymbol{E}_{THz})$ and the corresponding eigenvectors $\boldsymbol{U}_{1,2,3}$ can be calculated to be [75]

$$\lambda_{1,2} = \frac{1}{n_0^2} - \frac{r_{41} E_{THz}}{2} \left(\sin\left(\alpha\right) \pm \sqrt{1 + 3\cos^2\left(\alpha\right)}\right) \tag{2.73a}$$

$$\lambda_3 = \frac{1}{n_0^2} + r_{41} E_{THz} \sin\left(\alpha\right) \tag{2.73b}$$

$$\boldsymbol{U}_1 = \frac{1}{2} \sqrt{1 + \frac{\sin\left(\alpha\right)}{\sqrt{1 + 3\cos^2\left(\alpha\right)}}} \begin{pmatrix} -1 \\ 1 \\ \frac{2\sqrt{2}\cos\left(\alpha\right)}{\sqrt{1+3\cos^2\left(\alpha\right)}+\sin\left(\alpha\right)} \end{pmatrix} \tag{2.73c}$$

$$\boldsymbol{U}_2 = \frac{1}{2}\sqrt{1 - \frac{\sin(\alpha)}{\sqrt{1+3\cos^2(\alpha)}}} \begin{pmatrix} 1 \\ -1 \\ \frac{2\sqrt{2}\cos(\alpha)}{\sqrt{1+3\cos^2(\alpha)}-\sin(\alpha)} \end{pmatrix} \tag{2.73d}$$

$$\boldsymbol{U}_3 = \frac{1}{\sqrt{2}} \begin{pmatrix} -1 \\ -1 \\ 0 \end{pmatrix}. \tag{2.73e}$$

The main refractive indices are connected to the eigenvalues of $\boldsymbol{\eta}(\boldsymbol{E}_{THz})$ by $n_i = 1/\sqrt{\lambda_i}$. Using a Taylor expansion and recognising $r_{41}E_{THz} << \frac{1}{n_0^2}$, the main refractive indices become

$$n_1 = n_0 + \frac{n_0^3 r_{41} E_{THz}}{4}\left(\sin(\alpha) + \sqrt{1+3\cos^2(\alpha)}\right) \tag{2.74a}$$

$$n_2 = n_0 + \frac{n_0^3 r_{41} E_{THz}}{4}\left(\sin(\alpha) - \sqrt{1+3\cos^2(\alpha)}\right) \tag{2.74b}$$

$$n_3 = n_0 - \frac{n_0^3 r_{41} E_{THz}}{2}\sin(\alpha). \tag{2.74c}$$

The third eigenvector is parallel to the propagation direction of the THz field, while $\boldsymbol{U}_1$ and $\boldsymbol{U}_2$ lie in the (110)-plane of the crystal. The difference $n_1 - n_2$ becomes maximal for $\alpha = 0$. The phase advance Γ of one polarisation component against another of a laser pulse testing the induced birefringence is

$$\Gamma(\alpha) = \frac{\omega d}{c}(n_1 - n_2) = \frac{\omega d}{2c} n_0^3 r_{41} E_{THz}\sqrt{1+3\cos^2(\alpha)}. \tag{2.75}$$

The phase advance becomes maximal for $\alpha = 0$, which corresponds to an angle of $\phi = \pi/4$ between $\boldsymbol{U}_1$ and the X axis of the crystal coordinate system. For $\alpha = 0$, n_3 becomes unchanged. The crystals and the measurement setup used in this thesis are oriented in this fashion.

2.3.5 Propagation in a Crystal

The optimal crystal orientation ensures a maximal phase retardation produced by the Pockels effect. Beside this, the laser pulse testing the induced birefringence and the THz pulse evocing this change need to copropagate through the crystal. If the timing is correct and the two pulses enter the crystal at the same time, they still might have different velocities. The phase velocity of the THz pulse is given by the index of refraction n_{THz} in the THz range, and the group

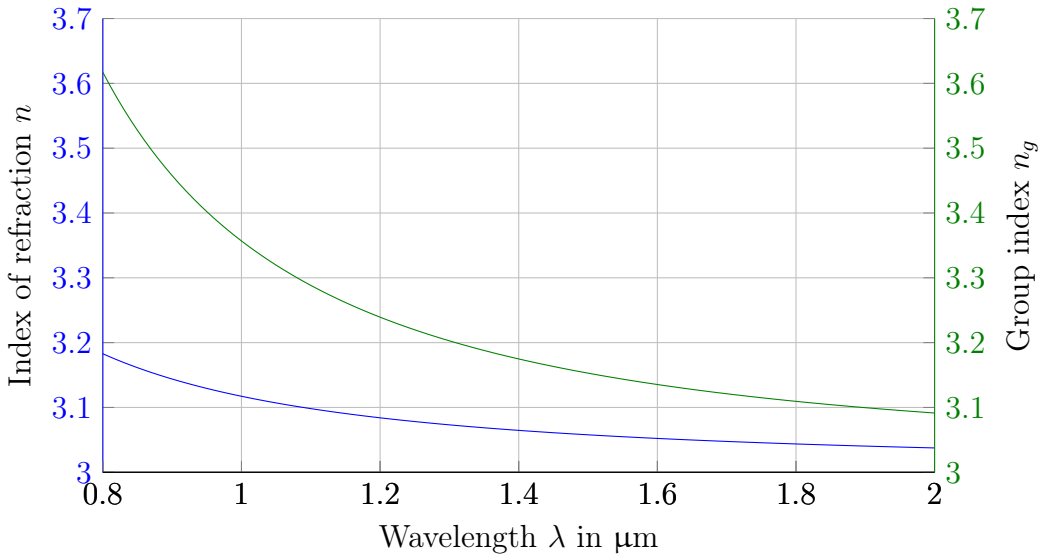

Figure 2.12: Index of refraction $n(\lambda)$ for near-infrared wavelengths as approximated by the Sellmeier equation (eq. 2.76), data taken from [8]. The group index n_g is plotted in green (eq. 2.78).

velocity of the laser pulse enveloppe is given by the group indexat the optical wavelength, n_g, which is derived from the index of refraction n_{opt}. Also the absolute value of the electro-optic coefficient r_{41} and its frequency dependency needs to be known. With the knowledge of these crystal properties an electro-optic response function can be given that characterises the overall strength of the coupling of the THz wave to the optical pulse.

The refractive index is frequency dependent as the material response to incident electric fields of varying frequency can be very different. Resonances can occur due to the coupling of the incident electromagnetic waves to the atomic kernels of the medium. In the optic region (visible light, near infrared, wavelength range starting at 400 nm), the refractive index lowers with increasing wavelength. In contrast, in the THz region it rises with increasing wavelength as the 'optic' resonances are approached. In an optical resonance (longitudinal, LO, or transversal, TO), the atoms of different kind oscillate in opposite directions on their places in the crystal lattice, while in an acoustic resonance (occuring at much lower frequencies) all atoms of the material oscillate in phase. The interaction can be thought of as a scattering process in

which the light particles excite delocalised quasiparticles, called the phonons.

In the frequency range of visible and infrared light, the frequency dependency can be described using a Sellmeier formula that approximates the measured data. The approximation formula given in [8] is used:

$$n(\lambda)^2-1 = C_1\lambda^2/(\lambda^2-C_2^2)+C_3\lambda^2/(\lambda^2-C_4^2)+C_5\lambda^2/(\lambda^2-C_6^2)+C_7\lambda^2/(\lambda^2-C_8^2) \tag{2.76}$$

with the coefficients (taken from [8])

$$\begin{aligned} C1 &= 1.390 \quad C3 = 4.131 \quad C5 = 2.570 \quad C7 = 2.056 \\ C2 &= 0.172 \quad C4 = 0.234 \quad C6 = 0.345 \quad C8 = 27.52. \end{aligned} \tag{2.77}$$

The resulting frequency dependency of the refractive index is plotted in fig. 2.12 together with the group index n_g which is defined as

$$n_g = n\left(1+\frac{\lambda}{n}\frac{\partial n}{\partial\lambda}\right)^{-1} \tag{2.78}$$

and is required for the calculation of the velocity mismatch between the THz wave and the laser pulse. For $\lambda_0 = 1030$ nm, the laser wavelength used in this thesis, we find a refractive index of $n = 3.111$ and a group index of $n_g = 3.334$. The velocity of the enveloppe of the laser pulse is defined by the group velocity $v_g = c/n_g$.

The (complex) refractive index in the THz regime can be given in a form reminding of a response function of a damped, driven harmonic oscillator with the lowest phonon frequency as its eigenfrequency and assumes the form

$$n_{THz}(f) = \sqrt{\epsilon_\infty\left(1+\frac{f_{LO}^2-f_{TO}^2}{f_{TO}^2-f^2-i\Gamma_0 f}\right)} \tag{2.79}$$

where the coefficients are

$$\epsilon_\infty = 9.075,\ f_{TO} = 11.02\ \text{THz},\ f_{LO} = 12.09\ \text{THz},\ \Gamma_0 = 0.129\ \text{THz}. \tag{2.80}$$

The approximation formula and the coefficients have been taken from [43]. A different parametrisation together with the available measurement data is found in [14], yielding similar results. Here, f_{TO} denotes the frequency of the transversal optical resonance, and f_{LO} the adjacent longitudinal optical resonance. When f approaches the resonance at f_{TO}, the denominator in eq.

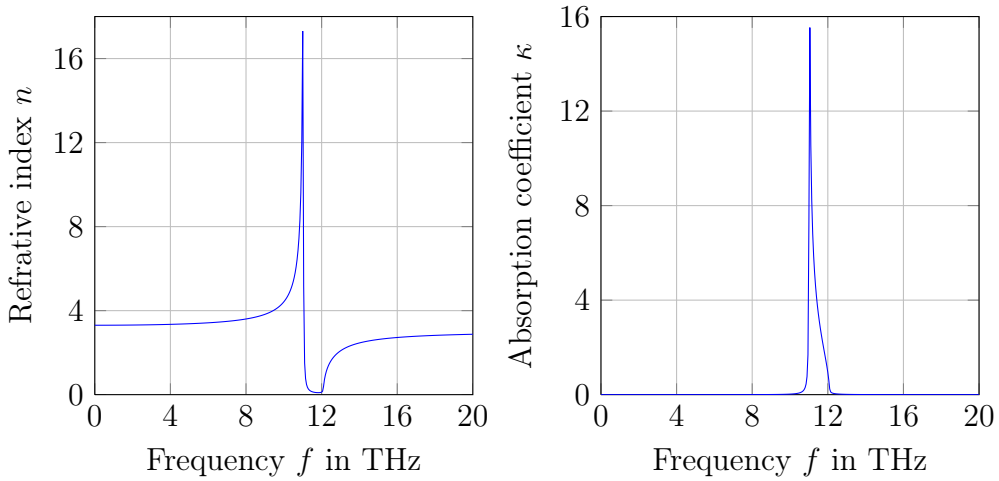

Figure 2.13: Refractive index of GaP in the THz range as calculated by eq. 2.79 (left) and absorption coefficient $\kappa(f)$. Approximation data taken from [43].

2.79 becomes purely imaginary, and Γ_0 defines the width of the resonance. The resulting dependency is plotted in fig. 2.13 where the real part of the complex index of refraction is given (the normal refractive index) and the imaginary part that is the absorption coefficient κ of a material. A similar frequency dependency as for n_{THz} is given for the electro-optic coefficient r_{41} in GaP [23]:

$$r_{41}(f) = d_E \left(1 + \frac{C f_0^2}{f_0^2 - f^2 - i\Gamma_0 f}\right) \tag{2.81}$$

With the coefficients $d_E = 1 \cdot 10^{-12}$, $C = -0.53$ as well as $\Gamma_0 = 0.129$ THz and $f_0 = f_{TO} = 11.02$ THz as above. The result can be seen in fig. 2.14. With the knowledge of the refractive index in the THz region, the phase velocity of a THz wave in the GaP crystal is given by $v_{Ph} = c/n_{THz}$ (see fig. 2.14 on the right, drawn together with the group velocity of an optical pulse with the centre wavelength of 1030 nm ($n_g(\lambda_0) = 3.334 \rightarrow v_g/c \approx 0.3$)). A response function can be defined that takes the velocity mismatch of the THz wave and the optical pulse over the crystal thickness d into account. It also contains the amplitude transmission coefficient of the THz wave into the crystal. Following [14] ([43] and [84] give a slightly different form), and using $n_{THz}(\omega)$ as the complex refractive index from eq. 2.79 and $\omega = 2\pi f$, the response function

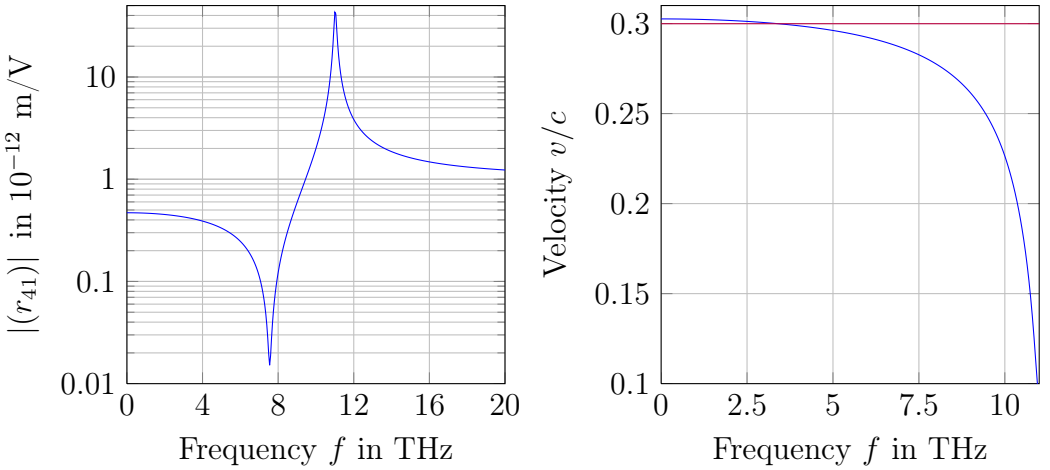

Figure 2.14: Left side: Frequency dependency of r_{41}. Right side: Frequency dependency of the phase velocity (normalised to c) in GaP (blue) together with the group velocity of an optical pulse centered around 1030 nm (purple).

can be written to be

$$G(\omega) = \frac{2}{n_{THz}(\omega) + 1} \cdot \frac{\exp\left(i\omega d(1/v_{Ph}(\omega) - v_g)/c\right) - 1}{i\omega d(1/v_{Ph}(\omega) - v_g)}, \tag{2.82}$$

where the loss term is omitted, and the group velocity is assumed to be constant. In fig. 2.15, the response function and the product of the response function and the electro-optic coefficient is plotted over the frequency. In the response function $G(\omega)$, the transmission of the THz wave into the crystal is included, and the velocity mismatch is regarded. The right plot with the effective response function $|G| \cdot |r_{41}|$ has a smoothly dropping part in the low frequency region (0 THz to 5 THz), and strong, nonlinear oscillations near the resonance frequency, whose maxima are not plotted (the effective response function becomes as large as 2.2 pm/V for a crystal thickness of 2 mm and 12.4 pm/V for 0.2 mm). A THz pulse that also contains frequency components in the region of the resonance frequency will excite these oscillations and the resulting EO signal will exhibit strong distortions because of the ringing at about 11 THz due to the resonant oscillations. For very high frequencies the effective response function becomes constant again (not shown) due to the purely electronic material response.

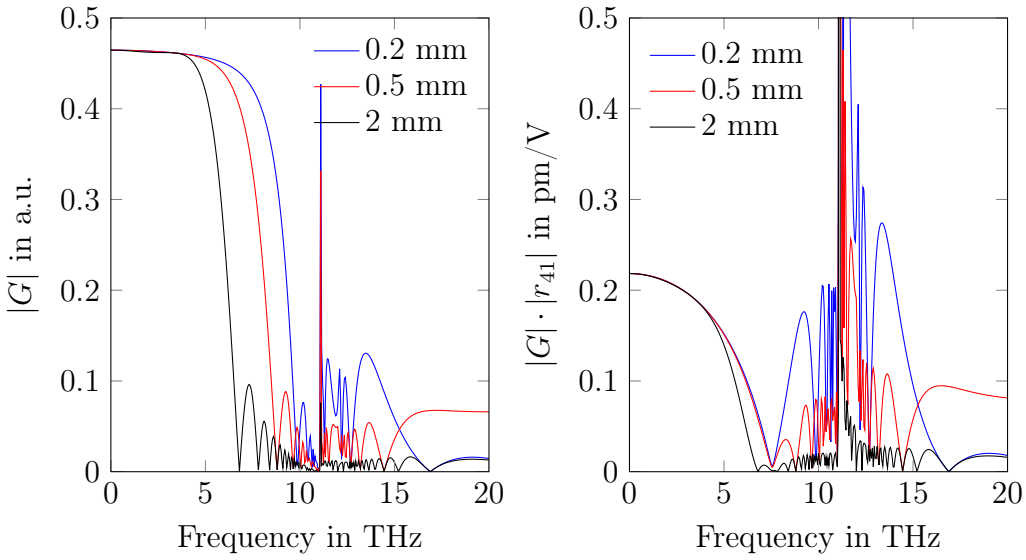

Figure 2.15: EO response function $|G|$ (left) and effective EO response function $|G| \cdot |r_{41}|$, both for $\lambda_{opt} = 1030$ nm. For explanation see text, compare also to [75], fig. 4.9.

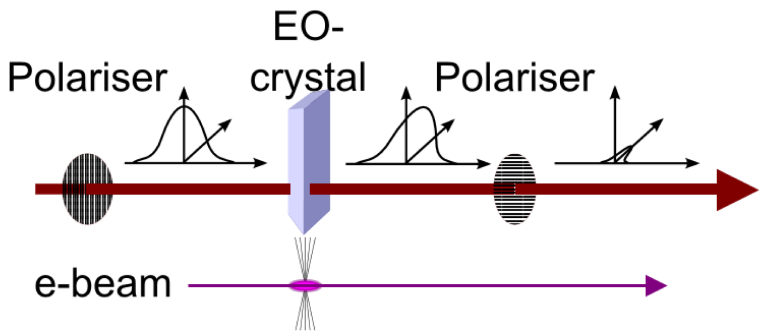

Figure 2.16: Principle of electron bunch diagnostic using electro-optic methods. The EO crystal is installed inside the beam pipe, the optics outside of it. Along the thick arrow, a laser pulse propagates, an electron bunch passes the EO crystal within a few mm distance. Explanations see text.

2.3.6 EO Techniques

Three commonly employed measurement techniques exist for electro-optic THz wave detection: The crossed polariser setup, the near-crossed polariser setup and the balanced detection.

The first one mentioned is sketched in fig. 2.16. The laser pulse is linearly polarised by a polariser before it enters the EO crystal (in the little inset 3D coordinate system the enveloppe of the laser pulse lies in the ZY plane when Z is the propagation direction). If there is no electric field applied to the crystal, there is no change of the polarisation state occuring in the crystal. Thus the laser will be completely blocked at the next polariser which is turned by 90° with respect to the first one (the polarisers are 'crossed'). Ideally, no light is transmitted in this case. If on the other hand an external electric field (here, the THz pulse traveling along the beam pipe together with the electron bunch) is applied the the electro-optic crystal while the laser pulse passes through it, a polarisation modulation will occur. This case is indicated as a tilt of the laser pulse enveloppe by a small angle towards the XZ plane in the inset coordinate system (in reality, the polarisation is turned to be elliptical). At the second polariser a portion of the incident laser intensity will be transmitted according to the strength of the polarisation modulation (shown as the projection of the tilted laser enveloppe on the XZ plane). Mathematically this is described using the Jones calculus for polarised light. The procedure deploys the multiplication of 2-by-2 matrices standing for single components that act on the polarisation of light. The goal is to determine the electric field at the light detector. The laser pulse propagates perpendicular to the XY-plane in the crystal coordinate system defined in section 2.3.4 (see fig. 2.11). It turned out that the maximum phase advance Γ_{max} is found for a measurement geometry with the crystal cut along the (110)-plane and an angle ($\varphi = 45°$) between the main axis $\boldsymbol{U}_1$ of the index ellipsoid intersection plane and the crystal X axis and an electric field vector along the $\boldsymbol{U}_1$ axis ($\alpha = 0$). For the Jones calculus, the horizontally and vertically polarised laser light can be written as

$$\boldsymbol{E}_h = E_{Laser} \begin{pmatrix} 1 \\ 0 \end{pmatrix} \text{ and } \boldsymbol{E}_v = E_{Laser} \begin{pmatrix} 0 \\ 1 \end{pmatrix}, \tag{2.83}$$

respectively, a rotation of the polarisation plane is done with a rotating matrix

$$\boldsymbol{R}(\varphi) = \begin{pmatrix} \cos(\varphi) & -\sin(\varphi) \\ \sin(\varphi) & \cos(\varphi) \end{pmatrix}, \tag{2.84}$$

while a $\lambda/4$ wave plate and a $\lambda/2$ wave plate are described by $\boldsymbol{Q}$ and $\boldsymbol{H}$ as

$$\boldsymbol{Q} = \exp(i\pi/4) \begin{pmatrix} 1 & 0 \\ 0 & -i \end{pmatrix} \text{ and } \boldsymbol{H} = \boldsymbol{Q}^2 = \exp(i\pi/2) \begin{pmatrix} 1 & 0 \\ 0 & -1 \end{pmatrix}, \tag{2.85}$$

respectively. The effect of the birefringent EO crystal with its refractive indices n_s and n_f (each depending on the angle α between the electric field vector $\boldsymbol{E}_{THz}$ and the $\boldsymbol{U}_1$ axis, $n_s(\alpha)$ and $n_f(\alpha)$) can be written as

$$\begin{aligned} \boldsymbol{EO}(\alpha) &= \begin{pmatrix} \exp(-in_s(\alpha)\omega d/c) & 0 \\ 0 & \exp(-in_f(\alpha)\omega d/c) \end{pmatrix} \\ &= \begin{pmatrix} \exp(-i\Gamma(\alpha)/2) & 0 \\ 0 & \exp(i\Gamma(\alpha)/2) \end{pmatrix} \exp(-i\kappa) \\ &\text{with } \kappa = (n_s + n_f)\omega c/d \end{aligned} \tag{2.86a}$$

where d is the thickness of the crystal and κ the averaged phase advance that can be separated out. $\Gamma(\alpha)$ is given by eq. 2.75. The phase factor in the above equations is omitted in the following as it drops out by calculating the intensity at the detector. To find the field strength at the detector E_{det}, the matrices corresponding to the used setup are multiplied in the correct order, with the matrix product 'acting to the right'. In case of the crossed polariser setup, this leads to

$$E_{det} = \begin{pmatrix} 0 & 1 \end{pmatrix} \cdot \boldsymbol{R}(-\varphi) \cdot \boldsymbol{EO}(\alpha) \cdot \boldsymbol{R}(\varphi) \cdot E_{Laser} \begin{pmatrix} 1 \\ 0 \end{pmatrix}. \tag{2.87}$$

In eq. 2.87, the polarisaton plane of the laser light is turned by $\boldsymbol{R}(\varphi)$ into the principal axis system of the EO crystal where the polarisation is turned slightly and depending on n_s and n_f. Then, the polarisation plane ist turned back into the laboratory system by $\boldsymbol{R}(-\varphi)$, and the horizontal polarisation is picked using (0 1). Working this through and calculating the intensity at the detector $I_{det} = \frac{c\epsilon_0}{2}|E_{det}|^2$ for the angle of maximum induced birefringence

$\alpha = 0$, we find

$$I_{det} = \frac{c\epsilon_0}{2} E_{Laser}^2 \sin^2\left(\frac{\omega d}{2c} n_0^3 r_{41} E_{THz}\right) + s_{bg} I_{Laser}. \tag{2.88}$$

The intensity at the detector is proportional to the square of the electric field applied to the EO crystal E_{THz}. A factor $s_{bg} I_{Laser}$ has been added to account for the background laser intensity caused by imperfect input laser polarisation, residual birefringence that could not be compensated, and scattering in the crystal, that leads to some laser intensity at the detector even for $E_{THz} = 0$. Another measurement technique is called 'near crossed polariser' or short 'near CP' measurement. The analyser section is extended with a $\lambda/4$ (turned to the angle ψ) and a $\lambda/2$ wave plate turned by θ before the second polariser, so the electric field at the detector is calculated to be

$$\begin{aligned} E_{det}(\theta, \psi, \Gamma) = &\begin{pmatrix} 0 & 1 \end{pmatrix} \cdot \boldsymbol{R}(-\theta) \cdot \boldsymbol{H} \cdot \boldsymbol{R}(\theta) \cdot \boldsymbol{R}(-\psi) \cdot \boldsymbol{Q} \cdot \boldsymbol{R}(\psi) \\ &\cdot \boldsymbol{R}(-\varphi) \boldsymbol{EO}(\alpha) \cdot \boldsymbol{R}(\varphi) \cdot E_{Laser} \begin{pmatrix} 1 \\ 0 \end{pmatrix}. \end{aligned} \tag{2.89a}$$

For $\alpha = 0 \rightarrow \varphi = \pi/4$ this results in

$$\begin{aligned} E_{det}(\theta, \psi, \Gamma) = &\frac{E_{Laser}}{\sqrt{2}} [\cos(2\theta) \sin(\Gamma/2) - \sin(2\psi - 2\theta) \cos(\Gamma/2) \\ &- i(\sin(2\theta) \cos(\Gamma/2) + \cos(2\psi - 2\theta) \sin(2\theta))]. \end{aligned} \tag{2.90a}$$

The intensity at the detector in general and for the two cases of $\theta = 0$ and $\psi = 0$ becomes

$$\begin{aligned} I_{det}(\theta, \psi, \Gamma) &= \frac{c\epsilon_0}{2} |E_{det,v}^2| + s_{bg} I_{Laser} \\ &= \frac{I_{Laser}}{2} \left[1 - \cos(\Gamma - 2\psi + 4\theta) \cos^2(\psi) \right. \\ &\quad \left. + \cos(\Gamma + 2\psi - 4\theta) \sin^2(\psi)\right] + s_{bg} I_{Laser} \end{aligned} \tag{2.91a}$$

$$I_{det}(\theta, \psi = 0, \Gamma) = \frac{I_{Laser}}{2} (1 - \cos(\Gamma + 4\theta)) + s_{bg} I_{Laser} \tag{2.91b}$$

$$\begin{aligned} I_{det}(\theta = 0, \psi, \Gamma) = &\frac{I_{Laser}}{2} \left[1 - \cos(\Gamma - 2\psi) \cos^2(\psi) + \cos(\Gamma + 2\psi) \sin^2(\psi)\right] \\ &+ s_{bg} I_{Laser} \end{aligned} \tag{2.91c}$$

With the above formula a measurement setting for the angles of the wave plate retarders can be found that does not maximise Γ but $\partial I_{det}/\partial\Gamma$ at $\Gamma = 0$: As

typically the phase advance is very small, the setting for the biggest effect over a small background is searched. Minimising the background ensures a better signal-to-noise ratio at the detector. In conclusion, turning the quarter wave plate leads to a smaller modulation depth for the $\lambda/2$ wave plate settings, so it is only used for compensating residual birefringence of the crystal. Then a setting for the $\lambda/2$ wave plate is searched where the background is small and the achieved signal large. An approximation can be given for $I_{det}(\theta, \psi = 0, \Gamma)$ to yield

$$I_{det}(\theta, \psi = 0, \Gamma) \approx I_{Laser} 2\theta\Gamma + I_{Laser}(4\theta^2 + s_{bg}) \tag{2.92}$$

where $4\theta << 1$ and $\Gamma << 8\theta$ (see [75]). It is important to note that in difference to the CP setting the intensity at the detector is proportional to Γ and thus to the electric field E_{THz} and not to its square. This means the intensity at the detector can drop due to induced birefringence.

The third commonly used electro-optic technique is the balanced detection scheme in which a Wollaston prism is used as the analysing polariser and the light of both polarisation states is directed onto a detector (each). This is realised by inserting only a $\lambda/4$ wave plate turned by 45° in between the EO crystal and the analyser. The intensity for the two polarisation states $(I_{det,h}, I_{det,v})$ at the detector then becomes

$$I_{h,v} = \frac{I_{laser}}{2}(1 \pm \sin(\Gamma)) + s_{bg} I_{Laser} \tag{2.93a}$$

$$I_{det,h} - I_{det,v} = I_{Laser} \sin(\Gamma) \tag{2.93b}$$

The signal is proportional to E_{THz} for small Γ, and not to its square. This implies that the signal will be much larger than in the CP setup as $\Gamma << 1$. This background-free setup is often used in multishot measurements with low laser powers.

2.3.7 Setups for Electro Optic Detection

In the above section, three different techniques of electro-optic beam diagnostic have been considered. These can be applied in different ways. In the following, the typical experimental setups are regarded in which these techniques are applied.

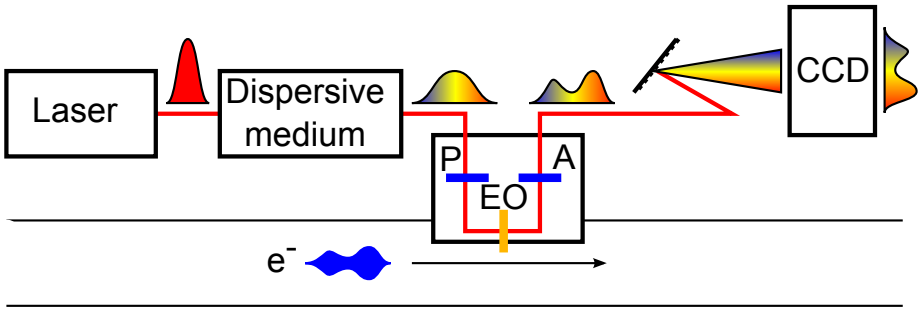

Figure 2.17: Sketch of an electro-optic spectral decoding setup, P - polariser, EO - EO crystal inside beam pipe, A - analyser section, CCD - camera. The laser pulse is linearly stretched in a dispersive medium. The different frequency components that are sorted along the laser pulse interact with different parts of the THz pulse of the electron bunch in the EO crystal. The imprinted bunch profile can be extracted using a spectrometer.

An often used approach is the electro-optic sampling (EOS). This is a multishot measurement where the laser pulse is consecutively shifted against the THz pulse in precise timesteps. As for all multishot measurements, the jitter between the laser pulse and the THz pulse is a limiting factor for the achievable resolution, as well as the duration of the probe laser pulse. Furthermore this setup is only useful if the sampled THz pulse is reproduced in the same shape every time. At FLASH, recent EOS experiments use pulses of a 30 fs Ti:sapphire laser that is locked to the accelerator driving frequency with an integrated timing jitter of less than 100 fs [34]. The experiments were primarily conducted to characterise the CTR transport beam line (see ch. 3.2.3), see [85]. Here, the technique of balanced detection was used, and the maximum of the measured field strength of the single-cycle THz pulse was up to 1 MV/cm.

A drawback of the electro-optic sampling for longitudinal electron bunch diagnostic is that it is a multishot setup and thus only provides information on the average THz pulse (or electron bunch) shape. A single-shot setup relatively easy to implement is the electro-optic spectral decoding (EOSD), sketched in fig. 2.17. Here, the laser pulse from the fs laser system is broadened in time by sending it through a dispersive medium. Due to the chromatic dispersion, a linear frequency chirp is imprinted on the laser pulse (see section 2.1.6). This means a linear relationship between the local optic frequency and the

location in the stretched pulse is established. Sending a stretched laser pulse through the electro-optic crystal together with the THz wave coming from the bunch, the leading part of the laser pulse will be modulated by the THz field of the leading part of the electron bunch, and the same for the trailing part. In the analysing polariser the polarisation modulation of the frequency components is turned into an amplitude modulation which can be detected using a spectrometer and a camera. This setup is usually deployed in the crossed polariser or near crossed polariser techniques as a balanced detection would need two (balanced) spectrometers. The noise of the detector camera suggests the use of the near crossed polariser scheme. Besides the fundamental resolution limits posed by the crystal resonances and the laser pulse duration that apply here just as in the case of electro-optic sampling, there is another limitation posed by the effect of frequency mixing. This effect leads to a restriction of the duration of resolvable features of the THz pulse of length T_{lim} given by

$$T_{lim} \approx 2.6\sqrt{T_0 T_c} \tag{2.94}$$

where T_0 and T_C denote the transform-limited FWHM duration of the laser pulse and the FWHM duration of the chirped pulse, respectively. In [63], a more complex formula is deduced in the search of the optimal amount of chirp for the detection of a THz pulse of given length. The distortion that appears for smaller features than T_{lim} that limits the resolution can be thought of as the production of frequency sidebands with $f = f_{opt} \pm f_{THz}$ (details see [38]. This effect of frequency mixing is in newer experiments used as the actual EO detection principle, then called upconversion, and deployed for the measurement of THz pulses using narrowband laser probes [81], [78].

To overcome the limitations imposed by frequency mixing while still enabling single-shot measurements, a pure time-domain measurement called electro-optic temporal decoding (EOTD) has been deployed. Here, the chirped laser pulse with the imprinted bunch profile is analysed by means of second-harmonic generation in a BBO crystal in a non-collinear way, where the chirped laser pulse is sampled by a short gate pulse. This setup enabled faithful electro-optic bunch shape reconstruction in a 2007 experiment at FLASH [74]. However, this experimental setup requires a high-power laser (pulse energies about 0.3 mJ) to drive the nonlinear frequency doubling process. Similar setups extend-

ing this idea are used by now named 'x-frog THz time domain spectroscopy', where in addition one spatial dimension is also mapped [51].

A further way of non-destructive bunch shape measurements is the electro-optic spatial decoding (EOSpD). Here, the EO crystal is oriented to the passing electron bunch under an angle, so consecutive parts of the electron bunch field are imprinted in different parts of the chirped laser pulse. This scheme has been deployed in an early bunch arrival time monitor at FLASH called TEO (timing electro-optical experiment) [6].

In general electro-optic methods have become more popular since the advent of laser driven THz pulses (for example by means of optical rectification) - in this case, there already is a laser pulse inherently synchronised to the THz pulse that has to be investigated. The same holds true for laser based electron acceleration through plasma wakefields (see for an overview [50]). Especially when an experiment operates at high repetition rates while producing only low THz intensities multishot setups including lock-in amplifier technology is often applied.

Chapter 3

The FLASH Accelerator

FLASH, the **f**ree-electron **las**er at **H**amburg, is an accelerator facility that delivers high peak brilliance laser pulses in the deep UV and down to the soft x-ray wavelength region for user experiments. Started as a collider test facility (TTF), a main feature of this linear accelerator is the use of superconducting accelerating structures, leading to a good luminosity in linear colliders. Important electron beam features for the use as a high-gain FEL are a high peak current and a small transverse emittance of the electron bunches. In this chapter, the accelerator facility is briefly described and the instrumentation and bunch properties relevant for this thesis are discussed.

3.1 The Linear Accelerator

3.1.1 The Electron Gun

The electron gun is designed to create bunches of up to 10^{10} relativistic electrons with a small transverse emittance and a small energy spread. This is accomplished using a laser driven photo-cathode and a 1 1/2 cell normal conducting RF structure. The photo-cathode laser is a multi-stage laser system delivering a variety of pulse patterns at a wavelength of 262 nm (two times frequency doubled Nd:YAG laser) [82]. The focused laser beam impinges on the photocathode and releases electrons via the photoelectric effect [42]. The emitted electrons are accelerated away from the photo cathode with a field gradient of up to 42 MV/m. Through reaching relativistic energies quickly,

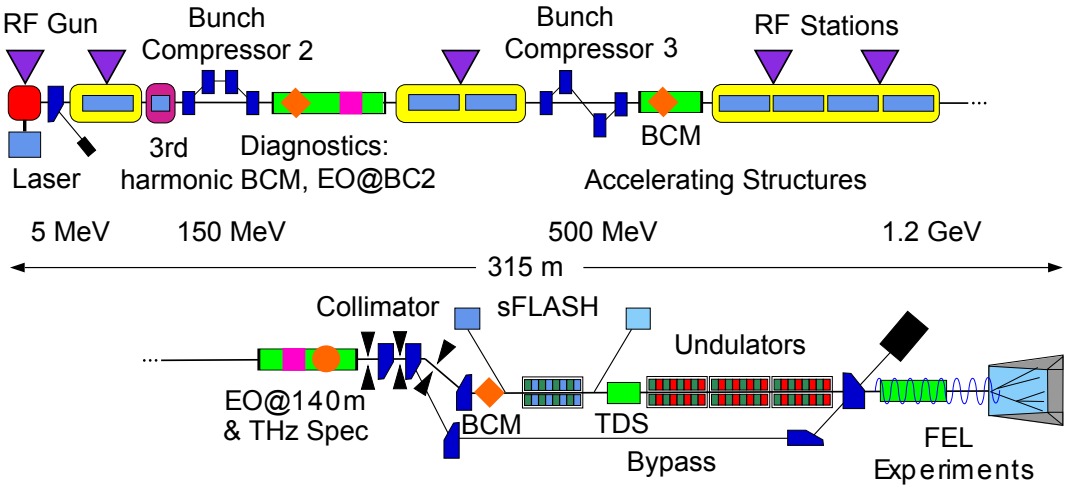

Figure 3.1: Sketch of the FLASH facility. Shown are the major components together with some longitudinal diagnostics instrumentation: Bunch compression monitors (BCM), EO setups at BC 2 and 140 m, Transverse Deflecting Structure (TDS), four stage THz spectrometer (CRSIP4).

the impact of the internal Coulomb repulsion of the electrons is suppressed, and thus the transverse emittance of the electron bunch is maintained. This way, a normalised transverse emittance of less than 5 mm mrad (projected emittance, rms, see [47]) is achieved. With an energy of about 4.5 MeV the electron bunch is injected into the first acceleration module. The duration of the uncompressed electron bunch at the exit of the gun is about 10 ps (FWHM) or 6 ps rms.

3.1.2 Accelerating Modules

After the 2009 upgrade, a total of 7 accelerating modules is installed at FLASH, powered by four klystrons. Every module contains eight niobium cavities that are cooled to 2 K with liquid helium. Each of these cavities consists of nine cells, a power coupler for the 1.3 GHz driving radio frequency (RF), a pick up antenna for field diagnostic, and a higher order mode coupler for suppressing higher resonant modes (see fig. 3.2). The cavities are standing wave resonators exited by the high power RF in the TEM_{010} mode. An electron in the center of a bunch enters the cell of a cavity at the moment of the zero crossing of the electric field. While the electron propagates through the cell, the amplitude

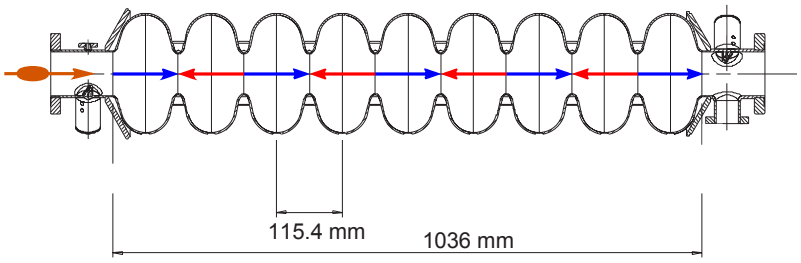

Figure 3.2: TESLA cavity. The electron bunch enters the next cell of the cavity at the zero crossing of the field amplitude, thus beeing accelerated over the whole length of the cavity. Adapted from [5].

grows until the electron is midway, and then decreases until the electron leaves the cell. The amplitude is always positive so that the electron is gaining energy all the time. As the electron reaches the next cell, the sign of the field changes in both cells, and the process repeats. An electron in the same bunch, but a distance δ before (behind) the bunch center is subjected to a negative field amplitude after entering (before leaving) the cell. The energy gain $g_E(\delta)$ is proportional to $\cos(\frac{\delta}{\lambda})$ (for $\delta << \lambda$) with λ being the wavelength of the accelerating field (and twice the period length of the accelerating structure). This mode of operation is called 'on crest' (though this originally refers to electron acceleration in travelling wave resonators). To retrieve an energy spread that grows monotonous over the length of the bunch (the ζ axis) which is needed for later bunch compression, the bunch is injected into the cavity with a phase offset ϕ resulting in an energy chirp $E(\zeta)$ proportional to $\sin(\phi) * \delta$ [20].

3.1.3 Bunch Compression

The peak current of the electron bunches at the exit of the electron gun is about 40 A (see fig. 3.5) which is not sufficient for later lasing. Compressing the bunch before acceleration would increase space charge effects. As these drop with a factor of $1/\gamma^2$, the first bunch compressor is installed behind the first acceleration module. There are two bunch compressors installed at FLASH, called BC2 and BC3 (There has been another bunch compressor once, BC1, which is obsolete now). They operate at electron energies of 130 MeV

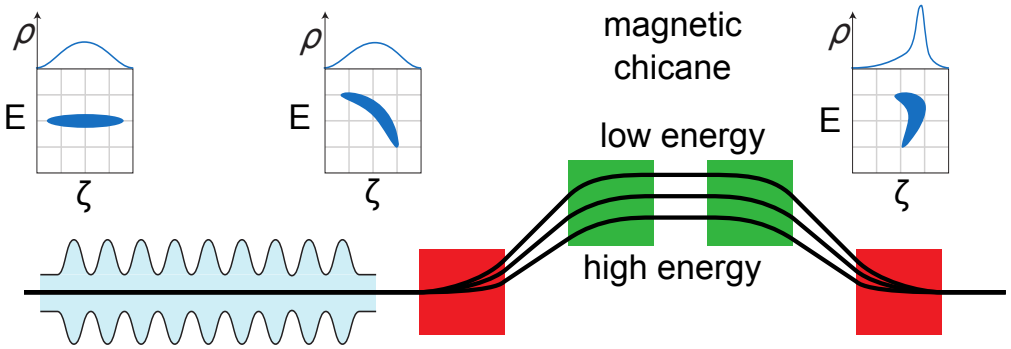

Figure 3.3: Principle of bunch compression. The inlets show the longitudinal phase space (Energy E over longitudinal coordinate ζ) and the longitudinal charge density (ρ) distribution (the projection of the phase space on the ζ axis). For details on bunch compression, see text. Adapted from [36].

and 450 MeV, respectively. Bunch compressors consist of a magnetic chicane forcing the electron bunch on a C-shaped (BC2) or S-shaped (BC3) detour (see fig. 3.3). Having received a monotonous energy chirp in the preceding accelerator module, leading electrons in the bunch have a lower momentum, they are forced on a longer detour than electrons in the bunch tail. The electrons are combined again to a much shorter bunch by leaving the bunch compressor, while the energy spread has not changed. Typical compression factors are about 10 and 5 in BC2 and BC3, respectively, however, varying compression schemes are used in practice.

3.1.4 3.9 GHz Module

In the 2009 shutdown, a 3.9 GHz module has been added to FLASH. It is a superconducting accelerator module operated at the third harmonic of the FLASH driving frequency, driven by an additional klystron. It enables a different compression scheme for a more robust SASE operation and in particular for a seeded operation of FLASH. The basic idea is that the energy chirp of the electron bunch resulting from the 'off-crest' acceleration in ACC1 has a nonlinear sine-shaped curvature. In first order approximation (i.e., for short bunches), this is linear over the bunch length. The next term in the Taylor expansion is cubic. To cancel this term, an energy chirp at the third harmonic is applied to the bunch using the 3.9 GHz cavity with the correct phase offset

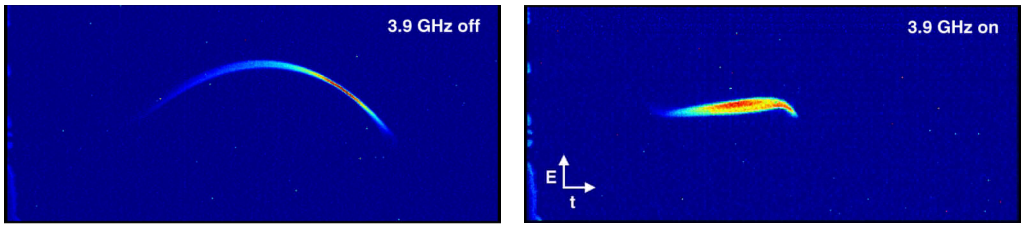

Figure 3.4: Phase space linearisation using the 3.9 GHz module. On the left, a phase space measurement without correction applied can be seen. It has been made by Ch. Behrens using the Transverse Deflecting Structure (TDS). On the right the same settings were used, but with a correcting field applied to the bunch in the 3.9 GHz module. The curvature due to the (in this case, nearly on-crest) acceleration in the preceding accelerator module (ACC1) is nearly completely corrected. Taken from [79].

(Needed for curvature correction: decelerating the bunches, but only slightly; the module is equipped with four nine cell cavities featuring lower accelerating gradients). In fig. 3.5 results from start-to-end simulations (by I. Zagorodnov) can be seen in which this bunch compression is simulated for a bunch charge of 1 nC, an initial bunch length of 20 ps (FWHM) (a flat-top injector laser is assumed), and a final energy of 1.2 GeV using the dual frequency linearisation of the phase space. The current profile over the time axis is drawn with the bunch head at the right side. Note the different axis ticks. In contrast to the rollover compression scheme applied before the 2009 upgrade, the current profile remains symmetric, and most of the bunch charge contributes to the lasing high current part of the bunch [65]. The fragmentation of the simulated bunch current at the entrance of the undulator (right picture) is due to collective effects that diminish with lowering the total charge of the bunch. Since the 2009 upgrade, a typical operation bunch charge is 0.5 nC.

3.1.5 SASE process

After acceleration and compression, the electron bunch passes an energy collimator and enters an experiment and matching section before it reaches the undulator section. Undulators are periodically poled magnetic structures with a small gap, forcing the electron bunch on a sinusoidal trajectory [1]. The short electron bunch with a high peak current emits synchroton radiation at each

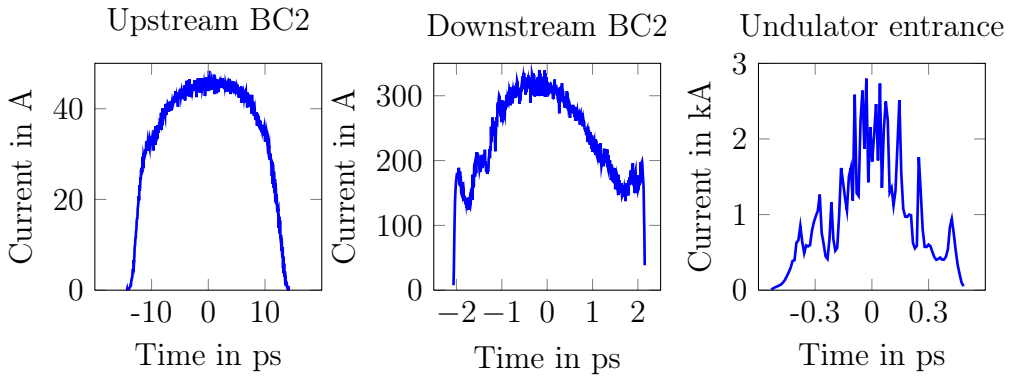

Figure 3.5: Longitudinal charge profile at different locations in FLASH. Simulations done for a 1 nC bunch by I. Zagorodnov. The bunch head is at the right side. Note the different axis ticks.

bend. If the overlap of the emitted x-ray radiation and the electron bunch is maintained, the light field induces a density modulation in the electron bunch (microbunching, see fig. 3.6). This process is self-enhancing at the right conditions and leads to coherent emission of short and intense laser pulses in the SASE (self amplified spontaneous emission) process [54]. The undulators need a certain minimum length depending on the undulator gap, its period length and the electron bunch energy and emittance to reach the SASE gain saturation. The laser pulses are directed through a photon diagnostic section into the FLASH experimental hall, where they can be distributed to different beam lines for user experiments.

3.1.6 Timing of the Bunches

FLASH is equipped with superconducting cavities featuring very low wall losses. As a consequence, the driving RF field can be maintained longer than in normal conducting devices. At FLASH, the RF macropulse is 800 µs long and is delivered ten times a second (10 Hz), see fig. 3.7. During the macropulse, a bunch train with repetition rates of 10 kHz or up to 1 MHz is injected into the cavities. A 3 MHz option has been tested for a high current mode. This timing scheme needs to be covered by all devices from the injector laser to the diagnostics, resulting in a couple of devices operated at 10 Hz, while others can cover every bunch in the macropulse. The actual bunch length depends on the

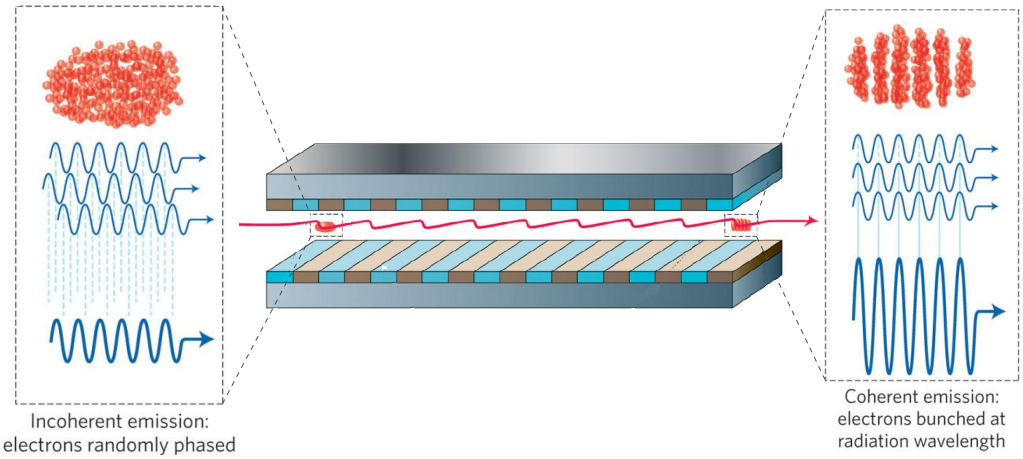

Figure 3.6: Schematic of the SASE process, adapted from [54]. In the beginning of the undulator, the electron bunches start to emit synchroton radiation randomly phased but mainly at the undulator design wavelength. This radiation imprints a density modulation on the elctron bunch while copropagating through the undulator. The microbunched electron bunch emits coherent light.

location in the linear accelerator as well as on the compression scheme and is typically about 150 fs FWHM at the undulator entrance in normal operation mode. Devices that are designed to work on the electron bunches or measure their properties need to be precisely synchronised to the accelerator driving frequency (1.3 GHz, also subharmonics are distributed) and triggered by the 10 Hz machine trigger that is spread around the facility. The timing is derived from the AC line zero crossing: When 100 ms are over since the last trigger (in 10 Hz mode), the next trigger is created at the next zero crossing of the 144^{th} subharmonic of 1.3 GHz (9.027 MHz) after the AC line zero crossing. The 9 MHz clock signal runs continuously, but any device synchronised with the electron bunch needs to wait for the machine trigger to hit the right 9 MHz bucket.

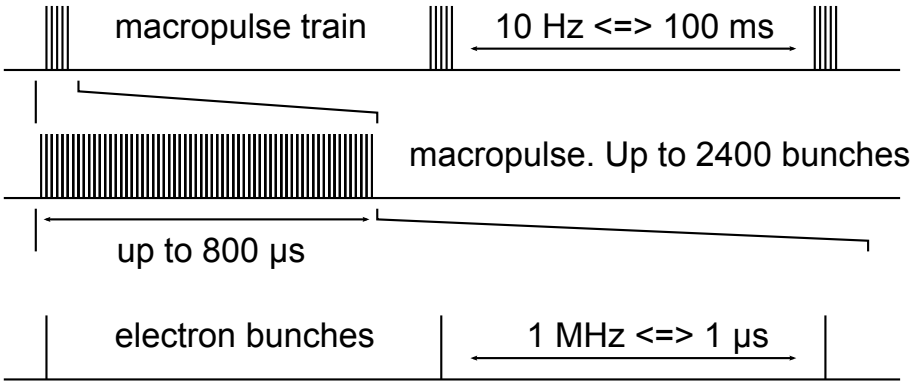

Figure 3.7: Timing of the electron bunches in the FLASH accelerator. Ten macropulses per second containing several electron bunches are accelerated together by one cavity filling of a duration of 800 µs. A typical macropulse train consists of 2 to 30, but up to 2400 electron bunches. The intra bunch train repetition rate can be varied between 10 kHz and 3 MHz but is usually 100 kHz or 1 MHz. The bunches itself have a length on the scale of picoseconds.

3.2 Longitudinal Diagnostics

The measurement of the longitudinal bunch profile, i.e., the charge distribution ρ along the ζ axis in a rotational symmetric way (1D) is a challenging task, as the compressed bunches have a length of only a few hundred micrometers (depending on the compression scheme) and may even have a subtle microstructure. There are a few devices meant for this task, some are well established and in operation for years, others are still experiments.

3.2.1 Transverse Deflecting Structure

The Transverse Deflecting Structure (TDS), also called LOLA after their inventors (Loew, Larsson, and Altenmueller [46]), is a precise way to determine the longitudinal bunch profile and even the phase space distribution of the bunch. Since the 2009 upgrade it is located just before the undulator section. It consists of a 3.6 m long travelling wave cavity powered by a klystron (S-band, 2856 MHz), a fast kicker magnet, a dipole with a drift section and different screens including cameras. When the electron bunch enters the cavity, an electric field perpendicular to the direction of propagation is applied.

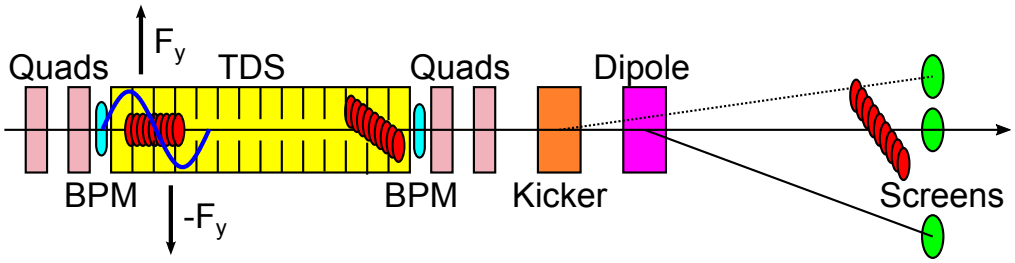

Figure 3.8: Schematic of the Transverse Deflecting Structure (TDS) layout and operation principle. The electrons in the bunch are subjected to a position depending kick F_y and thus sheared at the screen. A dipole and a dispersive section form an energy spectrometer. Using both, the longitudinal phase space distribution E over ζ is accessible. BPM - beam position monitor, Quads - pair of quadrupole magnets.

This field is zero for an electron in the center of the bunch and has opposite signs for electrons in the head and the tail of the bunch. In this way electrons with different longitudinal positions in the bunch (pictured as slices in fig. 3.8) are subjected to a transversal kick ($\pm F_y$) depending on their position. After a drift section the electrons have a corresponding transverse displacement. The longitudinal coordinate has been transformed to the vertical coordinate. A dipole in the beginning of the drift section can be used to horizontally deflect the electrons in the bunch according to their momentum. Together with the drift section this results in a translation of the energy information to the horizontal axis on the OTR screen. Thus, a transformation of the longitudinal phase space (t, $\delta E/E$) to (y, x) coordinates is achieved. Depending on the magnet optics used, a longitudinal resolution of some tens of femtoseconds (fs) can be reached. The energy spectrometer resolution depends on the strength of the dipole and the length of the dispersive section. After having passed the TDS, the electron bunch can not be used for lasing, making this a destructive method. The filling time of the deflecting cavity (0.64 µs) allows for the investigation of one bunch out of the bunch train when the fast kicker is used.

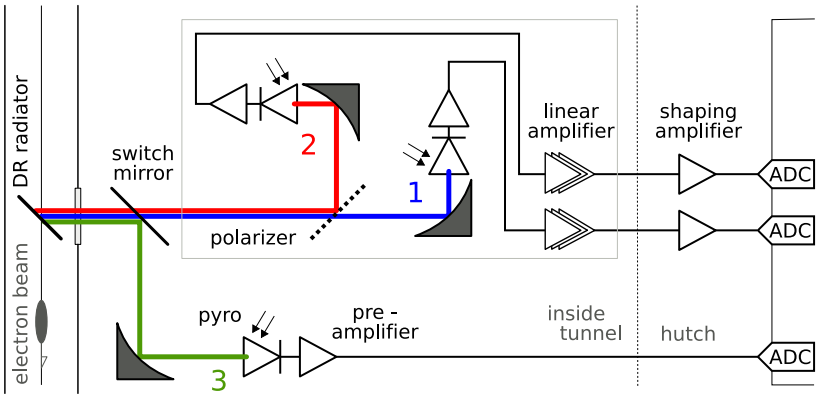

Figure 3.9: Schematic of the upgraded BCM (bunch compression monitor) installed behind BC2. The electron bunch passes through a small slit in the diffraction screen. The emitted radiation grows with increasing bunch compression. The radiation is focused on pyroelectric sensors. The signal is amplified with different amplifiers and sampled. Picture taken from [10].

3.2.2 Beam Compression Monitors

A couple of monitor systems rely on the measurement of the radiation emitted by the electron bunch when it passes a bend (synchroton radiation, SR, [25]), traverses a thin metal foil (transition radiation, TR, used for transversal electron bunch diagnostic and projected emittance measurements (OTR standard diagnostic [17], CTR beamline with four stage spectrometer, see sec. 3.2.3)) or passes a small slit in a metal screen (diffraction radiation, DR (BCM)). All of these different processes produce incoherent and coherent radiation depending on the electron bunch properties and regarded wavelength. A bunch starts to emit coherently as soon as the wavelength of the emitted radiation is on the order of magnitude of the bunch length (cooperation or coherence length). If a bunch of N electrons emits incoherent radiation, the intensity is proportional to N. In the coherent case the overall intensity grows dramatically as it is now proportional to N^2.

Behind each bunch compressor and behind the energy collimator a bunch compression monitor (BCM) is installed. This device is a sensor for the amplitude of the diffraction radiation (DR) of the electron bunch passing a slit in a thin metallic foil. A typical setup consists of a diffraction screen, focussing optics, and a pyroelectric sensor that is sensitive over a large wavelength range

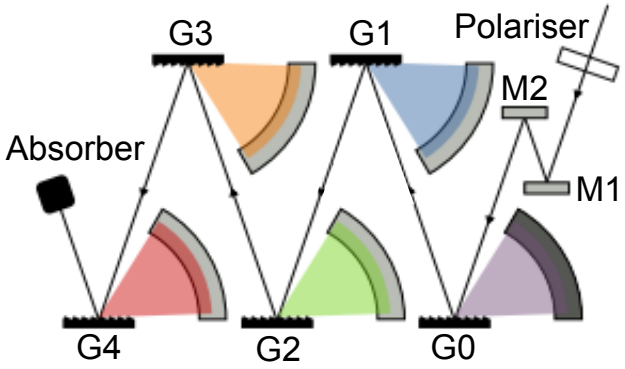

Figure 3.10: Operation principle of the four stage CTR spectrometer (CRISP4). The mirrors M1 and M2 are for initial alignment. The grating G0 acts as a low pass filter. The deflected zeroth order of each grating is decomposed by the consecutive grating. The grey components are gold cold coated ring mirrors that direct the spectrally decomposed radiation onto 30 pyroelectric sensors each. Taken from [80].

in the near and far infrared (see fig. 3.9, here, three different optics and sensors of varying sensitivity can be used). Some amplifier electronics and an analogue/digital converter (ADC) connect this device to the control system enabling an intra bunch train feedback on the bunch compression (Repetition rate of up to 1 MHz). The BCMs do not interact with the bunch and are a tool used in standard operation. Together with charge readings and some calculations, the bunch length can be estimated from the BCM signal.

3.2.3 CTR Spectroscopy

A much more sophisticated approach is the spectral decomposing of the coherent transition radiation (CTR) emitted by a bunch that hits a metal screen. At FLASH, this is achieved by the use of a beam line for the transport of the THz radiation, a four stage assembly of optical gratings, and a corresponding detector array of pyroelectric sensors. The 20 m long evacuated beamline transports the radiation emitted by the electron bunch from the accelerator tunnel to the laboratory over six remotely steered mirrors. It is designed for wavelengths from 0.2 THz up to the optical regime [15]. The focusing elements of the beamline are designed to image the spot on the metal screen where the

electron bunch hits onto the detector device. The complete spectrometer is mounted in a vacuum vessel [80]. It consists of four reflective gratings for different wavelengths in a staged scheme: The zeroth order reflected by one grating is decomposed by the next grating (see fig. 3.10). Two sets of gratings can be used, one for the mid-infrared wavelength range from 5 µm to 43.5 µm and one for the far-infrared radiation range from 45 µm to 440 µm. The grating set can be chosen remotely. The deflected and dispersed radiation hits gold mirrors that direct it on an array of 30 pyroelectric sensors per grating, giving a total of 120 pyroelectric sensors. The signal of each sensor is amplified in a charge sensitive preamplifier and a gaussian shaping amplifier before it is sampled by a 14 bit, 9 MHz ADC. Different sets of amplifiers can be used to achieve a 10 Hz or 1 MHz repetition rate of the single shot measurements. The spectrometer is calibrated utilising the transverse deflecting cavity (TDS). From the bunch shapes measured with the TDS the form factors (the Fourier transform of the normalised line charge density) are calculated and compared to the form factors calculated from the spectroscopic measurement. In this calculation the transport of the THz radiation through the CTR beam line, the grating efficiency and the wavelength dependend sensitivity of the pyroelectric sensor need to be considered. The spectrometer becomes a standard diagnostic tool, with operator friendly software fully integrated in the control system, under the name CRISP4. It is especially useful for the measurement of low charge bunches at high compression.

3.2.4 Electro-Optical Devices

Another class of devices tests the Coulomb field of the electron bunch utilising the Pockels effect occuring in nonlinear optical crystals. These crystals become birefringent when an electric field is applied to them. This change can be tested using a polarised laser beam (see sec. 2.3.3). There are different setups in use at FLASH. Those that are part of this thesis are described in detail in chapter 4.2.

The timing electro-optic experiment (TEO) uses a part of the pump-probe laser pulse also used for the user experiments [6]. It relies on the technique of spatial decoding and is a rather complex setup, involving an optical fibre transport with dispersion compensation including a spatial light modulator,

the actual EO setup in the beam pipe, and a gated camera. This setup allowed to measure the pump probe laser/electron bunch timing precisely for the first time, which is useful for an a posteriori sorting of the pump/probe shots. Even though it is possible, this device is not meant or optimised to be used for measurements of the longitudinal bunch shape.

Another area for EO experiments at FLASH is at 140m, where the bunches are fully compressed. This area has been used for EO experiments using the temporal decoding technique, where the stretched laser pulse with the imprinted information of the bunch train is sampled by a short laser pulse using a frequency doubling crystal. These measurements have reached the highest temporal resolutions up to now, bunch shape features with a length of less than 60 fs have been measured [11]. However these experiments make use of a complex laser system making it not ideal for the use as a standard diagnostic tool. Different other EO experiments have been conducted in this area making use of the existing vacuum chamber and laser transfer line. A detailed description of the present spectral decoding setup is found in chapter 4.2.

Using the experiences gained with the setup at 140m, another bunch shape monitor relying on the EO principle has been added to FLASH. This compact EO monitor is installed behind the first bunch compressor (BC2, thus 'EO@BC2') and uses the electro optic spectral decoding detection principle (see 2.3.7). A detailed description can be found in the next chapter (see 4.3), as the installation of this monitor is part of this thesis (see also [12]).

More electro-optic experiments are conducted at a second output port of the CTR beamline where also the four stage CTR spectrometer is situated [34]. Electro-optic sampling (EOS, see 2.3.7) is used for the investigation of the properties of the transmitted THz radiation in the temporal domain and thus to characterise the CTR beamline [85].

Chapter 4

Experimental Setup

This chapter gives an overview of the experimental setups used in this thesis, it is divided into three parts. The first one is dedicated to the technical realisation of the ytterbium doped fibre laser (YDFL) system. Its development starting from a prototype laser system [83] up to now is covered here as well. The laser system is in use at the EO station at 140 meter, which is described in detail in the second section of this chapter. A third section covers the EO setup downstream the first bunch compressor (BC2) with its new frontend design and commercial laser system.

4.1 Ytterbium Doped Fibre Laser System

The YDFL system is realised in the master laser power amplifier (MOPA) configuration. The oscillator development emphasis was to meet the requirements of stability and it has been optimised for synchronisation to the accelerator driving frequency. The amplifier stages have been designed to deliver the pulse energy and bandwidth needed for single-shot electro-optical measurements and to allow for different burst schemes using gating components.

4.1.1 Oscillator

General Design

In chapter 2.2.5, the general design of the laser oscillator has been sketched. Here the details are presented. First the light path may be regarded once

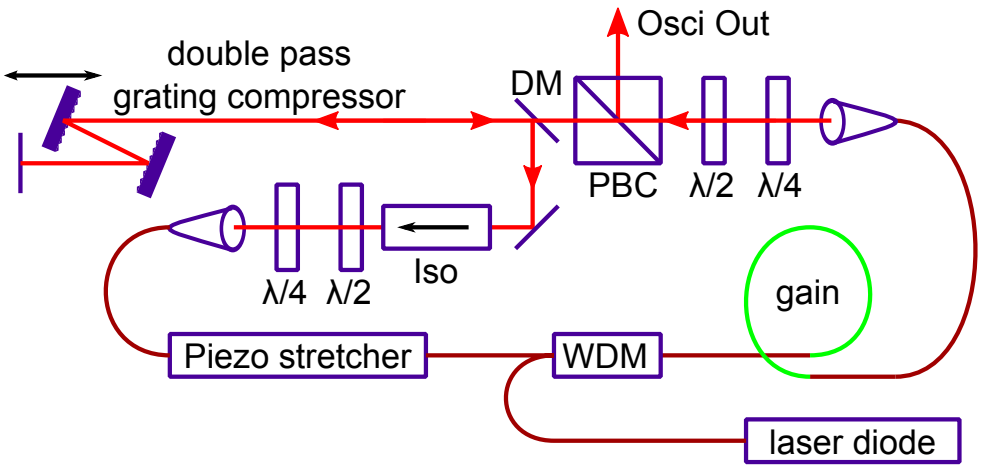

Figure 4.1: Layout of the YDFL oscillator. Iso: isolator, WDM: wavelength division multiplexer, $\lambda/2$ and $\lambda/4$: half/quarter wave plates, PBC: polarising beam cube, DM: D-shaped mirror, gain: Yb doped gain fibre. Osci out marks the actual free space output port of the oscillator.

(compare fig. 4.1 and fig. 4.2). The oscillator is optically pumped with a 600 mW, 950 mA single-mode fibre coupled laser diode emitting cw light at 976 nm matching the main absorption band of ytterbium (see fig. 2.7). A high pump power is used for modelock search but in standard operation the pump power is decreased to typically 300 mW. Over a wavelength division multiplexer (WDM), the pump light is coupled into the active fibre (Coractive Yb 164, now sold as Yb 501). The gain fibre has a length of 58 cm. The high dopant concentration results in a strong absorption at 976 nm, leading to an attenuation of the pump light in the gain fibre of more than 50 db. The light emitted around 1030 nm by the gain fibre is directed through a collimator and two motorised retarder wave plates. In the fibre section, the polarisation state of the light is arbitrarily changed. With the λ quarter wave plate, the polarisation is linearised, and with the λ half wave plate, the splitting ratio at the following polarising beam splitter cube is defined. Beam cubes are transmittive for horizontally polarised light and reflective for vertically polarised light. The reflected component is the actual oscillator output. The transmitted light passes over a D-shaped mirror and enters a double-pass grating compressor which is needed for dispersion compensation. The grating separation is variable, distances between 2 cm to 3.5 cm are possible, so different amounts of

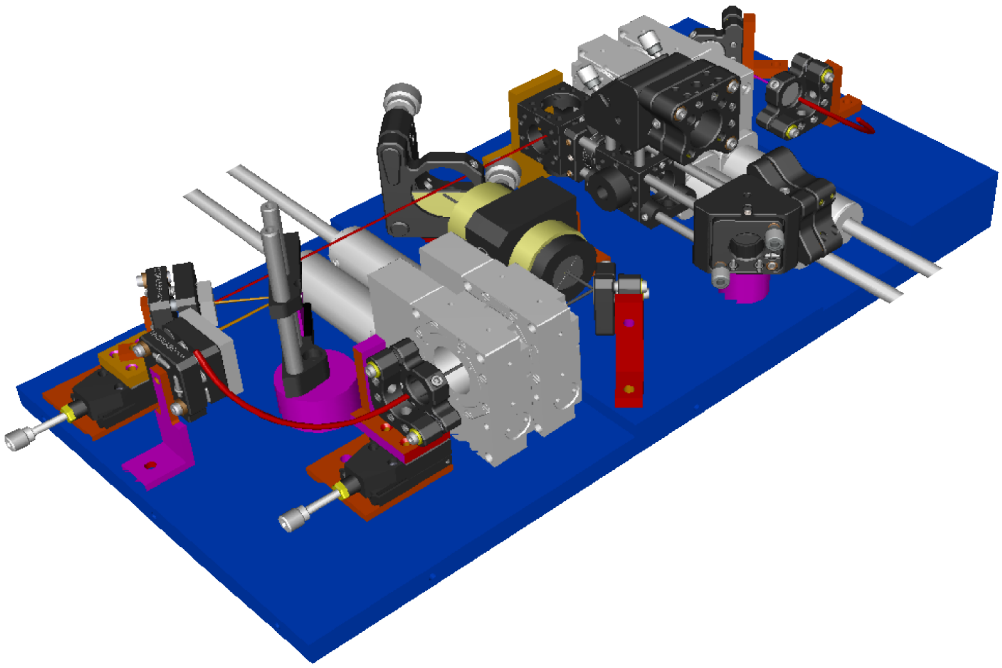

Figure 4.2: 3D drawing of the YDFL free space section. The light pass consideration (see text) starts at the fibre collimator in the upper right. The grey components are the motorised wave plate holders. The black cage system contains two polarising beam cubes, the upper one is the oscillator output, in the other one the output is divided into two parts that are both coupled into a fibre collimater (only mounts shown) over a mirror. The D-shaped mirror is passed on the way to the double-pass grating compressor, whose end mirror is slightly tilted with respect to the perpendicular plane to the optical axis. On the way back the beam is thus reflected on the D-shape mirror and directed through the isolator (the cylindrical device) and a pair of waveplates, again motorised, into a fibre collimator. The holder for the end collimator and the holder for the first grating of the compressor (on the left side) are mounted on miniature manual delay stages that can be adjusted from outside the laser oscillator housing. By courtesy of K. Ludwig.

	Length in cm	GVD/cm in $(fs)^2/cm$	total GVD in $(fs)^2$
gain fibre	58	222	12876
SMF	87	222	19314
free space	61	0	0
grating compressor	2.4	-12872	-30892
total	211	-	1297
Repetition rate	108.676 MHz		

Table 4.1: Dispersion map of the YDFL. The cavity length fine adjustment affects only the free-space length. For the calculation of the repetition rate the optical path length is considered. The total GVD value is slightly positive.

chirp can be added. Having been reflected at the end mirror under a slight angle, the light hits the D-shaped mirror on the return path and is guided through an isolator that prevents counterpropagating pulses in the ring cavity which helps finding a modelocked state of operation. Another pair of motorised wave plates is traversed that sets the polarisation state of the light to elliptical before the light enters the fibre part of the cavity again. Between the collimator and the pump light coupling WDM (i.e., in the low power branch of the cavities' fibre part), a piezo fibre stretcher is passed which accounts for quick changes of the laser cavity length (see 'Repetition Rate Control').

Dispersion Control

A laser pulse that propagates through the fibre temporally broadens due to the dispersion of the fibre material (see sec. 2.1.6). The laser pulses that may have a considerable bandwidth (here, up to 40 nm) are subjected to this dispersion every roundtrip. To realign the dispersed parts of the laser pulse again, a dispersion compensation inside the cavity is needed. In this laser oscillator it is a double pass grating compressor. This is chosen as there exists no dispersion compensating single mode fibre for wavelengths below 1300 nm for fundamental reasons (Beside very new photonic crystal fibres that have other disadvantages such as losses, pulse distortion through higher order dispersion, or splicing difficulty). Thus only bulk optics can be used here. In a grating compressor, the light of a lower wavelength is stronger deflected than the light of a higher

wavelength. If a stretched laser pulse with a positive chirp (That is, 'red' spectral components are leading in the pulse, while 'blue' components follow) is incident on a grating compressor, the leading 'red' spectral components have a longer optical path than the 'blue' ones. The added group velocity dispersion (GVD) of a double-pass grating compressor can be expressed as [3] (using $\omega_0 = 2\pi c/\lambda$)

$$GVD = -\frac{\lambda_0^3}{(\pi c \Lambda \cos(\theta_r))^2}. \tag{4.1}$$

Here $\lambda_0 = 1060$ nm is the central wavelength, $\Lambda = 1.66$ µm (equaling $g = 600$ lines/mm) the distance of the grating periodicity, and $\theta_r = 30°$ the angle between the facet normal of the blazed grating and the diffracted light. Adjusting the grating separation, the amount of anomalous dispersion (that leads to a negative chirp) can be set, the separation is adjustable between 2 cm and 3.6 cm. The GVD of the fibre pigtails of the components (HI1060) has been specified to have a dispersion of $D_\lambda = -38$ ps/(nm · km) which can be transformed using $GVD = -D_\lambda * \lambda_0^2/(2\pi c)$. The dispersion of the active fibre has been assumed to equal that of the HI1060 fibre as no specifications are given by the manufacturer. Using these values, a dispersion map for the laser oscillator can be made up (tab. 4.1).

Repetition rate control

The ytterbium doped fibre laser oscillator is designed to deliver pulses with a repetition rate of 108.33 MHz. This equals the 12^{th} subharmonic of 1.3 GHz, the acceleration frequency at FLASH. An exact subharmonic is needed for synchronisation purposes. The repetition rate of a standard bulk laser depends only on the length of the laser cavity: $f = c/2L$ or, for a ring cavity and a significant part of it fibre coupled, $f = c/L_{opt}$ with $L_{opt} = n_{free} * l_{free} + n_{fibre} * l_{fibre}$, where L_{opt} is the length of the optical path in the cavity, $n_{free} = 1$ the index of refraction of air, l_{free} the length of the free-space part in the cavity, and corresponding $n_{fibre} = 1.45$ and l_{fibre} the index of refraction of the waveguide fibre and its length. L_{opt} is used in tab. 4.1 to calculate the repetition rate. There is no external clock applied to the laser system. The repetition rate is controlled by tuning the cavity length using two mechanisms, a slow one to cancel drifts of the laser frequency relative to the accelerator reference (for

example due to environmental changes in the laser laboratory) and a fast one to compensate for sudden changes produced by shocks. The fast length stabilisation is accomplished using a piezo fibre stretcher. This device stretches the fibre about 10 μm proportionial to an applied voltage of 0 V to 150 V corresponding to a detuning of about $\pm$1kHz. The lowest electromechanical resonance of this fibre stretcher is specified to be at 20 kHz, which sets a upper limit for the excitation of the piezo stretcher and subsequently the cutoff frequency of the control loop. The design cutoff frequency is about 1 kHz as for high frequencies the laser oscillator is very stable (see sec. 5.1.4).

For the slow drift compensation the prototype mentioned above had a motorised delay stage. As a major modification of the oscillator, this delay stage was spared in the new design. Aside the difficult alignment the movement of the stage itself introduced vibrations that had a negative effect on the laser stability. A solution not using any mechanical elements could be found in an active temperature stabilisation. To achieve a good performance of this stabilisation of the lasers' free space and fibre part a redesign of the whole laser housing became necessary. The oscillators optomechanics for the free space part of the cavity is now mounted in a box with thick aluminium base plate, walls and top cover with two compartments. The lower part contains the free space part of the cavity including the fibre collimators (see fig. 4.2). The fibre part of the cavity is loosely laid on an aluminium plate in the upper part of the box. On this plate the resistive heaters and the temperature sensors for the stabilisation are installed. There are no peltier elements that allow for cooling, instead the standard operation temperature of the laser oscillator is raised with respect to the laboratory temperature by typically 5°C. The heating power is low, the maximum chosen to be 15 W, but the thermal shielding (1.5 cm thick rubber foam all around the aluminium box) leads to a low coupling to the environment. Measurements of the performance are presented in section 5.1.5.

4.1.2 Synchronisation

In order to achieve an active stabilisation of the repetition rate a control loop has to be set up. The input for a control loop that has to be established is an electric pulse train created from a part of the pulse train split directly behind the laser oscillator output which is directed onto a biased high band-

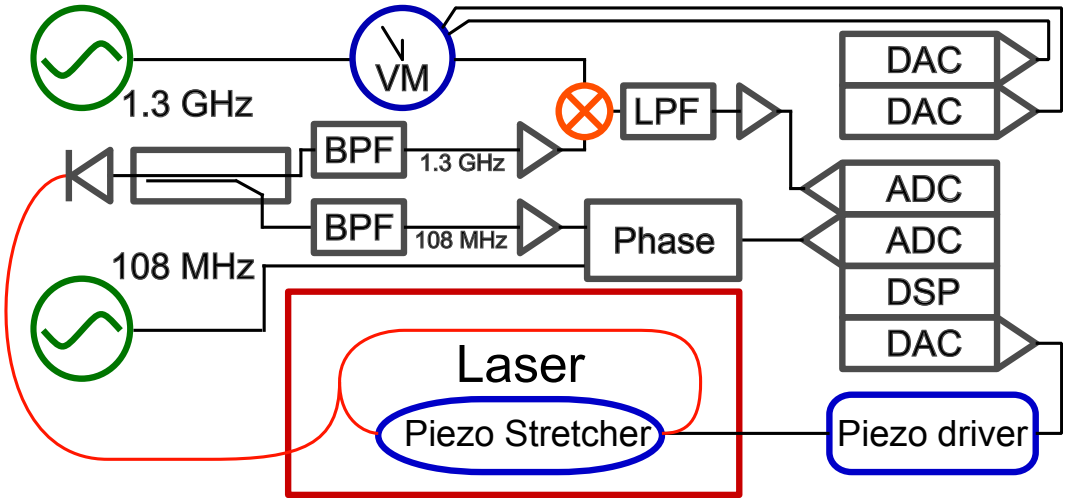

Figure 4.3: Layout of the laser oscillator synchronisation. ADC: analogue-digital converter, DAC: digital-analogue converter, BPF: band pass filter (central frequency depicted to the right), LPF: low pass filter (cutoff frequency 1.9 MHz), VM: vector modulator, DSP: digital signal processor, Phase: slow phase detector

width photo diode (ET3500F, $U_{Bias} = 15V$, cutoff frequency = 12.5 GHz)(see fig. 4.3). This signal is split up to feed a slow phase detector at the fundamental frequency (108 MHz) and a high frequency (1.3 GHz) part for precise synchronisation. The right harmonic of the pulse train for each branch is picked using a band pass filter with the according frequency and amplified. The error signal in the high frequency branch is obtained by mixing the 1.3 GHz retrieved from the optical pulse train with the 1.3 GHz reference from the FLASH master oscillator (MO). The error signal vanishes when the laser pulses have the exact subharmonic (in this case, the 12^{th}) of the FLASH acceleration frequency. The master oscillater (MO) also delivers other reference frequencies throughout the FLASH facility such as 108 MHz. To define the total phase, a slow phase detector (AD9515) is used in the low frequency part. In a multi-step digital regulation algorithm (last version written P. Predki) that runs on a fast digital signal processing (DSP) unit, the laser is locked onto the correct 108 MHz phase and then to the next 1.3 GHz zero crossing. This is achieved by acting on the piezo stretcher in the oscillator cavity using a digital/analogue converter (DAC) and a piezo driver unit. If the laser is to be shifted with respect to the electron bunch, the 1.3 GHz signal coming from

the MO is phase shifted using a remotely controled vector modulator (VM).

4.1.3 Amplifier and Gating

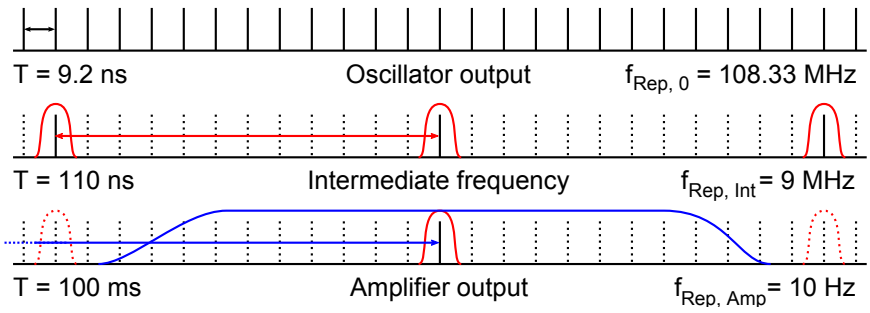

Figure 4.4: Gating scheme suited for electro-optic spectral decoding. The intermediate frequency can vary between the full oscillator repetition rate and 1 MHz, 9 MHz has been chosen for taylored SPM optimisation. The amplifier output frequency can be varied between 10 Hz and 1 MHz to adapt to the readout of the experiment conducted.

The oscillator delivers pulses with an energy of about 0.5 nJ of which a significant part is used for the synchronisation. To achieve the needed pulse energies of more than 5 nJ, a repetition rate that matches the capabilites of the readout system of the EO setup, a bandwidth needed for the actual EO experiment, the correct pulse length and a low background, a two stage amplifier was constructed. The layout of the amplifier scheme is depicted in fig. 4.5. The input 'Osci Out' corresponds to the 'Osci Out' output of fig. 4.1. The laser pulse train that exits the oscillator is split up with a fixed splitting ratio which is defined using a λ half wave plate and a polarising beam cube. Both parts are coupled into a fibre, one part is used for synchronisation and directed onto a photodiode, the other part is fed into a booster amplifier. The pulses have a positive chirp when they leave the oscillator, further dispersion in the preamplifier adds more chirp to the pulses. The pulse energy is increased by a factor of 10 in the gain fibre (optically pumped with an equal laser diode as the oscillator, length of the gain fibre: 45 cm). As the booster amplifier is operated at the full repetition rate, no isolator is needed to prevent ASE light from traveling backwards and disturbing the oscillator. ASE is an acronym for amplified spontaneous emission and describes the radiation

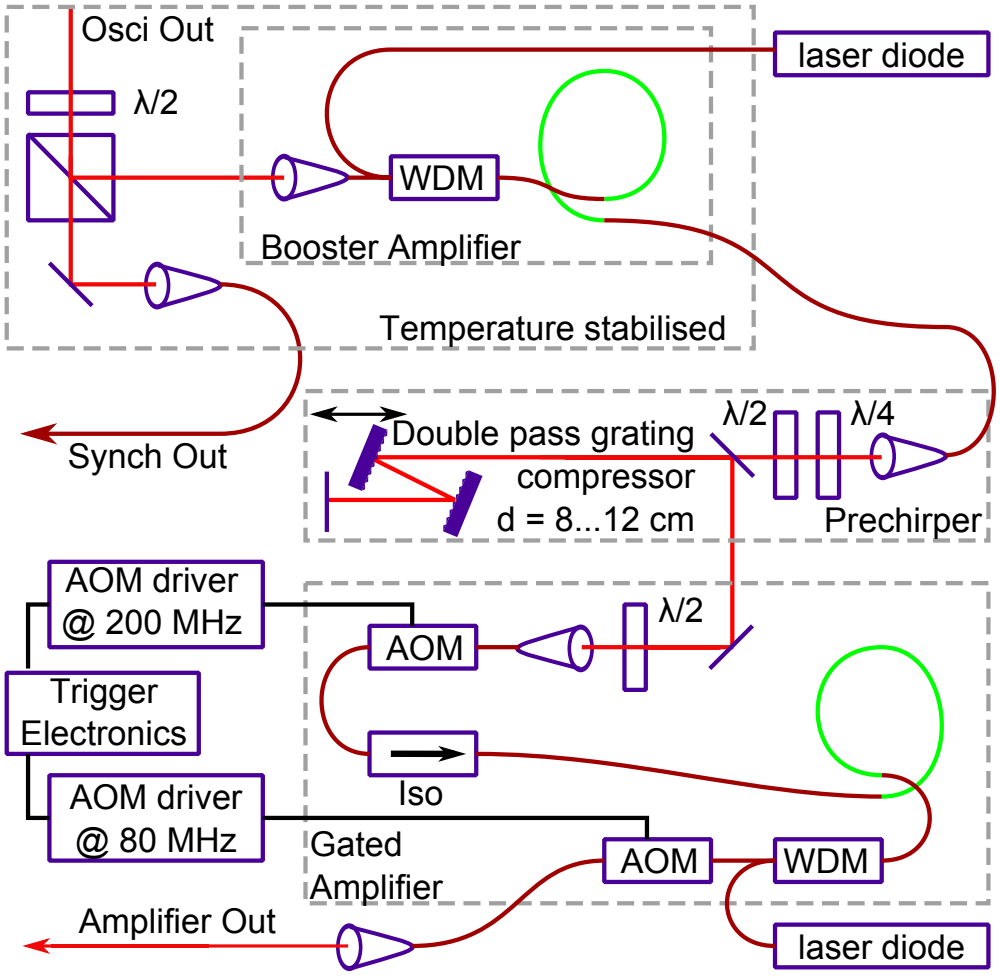

Figure 4.5: Layout of the two-stage ytterbium doped amplifier. The first stage is a booster amplifier operated at the full repetition rate. A grating compressor overcompensates the postive chirp of the laser pulses. The gated amplifier is operated at 9 MHz behind the first AOM (acousto-optic modulator). Nonlinearities occuring due to the high power of the short pulses are used to enhance the spectral bandwidth via self phase modulation (SPM). The last AOM supresses unwanted background light (ASE) and produces a 10 Hz pulse train.

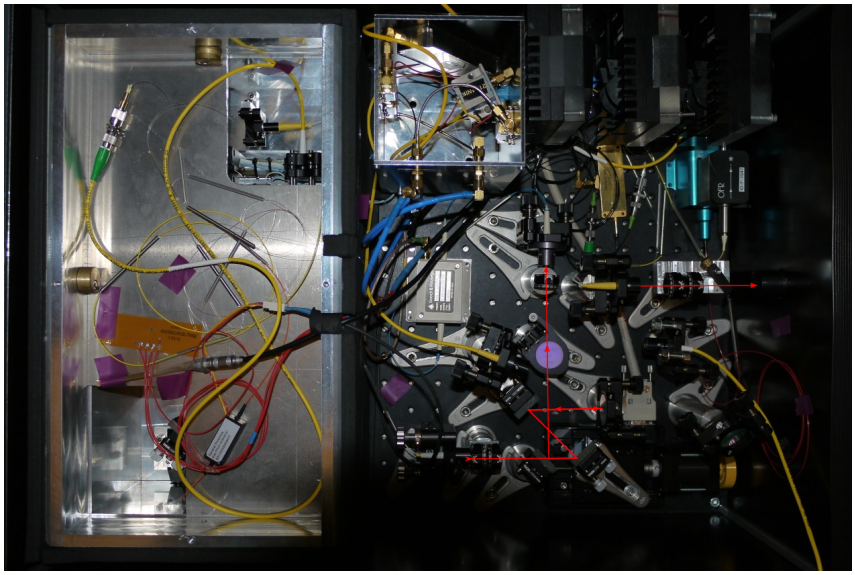

Figure 4.6: Photograph of the YDFL system. To the left, the open oscillator box can be seen with its thick aluminium walls, the rubber foam isolation, and the fibre compartment. In the upper right, there are the three laser diode mounts in the upper part next to a box with RF lock electronics. In the lower part, the prechirper double-pass grating compressor can be seen together with some optics for diagnostic purposes that are permantly installed. The free-space exit of the YDFL system is to the right.

occuring in a pumped fibre where the population inversion is not depleted by a seed laser pulse. The active medium starts to emit cw light at the natural emission wavelength with a broad spectrum (for ytterbium, this is 1030±15 nm). Beside this ASE radiation, a laser breakthrough can happen: If at the ends of the amplifier a fraction of the light is reflected (at splices of minor quality or inside collimators), a parasitic lasing process can build up using this low-Q cavity. This lasing process also produces unwanted radiation in both directions of the amplifier and can thus harm the pump diode of the amplifier or disturb the oscillator as it is of small bandwidth and high power. The ASE radiation poses a problem whenever an amplifier is operated at low repetition rates. At 108 MHz, the inversion population cannot build completely up between to seed pulses, so no ASE light is expected. The laser pulse train has an arbitrary polarisation state when it leaves the booster amplifier, as it is made from standard single mode fibre. The laser pulse energy is now about

1 nJ and the pulses are stretched with a positive chirp due to material dispersion in the oscillator and the booster amplifier. Before the pulses enter the prechirper the polarisation state is set to horizontal as the grating compressor then reaches its maximum efficiency. In this compressor the positive pulse chirp is overcompensated so that the pulses have a negative chirp when they enter the gated amplifier. The pulse length at the exit of the prechirper depends on the grating separation which is remotely controllable. As in the intracavity grating compressor, standard Thorlabs reflective gratings with 600 l/mm are used having a specified efficiency of 85% in the first order. This results in 50% total efficiency of the prechirper. The pulse train now enters the gated amplifer which is constructed using polarisation maintaining (PM) fibre. This kind of fibre intentionally breakes the symmetry of the usual single mode fibre by introducing a stress element. It induces a strong birefringency in the fibre, defining two axes along which the light wave can propagate, a slow axis and a fast axis. To hit only one (the slow) axis, a λ half wave plate is used to match the polarisation plane of the incident light to the orientation of the PM fibre collimator. If linearly polarised light is coupled into a PM fibre at an angle between the fast and the slow axis, the pulse is divided into its projected polarisation components and reaches the end of the fibre as two pulses following each other. The pulse train now is gated in an acousto-optic modulator (AOM). This device serves as a fast optic switch. It consists of a GaP crystal with two supersonic transducers glued to it. A pulsed high power RF drive signal originating from a power RF driver (200 MHz, 5 Watt) excites the transducers, leading to a traveling sound wave in the GaP crystal. When this sound pulse is timed with an laser pulse, the regular density variation in the crystal induced by the sound wave serves as a bragg grating for the light wave. The laser pulse is deflected such that it enters the exit fibre. If no sound wave is exited, the laser pulse does not hit the exit fibre. The on/off ratio of these devices is rather good, surpressing the unwanted pulses to a high degree (more than 45 dB). The overall insertion loss is depending on the switching speed: For a high switching speed, the laser light needs to be focused down to a small focus, as the sound velocity in the crystal limits the rapidity with which the traveling sound wave can uniformly spread over the area of the laser focus. However, for bulk devices this leads to a small aperture, and for fi-

bre devices to higher coupling losses. In the first AOM (insertion loss 3 dB) the laser pulse train is gated down to a repetition rate of 9 MHz. At this rate the backtraveling ASE light from the pumped gain fibre may already be a problem, thus an isolator is used to surpress disturbances. The gain fibre (Coractive Yb 500, the PM equivalent to the SM Yb 164 gain fibre used in the oscillator and the booster amplifier) is again optically pumped with an equal laser diode as the oscillator (max. 600 mW cw laser light at 976 nm in a single mode fibre, 950 mA pump current). Here, the gain fibre is pumped in a counterpropagating direction. This leads to a stronger population inversion at the end of the gain fibre where the incident gated laser pulses already have gained some energy. A gain profile with a maximum at the end of the gain fibre is thus produced. As the pulses enter the gated amplifier with a negative chirp and the chirp due to material dispersion is positive, the length of the laser pulses initially decreases (see sec. 2.1.6). The pulses are amplified in the active fibre and become shorter due to the cancellingof the initial chirp, thus strong nonlinear interaction can be exspected. The main effect is the self phase modulation (SPM, see sec. 2.1.7) that leads to new frequency components on the steep edges of the laser pulse. The strength of the effect can be tailored by controling the amount of chirp of the incident laser pulses and the pulse energy which is determined by the booster and gated amplifier pump power. The incident laser pulses have a spectral bandwidth of about 20 nm FWHM due to gain narrowing in the booster amplifier, the spectral width can be expanded to more than 50 nm FWHM (See sec. 5.2.2 for measurements). As the EO setup readout cannot handle the intermediate frequency of 9 MHz, the second AOM operating at a lower sound frequency of 80 MHz is used to produce a 10 Hz output. The insertion loss of the slow AOM is about 1.5 dB and it has a switching speed of 20 ns (10% to 90% rise time). This second AOM also suppresses unwanted ASE light in forward direction.

4.2 EO at 140 m

The experimental area at 140 m at FLASH together with its junction to the laser laboratory in building 28g was originally set up for experiments using a Ti:sapphire amplifier and thin electro-optic crystals to push the borders of the temporal resolution of electro-optic electron bunch diagnostics. These experiments are still a benchmark in the field as the fundamental limits posed by the phonon resonances in the crystal were essentially reached [74]. Bunch features as short as 60 fs have been measured. The infrastructure built for these experiments is flexible and allows different other experiments using the same equipment with slight changes. For this thesis it was adapted to an ytterbium fibre laser based spectral decoding experiment, an EO setup having different fundamental constrains so that lower temporal resolutions are to be expected (see sec. 2.3.7). Nevertheless the new laser system is capable of prolongued operation and thus facilitates the possibility of a longitudinal bunch shape monitor which had to be tested. The laser system and the readout together with the needed electronics is situated in the laser laboratory 28g, while in the accelerator tunnel a second optical table is installed holding the vacuum chamber with the EO crystals. The laser transfer line facilitates the transport of the laser pulse trains to and from the tunnel.

4.2.1 The Laser Transfer Line

The transfer line consists of four mirrors installed in a u-shaped pipe with a diameter of 12 cm, two of the mirrors are gold-coated off-axis parabolic mirrors with a focusing length of 6 m and a projected diameter of 6 cm (refer to fig. 4.7). These mirrors enclose the main beam pipe of 12.15 m length that traverses the radiation shielding of the FLASH tunnel. They form an approximate 2f setup and are remotely controlable to adjust the beam path through the transfer line. The other two mirrors are plane mirrors and installed over the ends of the transport line, each attached to the associated optical table to minimise vibrations and thus beam pointing instabilites. Indeed the beam path of the YDFL laser system is very stable, taking the 0.16 mm^2 detector area of a photodiode inside the tunnel as position reference, no drift of the beam path from the YDFL laser system into the tunnel occurs over a

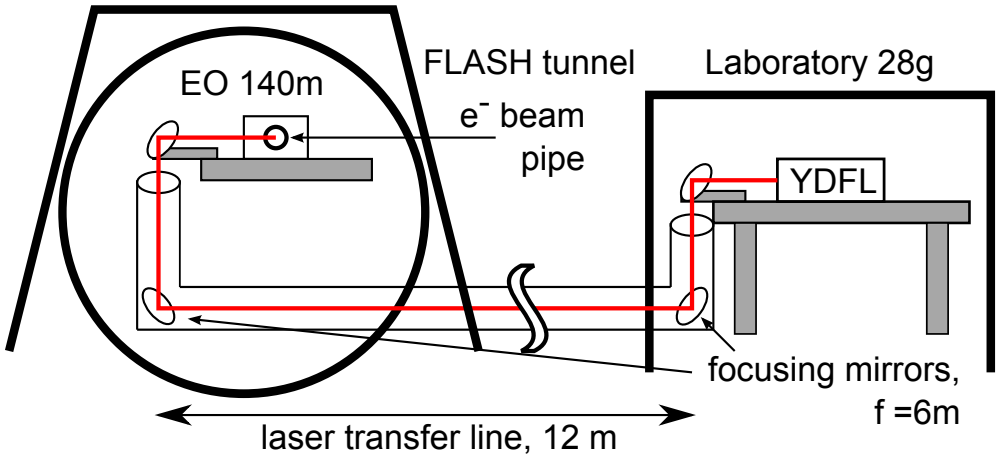

Figure 4.7: Cross section of the laser laboratory, the FLASH tunnel and the laser transfer line. Not to scale.

length of more than 20 m and a duration of months. The prior used 4f setup with intermediate lenses and the possibility of evacuating the beam transfer line for high power pulses has been altered to allow a beam transport with minimised dispersion acting on the laser pulses to also facilitate electro-optic sampling experiments. The lenses have been taken out and the two vacuum windows at the ends of the beam pipe of the old setup have been repaclaced by pellicels (foils originally intended for beam splitting). The pellicles have a high transmission and a minimum thickness (about 2 µm). Even though the transfer line is not evacuated as was needed for the high peak power pulses from the Ti:sapphire amplifer, a closure of the ends is still necessary for two reasons. First, there might be air pressure differences between the laser laboratory and the accelerator tunnel, leading to air flow through the laser transfer line. This needs to be avoided as such a flow might disturb the laser pulses. Second, the accelerator tunnel is a place with a high amount of dust particles in the air. The upward pointing end part of the tunnel side laser transfer line works as a downpipe for dust particles that accumulate on the gold coated mirror when no precautions are taken.

4.2.2 Setup in the Tunnel and the Vacuum Chamber

As the part of the laser transfer line between the two focusing mirrors is not exactly 12 m long and the focusing length of the mirrors is not optimally matched

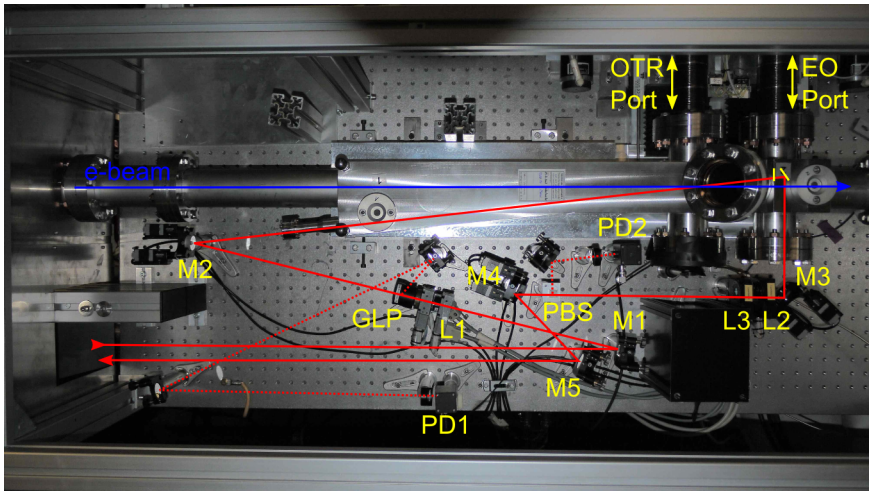

Figure 4.8: Photograph of the EO setup in the tunnel at 140 m. M1-M5 mirrors, L1-L3 waveplates, PBS polarising beam splitter, GLP Glan Laser prism. The EO crystal and the successive mirror are drawn in yellow at the EO port. For a beam path consideration see text.

and due to the inherent broadening the laser arrives on the optical table in the tunnel with a diameter of about 10 mm ($1/e^2$) which is still acceptable with 1 inch optics. The situation on the optial table in the tunnel is depicted in fig. 4.8. The exit of the laser transfer line is on the left. Its upper mirror on the tunnel side is turned by 90°, and so is the polarisation plane of the laser pulses. This is corrected for with a λ half wave plate (L1) and verified by a Glan laser prism (GLP, coated Glan Thompson prism). The wave plate mount is motorised, so the splitting ratio at the beam cube can be set remotely. The vertically polarised part is directed onto a fast photodiode (L1, bandwidth 12.3 GHz) and used for a laser pulse alignment and arrival time check. The horizontally polarised laser pulses are directed on a motorised focusing mirror (M2) with a focusing lengh of 1 m directly before the entrance window to the vacuum chamber. The laser pulses cross the beam path of the electron bunches and are focused onto the EO crystal. If the screen at the OTR port is not moved into the electron bunch beam path, the electron bunches pass the electro-optic crystals mounted at the movable EO port. There are two different crystals mounted on the crystal holder: a thin galliumphosphide (GaP) crystal without any coating in the lower place with a nominal thickness of 0.2 mm (measured: 185 μm), and a thick GaP crystal (0.5 mm) in the upper place with

an antireflection coating for light of 1030 nm at the back plane. If the electron beam orbit is centered in the beam pipe, each crystal has the same distance to the electron beam. The laser pulses that traverse the electro-optic crystals a few millimeter from the edge are reflected out of the vacuum chamber by a mirror mounted directly behind the electro-optic crystal (yellow). The total distance between the electron bunches and the laser spot on the crystal is not more than 5 mm. The motorised mirrors M2, M3 and M4 are used to switch the beam path of the laser from the upper to the lower crystal. The laser beam has a small diameter when it exits the vacuum chamber as the window is only some centimeters behind the focus on the crystal. A $\lambda/4$ wave plate (L2) is used to account for residual birefringence of the EO crystal and a motorised $\lambda/2$ wave plate defines the polarisation state at the following polarising beam splitter cube (BPS) which acts as the analyser in the EO setup. Here the polarisation modulation imprinted onto the laser pulse is converted into an amplitude modulation. The laser light of the unused vertical polarisation is directed onto a second photodiode (PD2) to check for the correct waveplate setting of L3. The laser beam broadens until it hits the next focusing mirror (M4) that collimates the beam. It then is redirected to the laboratory using the laser transfer line. On the way back, the off-axis parabolic mirrors in the beam line are hit off-centre which leads to a slight beam distortion in the laser lab.

4.2.3 Readout and Temporal Overlap

In the spectral decoding setup, the spectral components experience a different amplitude modulation. The readout is done with a grating spectrometer (600 l/mm, blazed for 1 µm) and a 512 pixel wide cooled InGaAs CCD array (Andor IDus DU490A-1.7), both situated in the laser laboratory. The camera has a minimum exposure time of 1.4 µs, so it can neither be operated at the full YDFL repetition rate of 108 MHz nor at the full intra-bunch repetition rate of FLASH (1 MHz). Averaging over unmodulated laser pulses needs to be avoided as the signal to noise ration would drop unacceptably. Instead, the laser pulse is gated down to 10 Hz and background laser light is thus supressed. The camera is integrated in the accelerator's control system (DOOCS) and the data aquisition system (DAQ). The low repetition rate also allows for saving

data series 'manually', i.e., script-based via DOOCS.

Finding the temporal overlap of the electron beam and the laser pulses at the place of the electro-optic crystal is done in a two-step approach. A rough timing is provided by a cable antenna wrapped around the window opposite of the OTR port. The transient electric field carried by the bunch is picked up with this antenna. The cable also connects to the photodiode PD1. Both signals (from the laser pulses and the electron bunches) are joined in one cable. With an oscilloscope the overlap of these two signals can be tested with an accuracy of 200 ps. The cable and light path lengths need to be taken into account when calculating the needed spacing of the signal scope traces that corresponds to a temporal overlap of the electron bunches and the laser pulses at the EO crystal. The accuracy of this method is limited by the correctnes of the measurement of the light path (which is some centimeters), the unknown duration of the converting of the laser pulses to electric pulses in the photo diode, and the limited bandwidth of the pick up antenna. The second step is a fine timing scan: The laser pulses are shifted with respect to the electron bunch in small steps and the spectrum of the laser pulses is recorded. This needs to be done for a broad time window when the overlap needs to be found for the first time. If this is accomplished once, the timing of the accelerator to the laser changes only by small amounts in the range of less than 100 ps.

4.3 EO at BC2

4.3.1 General design

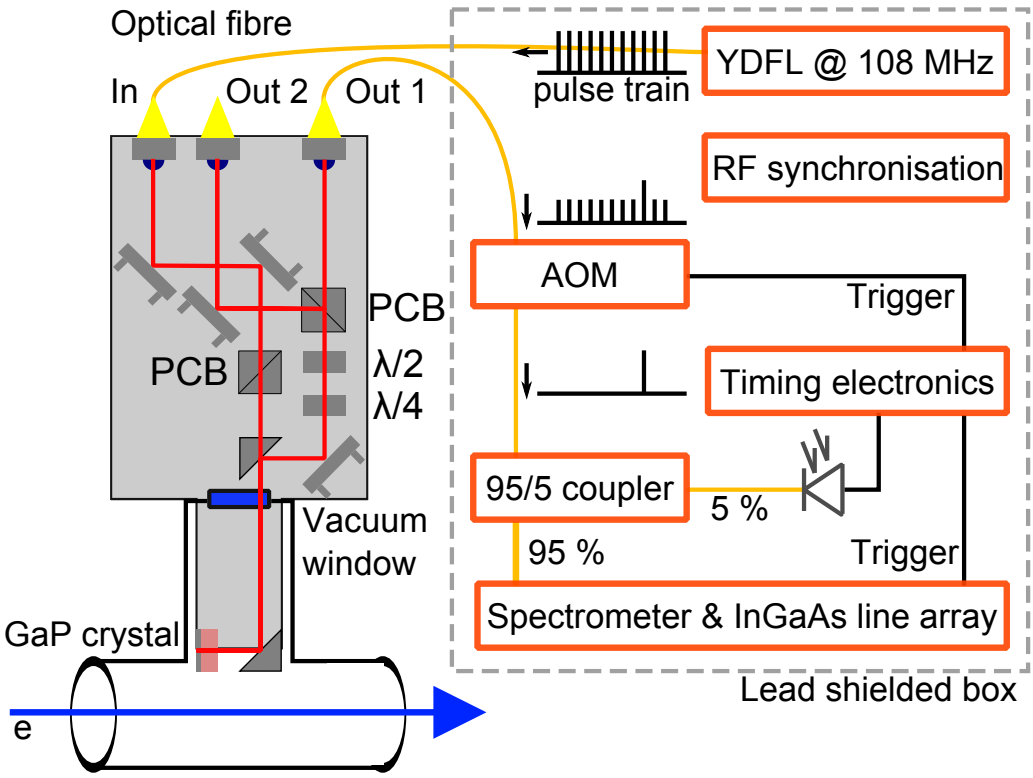

Figure 4.9: Layout of the electro-optic spectral decoding setup at BC2. On the left, the electro-optic frontend holding a 5 mm thick GaP crystal is drawn. The laser system, electronics and readout camera are placed in a lead shielded box next to the setup inside the accelerator tunnel.

The development of robust short pulse fibre laser systems allows the application of these systems inside the accelerator tunnel, where maintenance access is restricted to a few days per month. Together with a newly designed frontend (Bernd Steffen et al, see [76]), a small and robust electro-optic bunch length monitor has been constructed and comissioned (mainly by J. Breunlin, see [12]). To achieve the goal of installing an operator friendly bunch length monitor, a comercially available fibre laser system is used, the necessary trigger and synchronsation electronics have been installed, and the gating and readout has been established. These components will be shortly adressed here. The general design (sketched in fig. 4.11) makes use of the two main features of the

Pulse energy	1.5 nJ
Spectral bandwidth	40 nm (FWHM)
Central Wavelength	1050 nm
Pulse duration	< 5 ps (FWHM)
Repetition rate	108.33 MHz
Repetition rate tunability	$\pm$ 200 kHz
Integrated timing jitter (1 kHz - 10 MHz)	< 50 fs
Fibre type at main output port	Polarisation Maintaining

Table 4.2: Specifications of the Orange SA ytterbium doped fibre laser system

laser system: The robustness of it allows to place it inside the tunnel, enabling a completely fibre based laser pulse train transfer to and from the electro-optic frontend. And on the other hand, the bandwidth emitted by this oscillator is sufficient for single shot electro-optic spectral decoding of electron bunches not too short. Thus, the new monitor has been installed behind the first bunch compressor (BC2), where the electron bunches are not fully compressed and have a typical length of 1.5 ps (rms). All necessary hardware is installed inside a lead-shielded box with a size of about 1 cubic meter right next to the electron beam pipe and the electro-optic frontend.

4.3.2 Laser system

The purchased laser system is an Orange SA fibre laser bought from Menlo Systems, Munich. It is a stretched-pulse ytterbium doped fibre laser (YDFL) and equals in the design the self-built YDFL oscillator (see chapter 4.1). It also comes with a booster amplifier to achieve output pulse energies of 1.5 nJ at the full repetition rate of 108.33 MHz. The output on the main port is fibre coupled as is needed for this setup. The laser system has been characterised in the above mentioned diploma thesis [12], its main specifications are listed in tab. 4.2. The synchronisation of the laser system to the accelerator has been copied from the self-build system (fig. 4.3) and makes use of a second laser output with a smaller pulse energy of about 0.02 nJ. A useful feature of the laser system is its software enabling remote control of the oscillators modelock state and the system diagnostic as well as operation of the booster amplifier.

4.3.3 The Electro-Optic Frontend

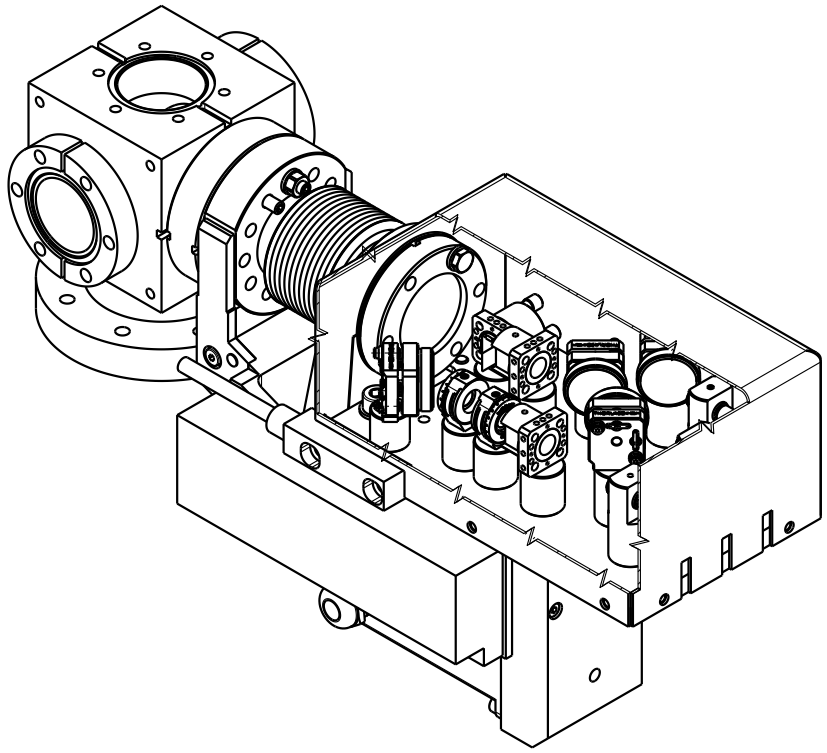

Figure 4.10: Technical drawing of the electro-optic frontend. In the right part the optical components on their base plate are shown. Inside the bellow behind the vacuum window the crystal holder is mounted in a fixed position relative to the base plate. The cube with five vacuum flanges (electron beam pipe not shown) has a side length of 7 cm. On the bottom the motor can be seen that places the EO crystal together with the base plate relative to the electron bunches (By courtesy of B. Steffen).

The electro-optic frontend has been designed at the PSI by B. Steffen et al and has been tested at the Swiss Light Source (SLS) and is foreseen as part of the special diagnostics for the European X-FEL (Hamburg). In difference to the experimental area at 140 m in FLASH, it is not intended as a flexible multi-purpose infrastructure but is an engineered device of small size. It consists of a base plate for the optics outside the electron beam vacuum, a vacuum window, the crystal holder with a mirror, all of it mounted on a motorised sledge (see the technical drawing in fig. 4.10). As the optics base plate and the crystal on its holder are both fixed on the motor sledge, the alignment

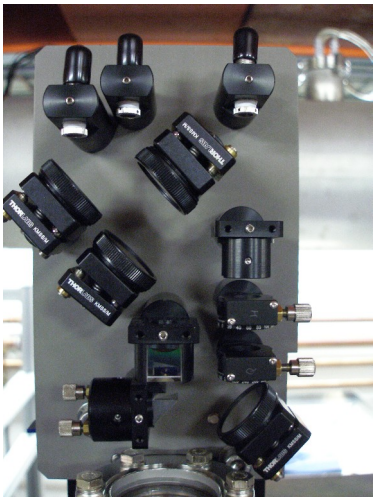

Figure 4.11: Picture of the optic components mounted on the base plate of the electro-optic frontend. The vacuum window can be seen on the bottom as the whole frontend is installed above the electron beam pipe.

of the optic is fixed too, this allows for repositioning the electro-optic crystal relative to the electron bunch orbit while the system runs. The optics base plate is equipped with all the necessary bulk-optics for the spectral decoding setup. The laser pulse train arrives from the laser system through a 2 m long polarisation maintaining (PM) single mode fibre (In the first setup, this was one meter of fibre. To gain a broader time window whithin which a signal can be recorded, one meter of additional fibre was installed. The additional material dispersion leads to a longer duration of the chirped laser pulse). Another meter of equivalent fibre comes with the fibre collimator, making it three meters of optical fibre in total. The polarisation plane is adjusted to horizontally by turning the fibre collimator in its mount. The laser pulse train is now directed through a polarising beam cube (PCB) and the vacuum window into the beam vacuum. It is reflected on a mirror that is mounted downstream the electro-optic crystal. On the entrance facette, the crystal is anti-reflection coated for light of 1030 nm. The laser pulses propagate in the opposite direction than the electron bunches through the crystal and are reflected by a reflection coating on the opposite crystal surface which is coated for a good THz transmission. The crystal has a thickness of 5 mm, changed from the previous version with a thickness of 0.5 mm. In the former version reflections of the THz field in the crystal led to an artifact signal about 11 ps after the main signal, disturbing

the data acquisition. This artifact is not avoided but shifted to 110 ps after the main signal. As the modulation strength grows linearly with the crystal thickness, a stronger signal can be exspected in the new configuration. On its way back, the reflected laser pulse propagates parallel to the electron bunch and is modulated by the electro-optic effect. The electro-optic crystal is mounted under a slight angle with respect to the plane perpendicular to the optical path, so that the reflected laser pulses do not hit the input collimator of the electro-optic frontend but a pair of mirrors that guides it through a pair of motorised retarder wave plates (a λ quarter wave plate for compensation of the residual birefringence of the EO crystal and a λ half wave plate for defining different measurement setups). Both of these retarder wave plates are motorised and can be remotely controled. The standard measurement configuration is the near-crossed polarizer setup with an angle of $\theta = 9°$ of the λ half wave plate (see sec. 2.3.6). Behind the retarder wave plates the analyser beam cube (another PCB) turns the polarisation modulation of the laser pulses' spectral components into an intensity modulation. Both parts of the splitted laser beam are fed into single mode fibre (non-PM) via two collimators and transportetd back to the lead shielded box, but only one of them is used for further processing. The readout system is similar as in 4.2.3, consisting of a spectrometer (Andor Shamrock SR-163 with 600 l/mm grating blazed for 1 µm), and the same InGaAs line array camera (Andor Idus D490-1.7A) which is integrated into the control system. These two components fit well in the lead shielded box for their compact size and were chosen for long-term use. As at 140 m, a pulse picking device is needed as the camera cannot handle the full laser repetition rate (see below).

4.3.4 Timing Overlap and Triggering

As with the experimental electro-optic setup at 140 m, the timing of the different devices is of importance, but the installation in the tunnel necessitates a mostly remotely controllable system. The synchronisation scheme is equivalent to the one depicted in fig. 4.3, assuring the stable phase relation between the laser pulses and the accelerator driving RF (and thus the electron bunches). A machine trigger activates the fast AOM for pulse picking and the readout camera. The AOM is of the same kind as the fast AOM in the self-build YDFL

system (see sec. 4.1.3). A difference to the EO setup at 140 m is that the electro-optic frontend of the compact monitor at BC2 is operated at 108 MHz and the pulse picking is done just before readout.

The correct delay between the 10 Hz machine trigger and the activation of the AOM to open the optical gate needs to be found and set on a nanosecond scale (remotely controlable, as far as possible). Therefore a part of the gated pulse train is directed onto a fast photodiode whose RF signal is amplified, broadened (to account for the lower bandwidth of the digitalisation) and fed to an ADC (analogue/digital converter). A signal originating from a pick up antenna installed at the elelctron beam pipe near the frontend also amplified and fed to the same ADC card. In scanning the delay of the ADC card with respect to the electron bunches and the laser pulses that have a fixed phase relation, the relative position of the two signals from the photodiode and the pick up antenna can be measured. Taking into account the cable lengths and optical paths, the needed spacing between the two signals that corresponds to an overlap at the EO crystal position can be set. The accuracy of this method is in the range of a nanosecond, where the main limitation arises from the stability of the machine trigger. As the electron bunch and the laser pulse lengths are on the order of ten picoseconds, a fine scan of the laser against the electron bunches is needed after establishing the coarse overlap.

Chapter 5

Characterisation of the YDFL System

5.1 Oscillator

5.1.1 Starting Up the Oscillator

After setting up the oscillator and alignment of all optical components, cw lasing can be turned on and the slope efficiency can be measured (see section 2.2.4) to get a first impression of the quality of the laser resonator. For this measurement, the pump current of the laserdiode pumping the active fibre in the oscillator is stepwise increased (fig. 5.1). The laser output power is measured (in this case, with a Thorlabs PM100A with a S132C power sensor, Ge photodiode, uncertainty 700nm - 1100 nm: 3%). The measurement has been done twice: once for a waveplate setting in which modelock has been established beforehand (due to the hysteresis of the modelock operation state, the measurement could be done up to high pump currents in cw mode). This corresponds to the blue curve with a slope efficiency of ≈ 11.5 %. For the black curve the waveplate setting has been optimised for output power, here a slope efficiency of about 25 % has been measured. Turning the waveplates alters the coupling ratio at the output port and thus modulates the cavity finesse. In this thesis, the cw output power is of minor interest to other parameters such as spectral bandwidth of the emitted pulses, low noise and long-term stability of the operation state. Thus, the waveplate setting will be optimised for these

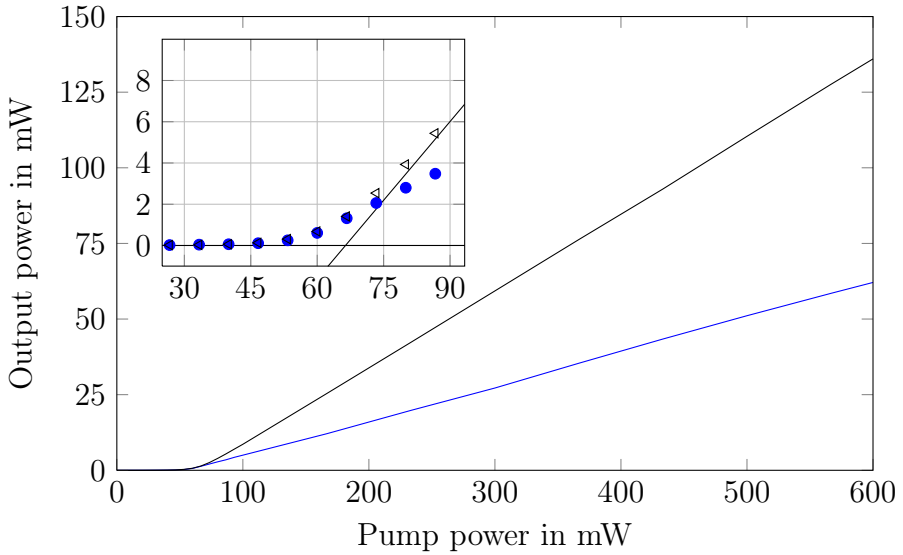

Figure 5.1: Measurement of the laser threshold and the slope efficiency. The inset is an enlargement of the threshold region including a linear fit for the black curve prolongued to the left.

parameters and not primarily for a good slope efficiency. Both plots lead to a laser threshold of about 45 mW. This relatively high laser threshold is due the high cavity losses mediated by the grating compressor (50 % efficiency), low incoupling at the intracavity collimators and the large outcoupling ratio.

5.1.2 Modelock Search

The second step in setting up the oscillator is to reach for a pulsed operation state. In principle, the modelock is self-starting when the correct waveplate setting is achieved. This waveplate setting is not known beforehand as the evolution of the polarisation state inside the fibre is arbitrary. Thus it cannot be calculated and must be found experimentally. To avoid time consuming manual adjustment, a partially automated procedure has been established. Three different signals are validated using parts of the RF lock electronics (refer to fig. 4.3): One photodiode is used to monitor the DC signal of the laser output. Also, the photodiode used for the RF lock circuit gives two signals, one at 1.3 GHz and one at 108 MHz (the slow phase detection). In fig. 5.2, the trace of the signal acquired from the latter is plotted. During a scan, the four waveplates in the oscillator are turned with different angular velocities

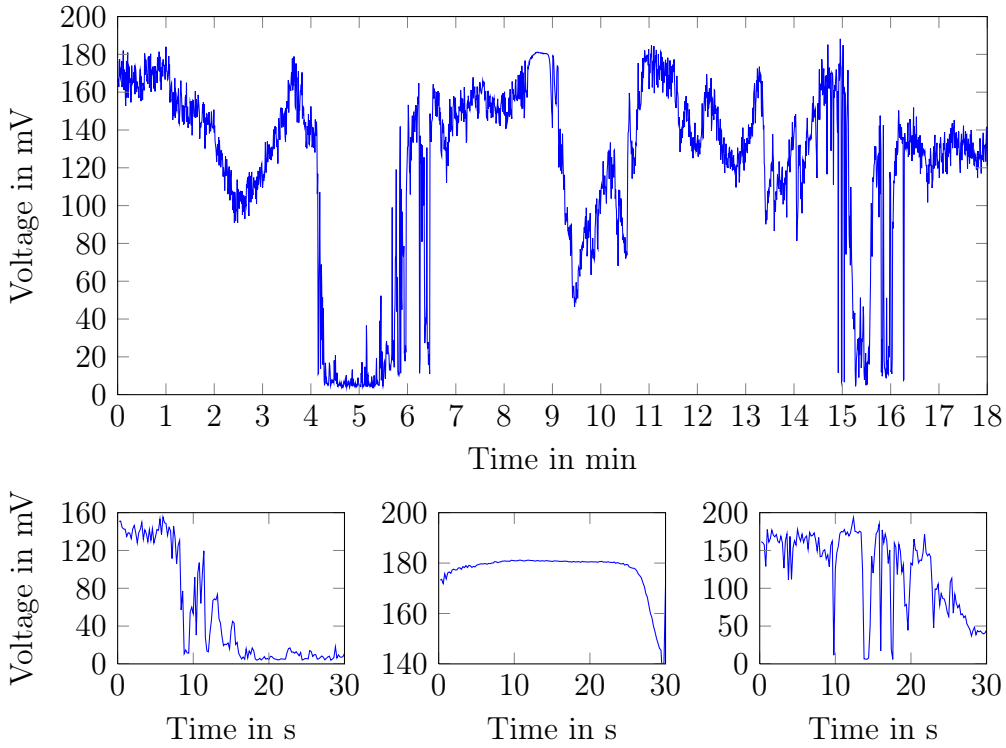

Figure 5.2: Scan of the waveplates in the oscillator to find a modelock state, the 108 MHz component of the laser output is shown. The plots beneath show magnifications of (left) the steep edge at 4 minutes, (center) the flat part before the ninth minute, (right) the strong modulations around minute 15. Further explanations see text.

(any velocity ω_0 times four different prime numbers to avoid recurring waveplate settings, in this example $[\omega_{\lambda/4,1}\ \omega_{\lambda/2,1}\ \omega_{\lambda/2,2}\ \omega_{\lambda/4,2}] = \omega_0 \cdot [5\ 11\ 13\ 7]$). The pump power delivered to the oscillator is set to a high value (here: Diode current of 700 mA corresponding to $\approx$ 460 mW laser power) which leads to a stronger noise in the cavity and facilitates the start of the modelock. The scan shwn here took 18 minutes to accomplish. The signal shows strong irregular oscillations due to two different mechanisms: First, even in cw operation different longitudinal modes are excited depending on the waveplate setting. Sometimes strong beating at the natural mode separation of 108 MHz occurs, giving rise to quick changes in this measurement (for example as around minute 15). Second, the outcoupling ratio is varying with the waveplate setting, causing slow changes in this measurement (see first three minutes). The three little

plots show magnifications of different parts of the above plot. On the left, the steep edge at about 4 minutes is shown, showing the signal drops in irregular steps. In the centre inset the flat part before the ninth minute is enlarged. Here, not any modulation can be seen for about 30 seconds, giving rise to the assumption that the laser is in a stable regime at that point. Pulsed operation can be assumed as the signal of the 108 MHz component is constantly high. On the right, the strong modulations around the 15 minute mark are plotted. The chaotic behaviour of this nonlinear system is illustrated well. Setting the waveplates to the values of the flat region around minute nine after the scan is finished, the laser is found to be pulsing.

5.1.3 Pulsed Operation

Time Domain Picture

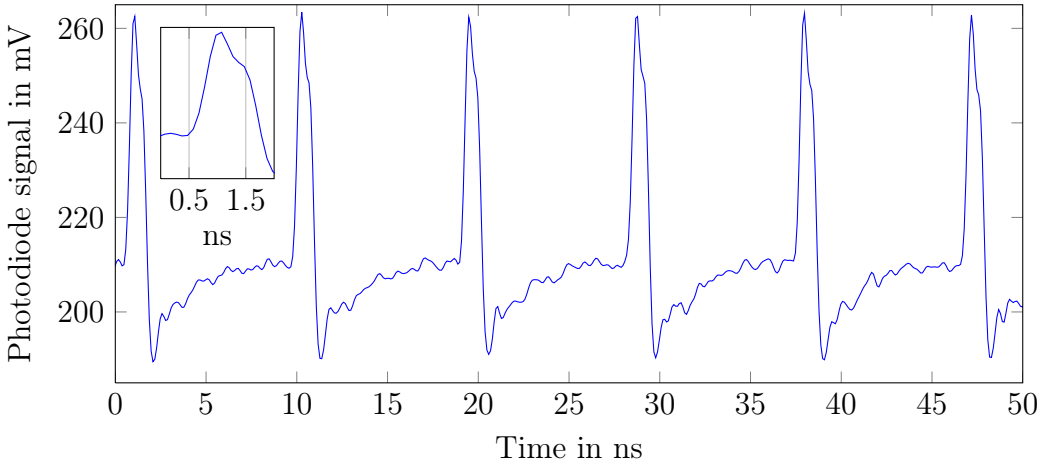

Figure 5.3: Pulse train acquired from the laser in the mode lock state found above. The inset shows a magnification of the first pulse. It can be seen that the resolution maximum of the oscilloscope (10 GigaSample per second, 100 ps/pt) is reached.

An examination of the laser pulse train with a fast photodiode (InGaAs, ET3500F, bandwidth >12 GHz) and a fast digital oscilloscope gives a first impression of the quality of the modelock state. In fig. 5.3 the pulse train acquired in the above found modelock state is plotted before reducing the

pump power. It can be seen that the pulses are very regular in shape and amplitude, they have a steep rising edge, whereas the typical exponential decay of the photodiode signal can not be seen. Two things are important: first, the resolution limit of the oscilloscope (in this case, 10 GSample/s or 100 ps per point) is reached. Second, as can be seen in the inset, a double pulse operation state with a pulse separation of less than 0.5 ns can not be ruled out. From the time domain measurement, a first estimate on the repetition rate of the laser can be made. The separation of the pulses in fig. 5.3 is about 9 ns. The oscilloscope measurement routine calculates a frequency of the pulse train of 108.3558 MHz with a standard deviation of 109.1 kHz, using 30k samples, which is going to be fine tuned.

Optical Spectra

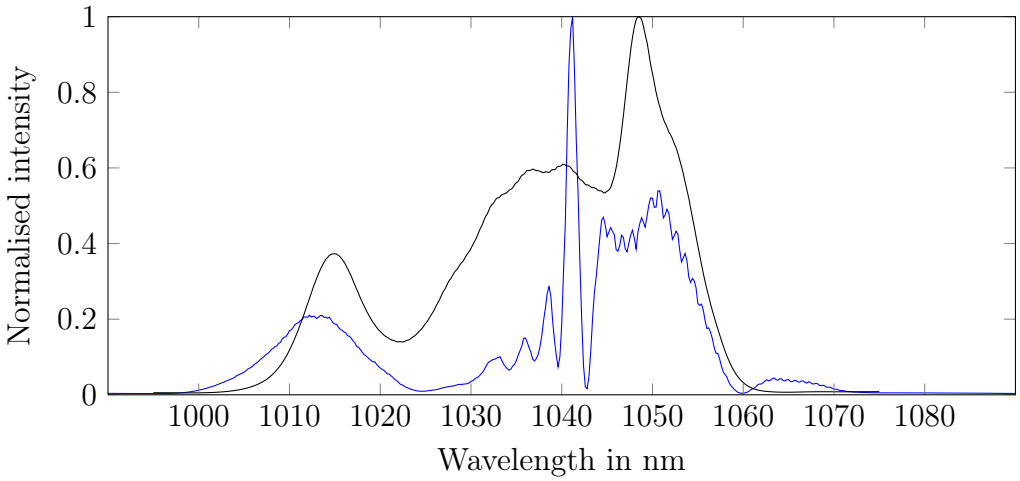

Figure 5.4: Normalised spectra taken at the synchronisation output. With Modelock search pump current (700 mA), blue, and standard operation current (250 mA), black.

The optical spectrum emitted by the laser when pumped with the pump current used for the modelock search (700 mA) is seen in fig. 5.4 (blue curve). A main peak at 1040 nm is surrounded with two broader peaks showing rich features. The ripples on the right point in the direction of wavebreaking. The next step is to reduce the pump current slowly to a lower value of 300 mA (corresponding to 200 mW pump light). If the pump power is reduced quickly,

the modelock may be lost. The laser stops pulsing at the very low pump power of 160 mW. Keeping the waveplate settings where modelock initially has been found, the laser starts to pulse again when the pump power is increased to the search value. The black spectrum is retrieved at lowered pump power. It consists of a broad central peak and two slightly asymmetric side bands. Only a small sinusoidal modulation is present on the central peak, no direct sign of multipulsing is detected. The full width at half maximum (FWHM) of the black spectrum is 22 nm, comprising the main broad peak and the right sideband. No optimisation of the waveplates has been done in this case, which would eventually lead to a more symmetric spectrum, this way enhancing the FWHM spectral width to about 40 nm.

RF Spectrum

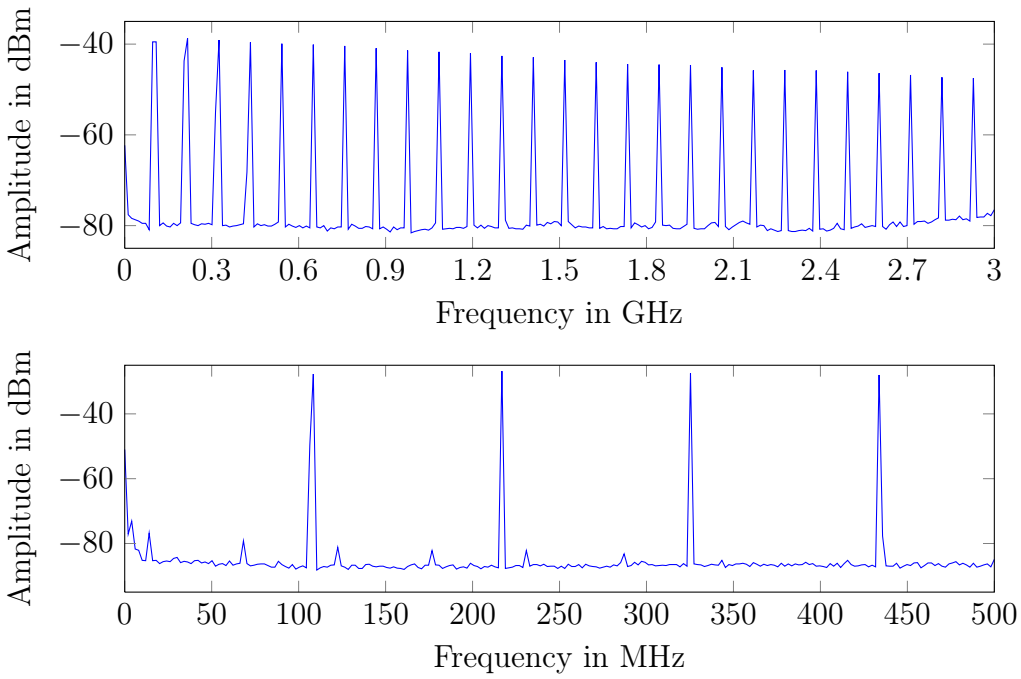

Figure 5.5: RF spectrum of the pulse train from the oscillator output. Top: whole RF analyser range, resolution 1 MHz, bottom: first 0.5 GHz, resolution 0.3 MHz.

The next standard laser diagnostic needed is a RF spectrum analyser. With it, the pulse train from a photo diode (as seen in time domain by the oscilloscope) is Fourier transformed to yield a frequency comb. A plot of a RF

spectrum measured with a 3 GHz spectrum analyser is seen in fig. 5.5. In the top row the frequency comb over the whole detection range is plotted. The equal spacing of about 110 MHz becomes clear, but details such as the exact frequency of the fundamental mode or other features such as a modulation of the peak amplitudes are not specifiable. This is partly due to the low measurement bandwidth of 1 MHz which cannot be set lower (that is, better,) at this frequency range and partly due to the limited frequency range itself. As for the synchronisation of the oscillator the 12^{th} harmonic is used, the deviation of the 1.3 GHz line from the exact value which is the FLASH accelerator driving frequency is important. In a detailed look onto the 1.3 GHz line of the laser, its frequency is measured to be 1.3002743 GHz, this means, the laser is 274.3 kHz off in the 12^{th} harmonic, giving a frequency mismatch of 22.85 kHz in the fundamental. With the RF spectrum analyser at hand the laser fundamental frequency is being tuned to the exact subharmonic of 1.3 GHz with an accuracy less than 1 kHz (limited by the screw of the little delay stage that is used for this purpose). With a laser fundamental nearly matching the right frequency, the downmixing is used to obtain the difference signal (see sec. 4.1.1) and the temperature regulation is used for the remaining small frequency difference (see sec. 5.1.5). The RF spectrum analyser can also be used to detect odd modelock states. In the bottom row a measurement with an increased resolution (300 kHz) and thus only a part of the full range is shown. For low frequencies, little extra spikes occur. Their spacing is about 68 MHz, which is not obviously connected to the fundamental repetition rate. The pump power has not been reduced to 300 mA for this measurement, it corresponds to the blue spectrum in fig. 5.4. After reducing the pump power, the little spikes are gone. It may have been some residual noise coming up now and then due to the strong pumping or an unstable multiple pulse state.

Autocorrelation

The duration of laser pulses lower than tens of picoseconds (ps) cannot be measured with direct time domain devices such as photodiodes (a duration of 1 ps corresponds to a bandwidth of 1 THz which can not be handled with electronics). Thus, indirect measurements need to be applied. The standard method for laser pulses is the autocorrelation. Here the laser pulse is split in

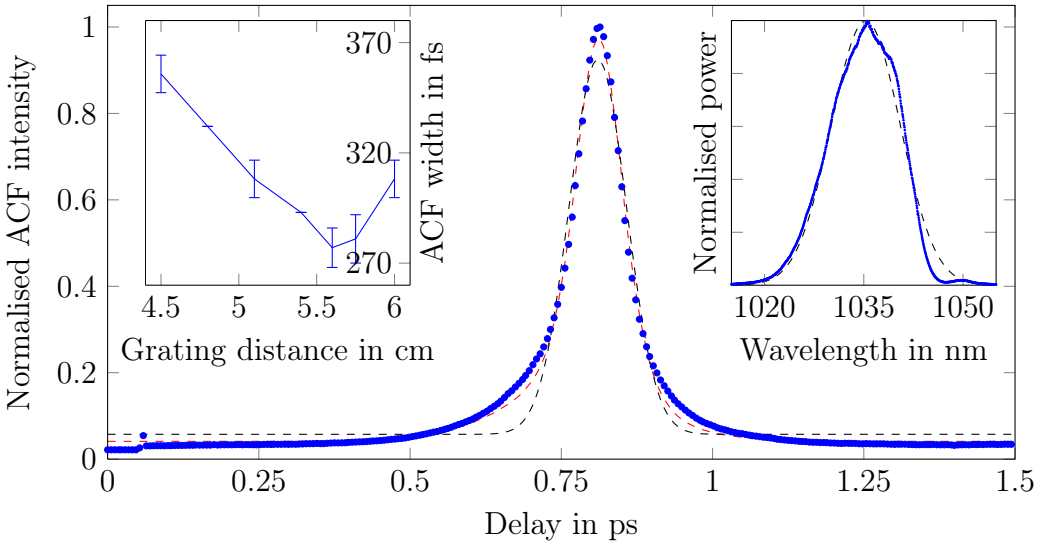

Figure 5.6: Left inset: Width of autocorrelation traces of pulses leaving the prechirper for different grating distances d. Main figure: Autocorrelation trace of the shortest laser pulses ($d = 5.6$ cm), calculated pulse widths from sech^2 fit (red): 167 fs, gaussian fit for comparison (black). Right inset: The corresponding optical spectrum, width: 13 nm (FWHM) from gaussian fit (black).

two parts, on one part a variable delay acts, and then the two pulses are recombined in an optically active crystal to produce the second harmonic (SHG). A photo detector measures the intensity of the frequency doubled light. The obtained autocorrelation function gives some information on the pulse shape and length, but only when a pulse form is known beforehand, a result with no ambiguity is received. For example, the autocorrelation function is always symmetric, even when the input pulses are not. For very short pulses the interferometric autocorrelation is deployed, even few-cycle pulses can be measured this way. The oscillator output of the laser built for this thesis can not be measured directly, as the freespace output of the oscillator is coupled into a fibre amplifier (the booster) inside the oscillator box. Thus, only the output of the booster amplifier can be measured (refer to fig. 4.5). The pulses leaving the oscillator will have a (positive) chirp which will become stronger by travelling through the booster amplifier. The pulses leaving the booster amplifier will be rather long. More information can be gained by looking at the pulses after they were compressed in the prechirper. Such a measurement is presented in

fig. 5.6. The main picture shows the autocorrelation trace as acquired by the APE systems PulseCheck autocorrelator together with a gaussian fit (black) and a fit according to a sech^2 pulse shape (red). The FWHM values of the fits for the two different pulse shape assumptions do not differ much, but calculating the actual pulse width results in $\Delta\tau = 200$ fs FWHM for the gaussian fit and $\Delta\tau = 167$ fs FWHM for the sech^2 fit. Regarding the fit quality the latter seems more appropriate, which is in agreement with the pulse shape expected for this particular modelock regime. The right inset shows the normalised optical spectrum after the booster amplifier, and the left inset shows a measurement of the ACF width in dependency of the prechirper grating distance. A clear minimum can be seen for a grating separation of 5.6 cm, at which the ACF plotted large has been measured. This measurement corresponds to the chirp considerations in fig. 2.3. Using $\Delta\nu = (c/\lambda_0^2) \cdot \Delta\lambda$ with $\lambda_0 = 1035$ nm the central wavelength the time-bandwidth product $\Delta\nu \cdot \Delta\tau = 0.608$ is calculated. The minimum value for sech^2 shaped pulses is ≈ 0.315, the laser pulses are not transform limited. This indicates higher order chirp is present in the measured laser pulses. A FROG measurement to determine the actual phase along the pulse is needed for a more detailed analysis. However, the pulses are being chirped in the following gated amplifier and leave the laser system with a duration of about 1 ps. This additional linear chirp is dominating the nonlinear chirp which enables a non-ambiguous time-to-frequency-mapping needed for electro-optic spectral decoding.

5.1.4 Noise Performance of the YDFL

Phase Noise

Two different kinds of noise are of importance in this thesis, the frequency noise leading to an arrival time jitter and the amplitude noise. To start with the former, the frequency noise of the laser pulses arises from the phase noise of the pulses inside the cavity. Phase noise and frequency noise are used synonymously in this thesis. The integrated arrival time jitter calculated from the measured phase noise spectrum must be low to allow for a precise synchronisation of the laser to the reference RF. It is necessary to measure the noise spectrum over the full bandwidth from the repetition rate of the experiment

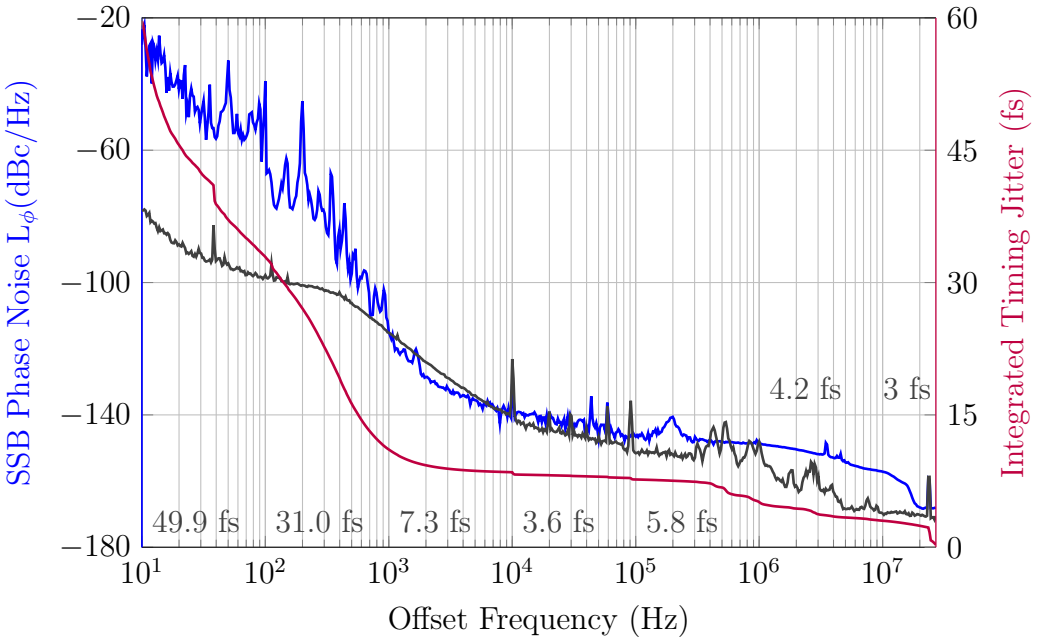

Figure 5.7: Measurement of the single sideband (SSB) phase noise of the free-running YDFL oscillator (early version with 54 MHz repetition rate) over an offset frequency range from 10 Hz to 27 MHz, the Nyquist frequency. The black curve is a measurement of the RF master oscillator reference frequency. In red the integrated timing jitter of the MO reference over the whole range is plotted, the numbers over the x-axis give the noise contributions of the MO for each decade.

(10 Hz) up to the Nyquist frequency (half the repetition rate of the laser oscillator). This is accomplished by a signal source analyser. The measurement presented here has been done using an Agilent SSA E5052B. The noise of the reference and of the measurement setup have to be regarded but turn out to be below the noise measured here. To obtain the phase noise, the laser pulse train is send to a fast photodiode (here, an ET3500F, bandwidth >12 GHz) operated in deep saturation so that it is only susceptible to changes in the arrival time of the pulses and not to possible amplitude variations. From the electric pulse train the 1.3 GHz component is retrieved by means of a band pass filter and amplified. The photodiode and the amplifier are active devices that need power supplies. All these need to be chosen with care to obtain a reasonable result. The measurement presented in fig. 5.7 shows the single-sideband (SSB) phase noise, measured with 100 correlations (this is important

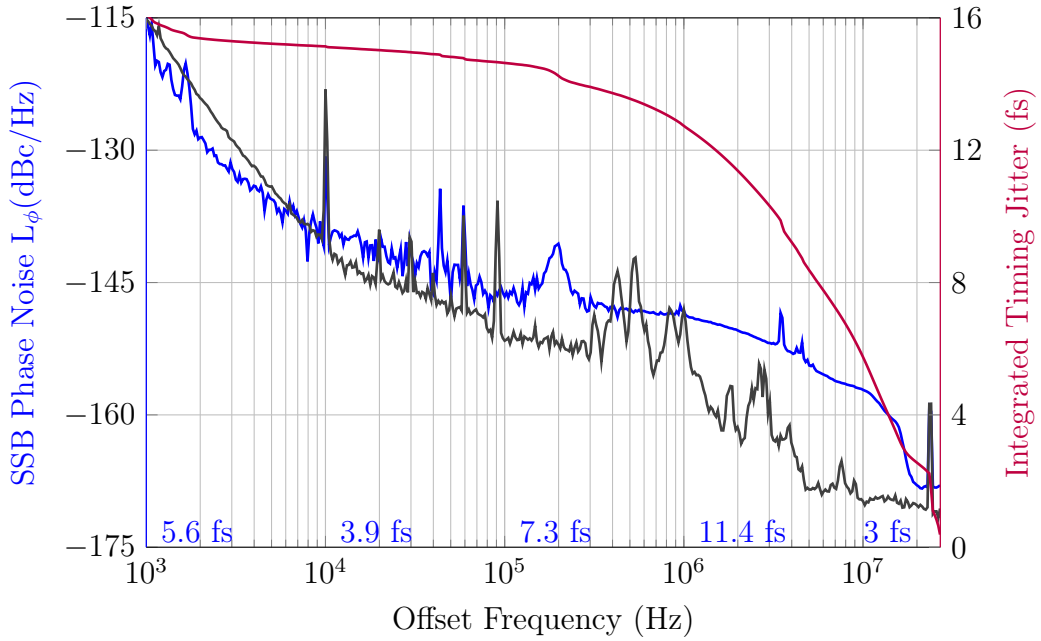

Figure 5.8: Same measurement as in 5.7, shown is the high offset frequency range of the laser phase noise (blue) starting at 1 kHz together with the integrated timing (red) and the reference phase noise (black). It sums up to 16.1 fs in the regarded frequency interval.

to supress the influence of the possibly noisy reference oscillator of the measurement with which the laser is compared). It has been done using a previous version of the laser that operated at 54.16 MHz. Three curves are plotted in figures 5.7 and 5.8: In black, the phase noise of the reference frequency as delivered to the laser laboratory is plotted. In blue, the frequency noise of the free running YDFL oscillator is plotted. In red, the integrated timing jitter is shown, on the former plot, it is the jitter of the reference frequency that sums up to 60 fs, and in the latter plot, it is the jitter of the YDFL oscillator. The latter plot is an enlargement of the former zooming in on the high offset frequency range starting at 1 kHz. In the low frequency range [10Hz,1kHz] the noise performance of the reference oscillator is better by orders of magnitude. Its jitter sums up to 60 fs (still, the largest contribution stems from the first decade), while the laser noise sums up to 18 ps for this frequency range (not shown in the plot). The situation changes when the high offset frequency range is regarded (refer to fig. 5.8): The noise performance of the laser and the

reference oscillator become comparable. Between 1 kHz and 10 kHz the laser is measured to have a lower phase noise. Starting at 150 kHz up to the cutoff at 10.5 MHz in offset frequency, the measured curve of the laser phase noise becomes flat. This indicates the measurement is limited by the setup, mainly, the available laser power on the photo diode (the main output port was used in this measurement, all power extracted from the laser cavity was lead to the photo diode). Note that the main contribution to the integrated timing jitter of the YDFL oscillator stems from this interval of [1MHz,10MHz]. The integrated timing jitter in the offset frequency range [1kHz,27MHz] is calculated to be 16.1 fs. More sophisticated measurements involving purely optical methods show that oscillators like the one presented here are capable of record-low noise figures [73]. For the noise performance of the laser oscillator when locked to the reference frequency refer to sec. 5.1.5.

Amplitude noise

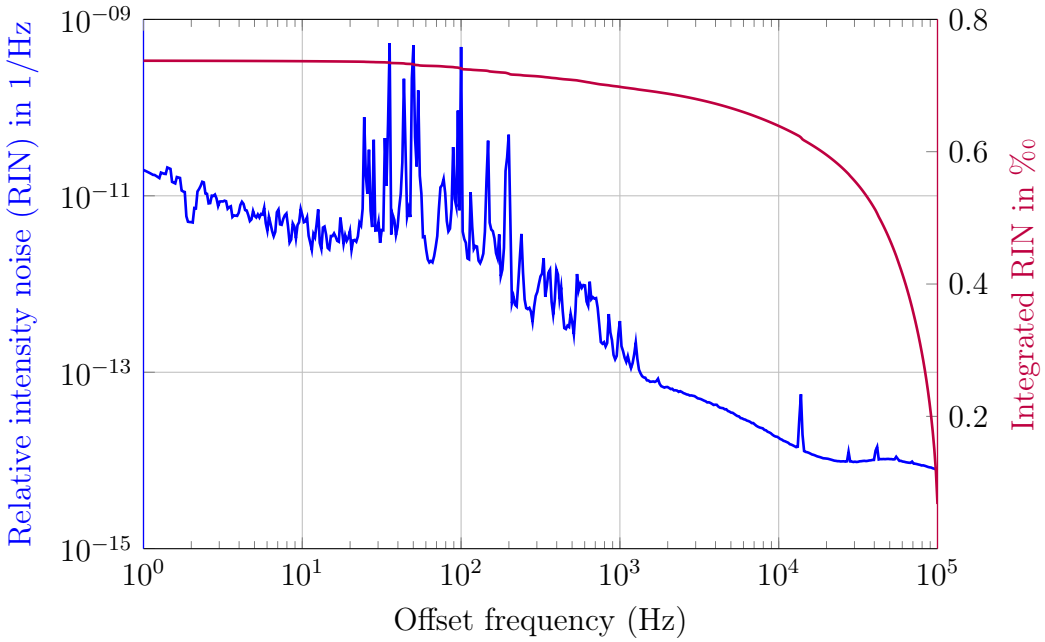

Figure 5.9: Measurement of the relative intensity noise (RIN) of the free-running oscillator (blue). The integrated RIN (red) sums up to 0.074 % in the frequency interval [1Hz,100kHz]. Details see text.

Also considered in this thesis is the amplitude noise of the laser. Several different kinds of definitions are in use for the variation of the laser output power. Here the relative intensity noise (RIN) is shown. For a measurement of the RIN, the pulse train of the oscillator output is directed onto a slow photodiode (EOT ET3040) that is operated in the linear regime (laser power 0.2 mW). In contrast to the phase noise measurement, the detector may never be driven into saturation, because then it is not longer sensitive to amplitude variations. The signal is low pass filtered to acquire the baseband and then amplified by a DC low-noise amplifier (bandwidth DC-10 MHz). The resulting voltage V_0 is recorded for calibration purposes, the amplified baseband is investigated with a baseband analyser (Agilent E5052B) whose DSB amplitude noise output spectrum is converted into a RIN spectrum. A measurement of the oscillator noise in the frequency range [1Hz,100kHz] is presented in fig. 5.9 (blue curve), together with the integrated RIN, resulting in 0.74 ‰ for the whole frequency intervall (red curve). For a comparison see [67]. The upper edge frequency of 100 kHz is chosen due to the limited bandwidth of the DC-LNA. Alike the autocorrelation trace, this measurement is taken behind the first (booster) amplifier.

5.1.5 Long Time Stability

RF Lock

The phase noise of the free-running laser oscillator for low offset frequencies is high compared to the phase noise of the RF master oscillator (see sec. 4.1.2). An active regulation locks the oscillator to the reference. The performance of the regulation can be determined with an out-of-loop phase noise measurement. Doing so, the laser is locked to the reference frequency using the synchronisation output port, and at a different output port the phase noise of the oscillator is measured. In fig. 5.10 the measured phase noise of the RF locked YDFL and the integrated timing jitter for the offset frequency range [10Hz,100kHz] is plotted. Comparing the measured phase noise in the range [10Hz,1kHz] with the measurements of the free-running YDFL (see fig. 5.7) it can be seen that the phase noise is reduced by orders of magnitude. In the interval [10Hz,100Hz] the measured laser phase noise is nearly as low as that of

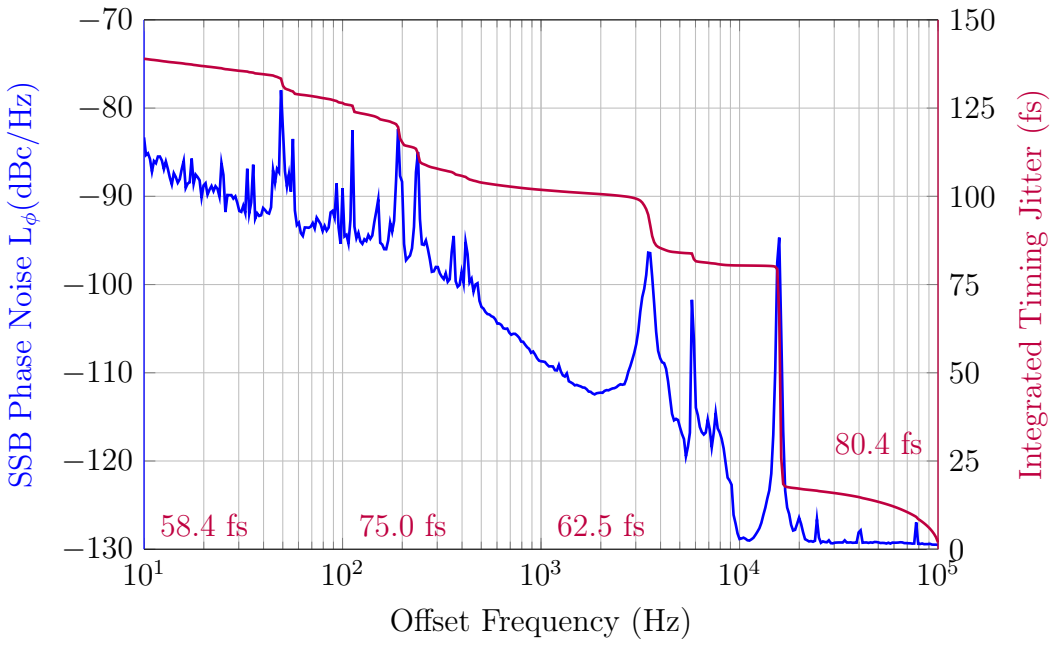

Figure 5.10: Phase noise (blue) and integrated timing jitter (red) of the oscillator locked to the reference. The integrated timing jitter in the offset frequency interval [10Hz,1kHz] has been reduced by 2 orders of magnitude, the integration over [10Hz,100kHz] shown here yields 140 fs. The numbers give the contributions of the decades.

the RF master oscillator. However, a strong spike in the noise spectrum can be seen at 10.5 kHz that also contributes strongly to the integrated timiing jitter. This peak originates from the piezo crystal used in the piezo fibre stretcher which has its first resonance frequency here. This peak disappears when the piezo driver is unplugged from the piezo stretcher. Higher offset frequencies (100 kHz to 40 MHz) are not shown in this plot as they are not affected by the regulation working on the oscillator. The timing jtter of the locked laser sums up to 140 fs in the regarded offset frequency range and 195 fs for the total range [1Hz-27MHz], and this is an overestimation as this measurement is not optimised for low phase noise at high offset frequencies.

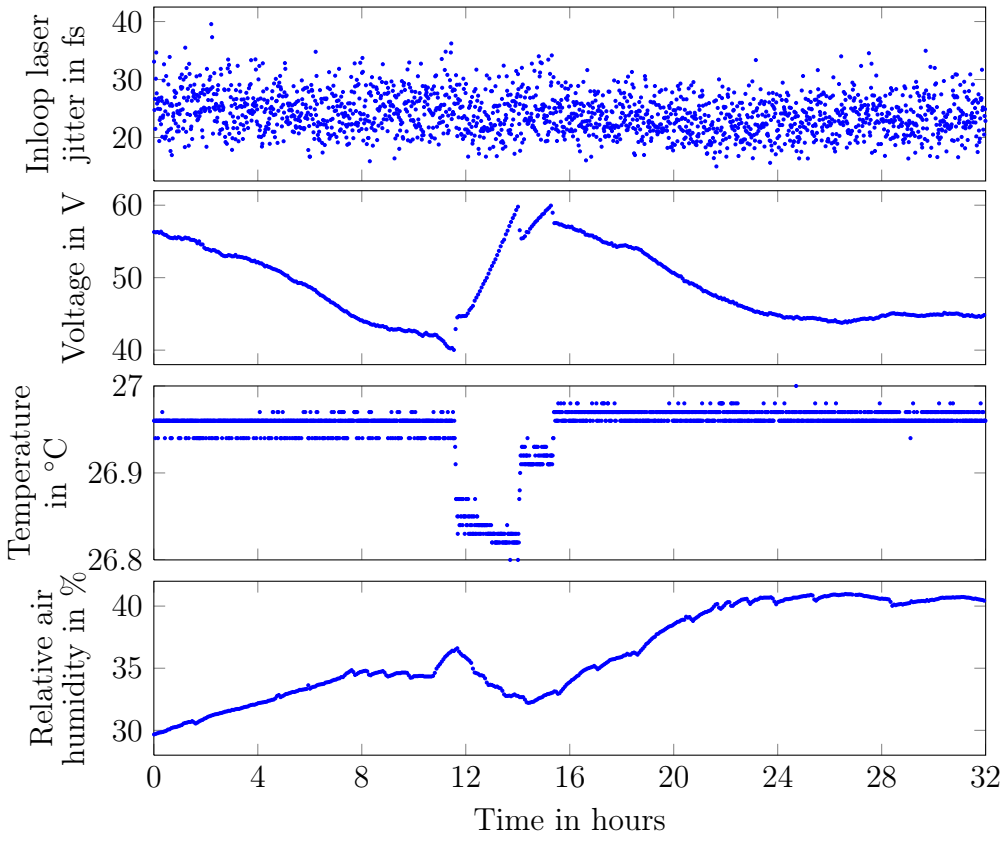

Figure 5.11: Measurement of the laser stability when locked to the RF reference with the temperature regulation active. Details see text.

Temperature Stabilisation

Having established the RF lock, it is interesting to learn about the long-time stability of the laser system. In a measurement extending 32 hours, data on the laser jitter, the voltage applied to the stretcher in the cavity, the temperature inside the laser oscillator box and the humidity in the laboratory were recorded. They are plotted in fig. 5.11. In the top row, the inloop jitter is plotted. As can be seen, the jitter remains constantly low over the whole measurement. The mean value of the inloop jitter is 24 fs with a rms deviation of 3.64 fs over more than one day. Care has to be taken in interpreting the inloop timing jitter. This number is given out by the digital regulation loop from the difference of the setpoint and the correction signal, converted with the Kϕ of the mixer. The regulation only acts on a limited frequency range up to about 1 kHz and thus this is only a part of the total jitter. To determine

the total jitter and to optimise the gain settings of the regulation the out-of-loop measurement shown in fig. 5.10 is used. A total integrated timing jitter [10Hz,54MHz] of 200 fs corresponds to an inloop timing jitter of 25 fs as shown here. The data presented here tells us that the laser has not left the RF lock over the whole time, a smooth operation is recorded. The second row shows the voltage applied to the intra cavity piezo stretcher. The temperature regulation adjusts the temperature setpoint in steps of 0.1° C when the piezo voltage leaves the range of 40 V to 60 V. This happens three times in the regarded time. It is important to notice that no changes in the laser jitter occur when the temperature is adjusted. The temperature sensor used for this measurement is not the sensor used for the temperature regulation. The main reason causing changes in the piezo voltage (that is, the optical path length in the cavity) has been identified to be the humidity in the laser laboratory. The lowest plot shows that significant changes of the relative humidity appear in the laboratory as it is not actively stabilised. The measured humidity in the laboratory ranges from 8% during a dry and cold winter period to more than 85% during wet and hot summer days. Changes of 20% may happen during a day due to weather conditions or many people working in the lab. There are two mechanisms that come into consideration causing an effect of the humidity on the laser. First, the water vapor changes the index of refraction of air on the 10^{-4} range and thus acts on the path length in the free space part of the cavity. Second, silica fibres can build in hydroxyl groups leading to stress inside the fibre and even to direct changes of the optical properties of the material during production but also when they are in humid environment [2], [57]. To adjust for larger frequency changes due to accelerator drifts or environmental changes, the total frequency detuning has been measured (see fig. 5.12). Here, the oscillator was set up for the correct repetition rate at a temperature of 28 °C. For the measurement the free-running oscillator was heated in 0.5 °C steps, and after a settle-down time the difference frequency against the reference was measured. It can be seen that a total detuning range of ± 10 kHz is accessible when the oscillator is set up at higher temperatures initially. The detuning constant is about 2.5 kHz/K. The end of the temperature range for stable modelock has not been reached in this measurement, the laser performance is not deteriorated for temperatures as high as 35 °C.

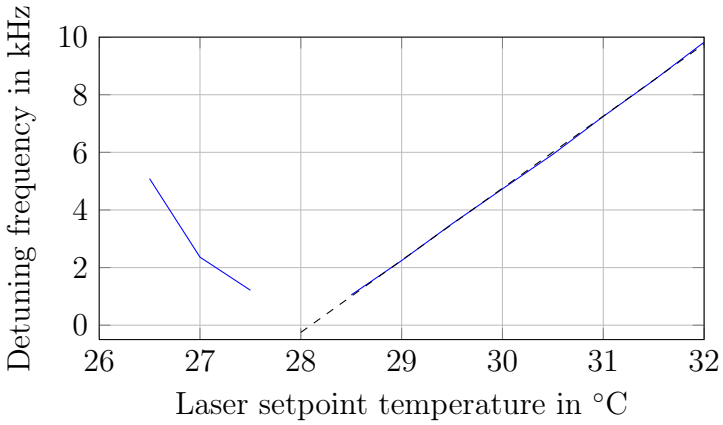

Figure 5.12: Measurement of the total frequency tuning range. The frequency changes by 2.5 kHz per Kelvin. Blue: data, dashed curve: linear fit.

5.2 Amplifier Stages

In the MOPA scheme, one or more amplifier stages enhance the pulse energy emitted by the oscillator while preserving other features such as spectral bandwidth, low jitter, repetition rate and the like. The amplifier assembled in this thesis also gates down the repetition rate in two steps to fit it to the accelerators timing scheme and furthermore to exploit the nonlinear effect of self-phase modulation (see sec. 2.1.7) to enhance the spectral bandwidth of the laser pulses. The setup has been described in sec. 4.1.3. Here some measurements are gathered that define the working point of the amplifier stages: The intermediate repetition rate at which the gated amplifier operates, the prechirper grating distance, and the pump powers of the amplifier pump diodes have to be set. To this end a measurement of the optical spectrum as emitted by the amplifier after having travelled through the EO setup has been made. It is a single-shot measurement, the repetition rate of the laser system output has been set to 10 Hz, and the line-scan camera is triggered accordingly. The pump powers of the two amplifier stages have been varied, for each setting 50 camera shots were taken. The setting $I_{Pump} = 200$ for both the booster amplifier and the gated amplifier is used as background, as no difference to $I_{Pump} = 0$ is seen. This measurement allows to define a working point that is a trade-off between the laser pulse energy (as high as possible), the bandwidth (reasonably high), and the shot-to-shot deviation of the spectra.

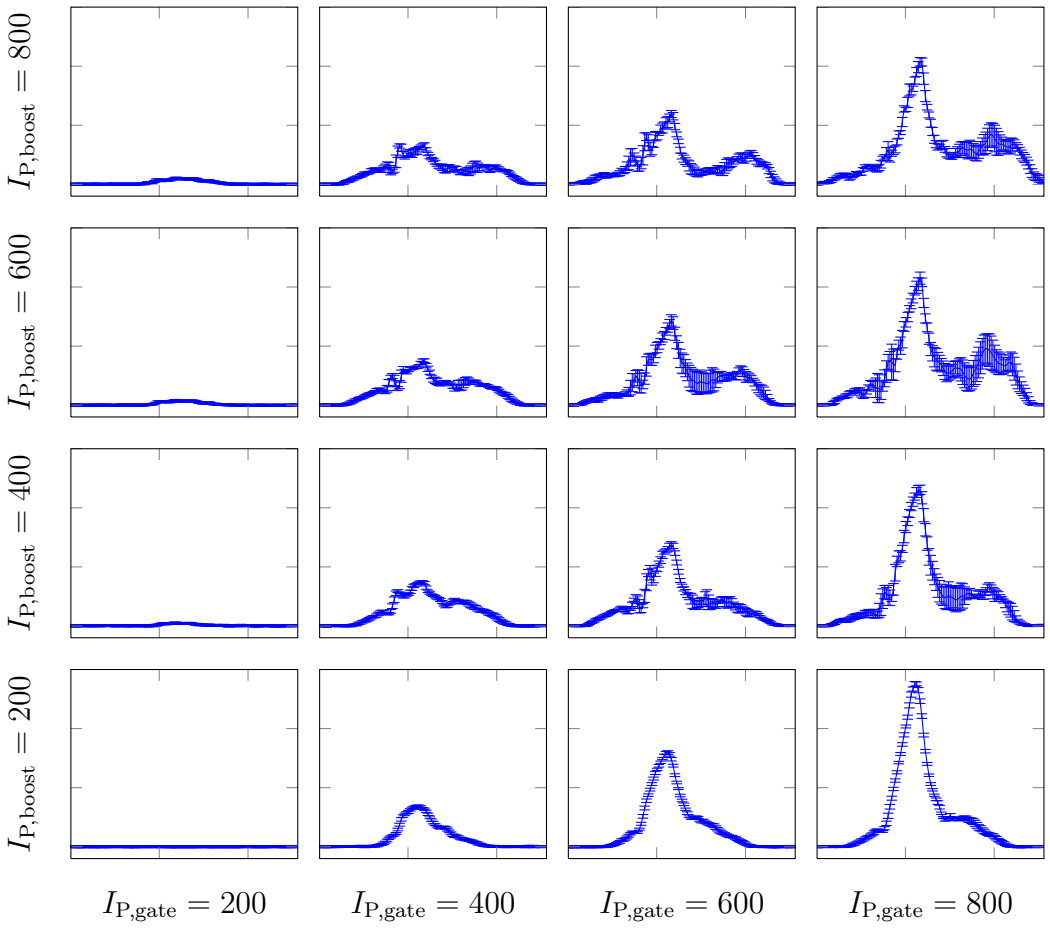

Figure 5.13: Optical spectra of single laser pulses as emitted by the gated amplifier. The pulses have travelled through the complete EO setup and are measured by the line scan camera, waveplates are set to 4° off CP. The grating distance in the prechirper is $d = 10$ cm, the intermediate gate frequency is 9 MHz. The pump currents for the laser diodes pumping the two amplifier have been varied. Each plot shows the mean of 50 shots and the according standard deviation. All spectra have been camera background substracted. All plots have the same x- and y scaling, they show the counts over the camera channels. The detector covers an optical bandwidth of 115 nm.

An overview with some of the data from that measurement is given in fig. 5.13. As can be seen, the lower left spectrum is used for background correction. Following the leftmost column from bottom to top, the booster amplifier pump current is enhanced. This has only a very small effect as the gated amplifier is pumped only very weakly, leaving it more or less untransparant for light of 1030 nm. The reverse situation is following the lowest row from left to right. Here, the pump power in of the gated amplififer is enhanced, while only very sparse seed signal is given to it for amplification. This leads to a rather smooth, medium narrow peak similar to the spectrum of amplified spontaneous emission. Looking at the third row from the bottom, the situation has changed. The seed signal for amplification fed to the gated amplifier is strong enough to be detected even with very weak pumping of the gated amplififer (leftmost picture). If the pump current of the gated amplifier is enhanced, a very broad spectrum emerges (second picture from the left). It has wings that spread over the whole spectral range covered by the detector. The shot-to-shot deviation is still rather small. With a stronger pump current in the gated amplififer, the central peak becomes more noticeable again. Furthermore the shot-to-shot deviation can become very large for this highly nonlinear regime encountered for very high pump currents (two plots on the right, very same row).

5.2.1 Shot-to-Shot Fluctuations

As an example for the evaluation of these spectra, an enlargement of the plot given for $(I_{P,boost}, I_{P,gate}) = (600, 400)$ mA in fig. 5.13 is given in fig. 5.14. The main things to consider are the bandwidth of the optical spectrum and the shot-to-shot fluctuation. The latter may be regarded first. The noise of the background (that is, the mean of the standard deviation of the consecutive shots for each camera channel) is about 7 counts rms. This noise is reproduced by the two outermost parts of the regarded spectrum in fig. 5.14 (camera channel 1 to 50 an 462 to 512) and reflects the camera readout noise. This is a shot-to-shot and channel-to-channel variation which can be handled by averaging many shots. Over the whole signal (camera channel 51 to 461) the noise is calculated to be about twice as high, 15 counts rms. Thus, a shot-to-shot variation is measured that exceeds the camera background, but

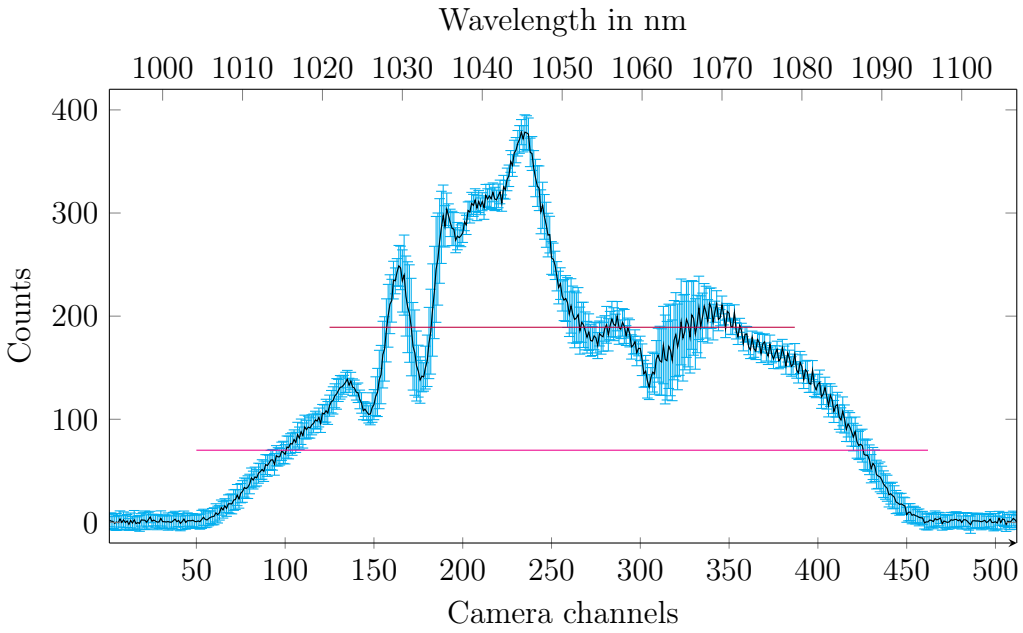

Figure 5.14: Optical spectrum acquired for the amplifier pump current setting $(I_{P,\,boost}, I_{P,\,gate}) = (600, 400)$ mA. The errorbars are the standard deviation for each camera channel for 50 subsequent shots. The purple line indicates the half maximum and the pink line is a possible threshold for the definition of the usable spectral width (see text).

it is mainly the part to the right of the main peak that exhibits fluctuations: the noise of the camera channels 300 to 350 yields to be around 25 counts rms, corresponding to a more than 10% error when the signal is about 200 counts. This region becomes wider as the pump power of the gated amplifier is increased and the noise measured here becomes larger (refer to fig. 5.13 where this can clearly be seen for high pump currents). These fluctuations are of different quality than the camera noise as the large deviation comes from shot-to-shot shape changes of the spectrum. It likely is directly connected to the strength of the nonlinearity in the gated amplifier. In the supercontinuum (SC) generation process, even very small fluctuations of the input power may have a strong impact on the resulting amplifier pulse spectrum, especially when the edge of the purely SPM governed SC generation regime is reached and other effects such as stimulated Raman scattering (SRS) and Four-Wave Mixing (FWM) come into play. This particular spectrum shows a pump current setting where the noise is tolerable for spectral decoding measurements.

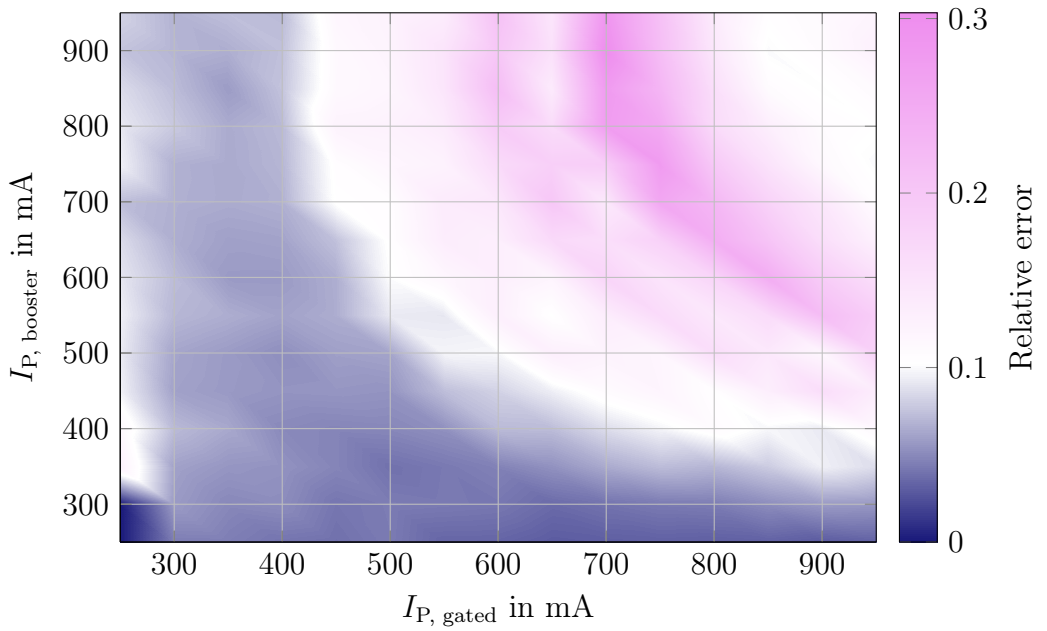

Figure 5.15: Averaged relative error of successive spectra of the amplifier measured for different pump current settings for each amplifier stage. For a definition of the plotted quantity see text.

The complete measurement consisted of 14 pump current settings for each amplifier. The relative error as calculated from the rms noise in relation to the mean counts of the signal over the usable bandwidth for each setting is plotted in fig. 5.15. It can be seen that one is restricted to values below 400 mA for the gated amplifier if the tolerated averaged shot-to-shot deviation should be smaller than 10%. The pump current of the booster amplifier can be chosen rather freely. The arc-shape maximum for pump powers lower than the maximum settings may be due to the pronounced peak developping for very high pump currents which has a rather stable shape, resulting in a dropping relative error. For the electro-optic spectral decoding setup, a 10% deviation in the spectrum amplitude corresponds to a phase advance of 0.013 for a $\lambda/2$ waveplate angle of 4° and 0.031 for a $\lambda/2$ waveplate angle of 9° according to eq. 6.1, which sets an upper limit for the spectrum instability.

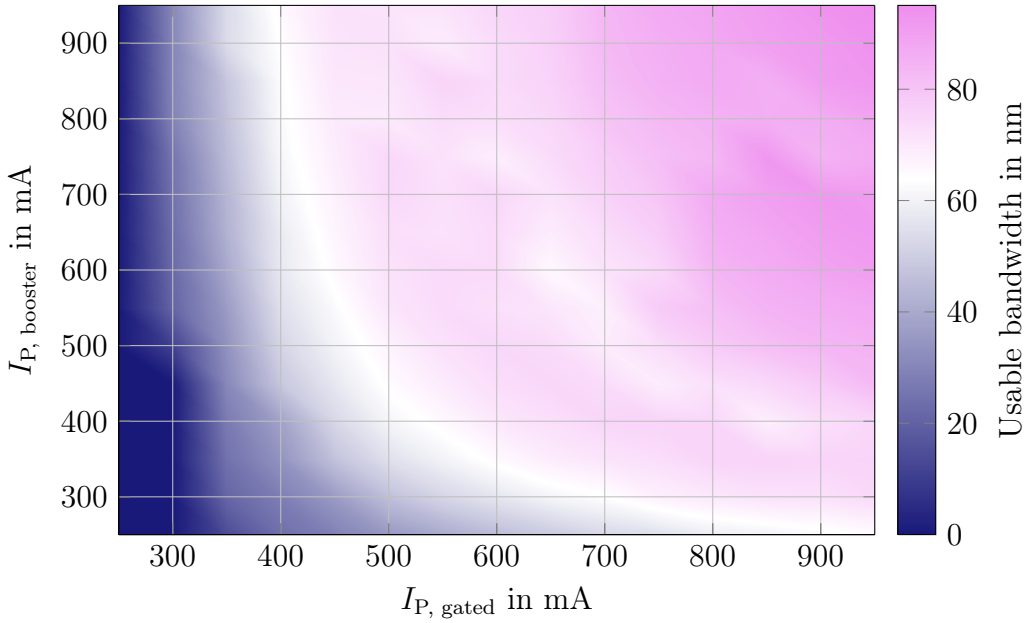

Figure 5.16: Usable bandwidth for different pump current settings for each amplifier stage. For the definition of usable bandwidth see text. The lowest four points of measurements (for $I_{P,gated} = 200$ mA) have been set to zero as no signal reached the threshold.

5.2.2 Spectral Bandwidth

The other property that needs to be regarded is the width of the optical spectrum. Standard width measures are the rms width that can easiest be given for gaussian (approximated) pulses. For many different pulse shapes the full width at half maximum (FWHM) is an appropriate choice. However, the spectra of the pulses emitted by this laser system show many features making a FWHM width definition difficult. The horizontal purple line in fig. 5.14 is drawn at the half height of the maximum. In a narrow sense of the FWHM definition, the first crossing of the edges with this line seen from the centre give the FWHM width of the spectrum, leading to 85 channel width. Changing the pump current settings by a small amount leads to a very different width, when the minima of the first sidebands just overcome the threshold. Using the outermost crossings of the spectrum with the purple line, a width of 197 channels is calculated. This wider definition certainly results in a more appropriate parameter to describe the actual spectral bandwidth. If FWHM bandwidths are specified in the following, this wider definition is used. For the spectral de-

coding technique, it is not the FWHM width that is of interest, but the usable bandwidth. This even more relaxed definition avoids the difficulty arising in the multiple minima and maxima by just looking at the width of the base of the spectrum. For the readout of the modulated spectra in the EO experiment it is only important to be above the setup noise level. In fig. 5.14 the pink line is drawn at 70 counts (the camera readout noise is 7 counts rms). This is very different from the usual definition of bandwidth as it does not refer to spectral properties ('maximum') but to properties given by the setup ('camera noise') and must be used with care. Whenever the term 'usable bandwidth' occurs it refers to this threshold condition. Here, a usable bandwidth of 325 camera channels is calculated, which corresponds to about 72 nm optical bandwidth.

The measurend usable bandwidth for all applied different pump current settings is plotted in fig. 5.16. It is clear that the exact shape of this plot is highly depending on the choice of the threshold which is here 100 counts. This value is low enough to keep the shape of the spectrum from entering into this plot which changes as the SPM induced chirp increases. It can be seen that a broad base of the spectrum is achieved even if pumping is not too strong. Having in mind that due to the tolerable noise the gated amplifier pump current will be around 400 mA, it is interesting to mention that the usable bandwidth significantly grows towards stronger booster pump currents.

5.2.3 Spectrum Features

Another two remarks can be made on the spectrum in fig. 5.14. First, the center peak between the channels 190 and 240 resembles the shape of the black spectrum seen in fig. 5.4. It is the amplified input spectrum that occurs here. It is not possible to estimate a camera channel to nm conversion based upon the input pulse spectral width as the pulse has undergone strong amplification and the spectral width will be severely degraded by gain narrowing. In fact, a rough calibration shows this feature is has a width of about 13 nm in contrast to the 30 nm input separation of the two outer peaks. Second, multiple side peaks can be distinguished. As is typical for SPM broadened spectra, the modulation is symmetric in the number of peaks (here: one) but the pronounciation of the side peaks differs. Towards the long wavelengths the spectrum features become wider than towards the small wavelengths.

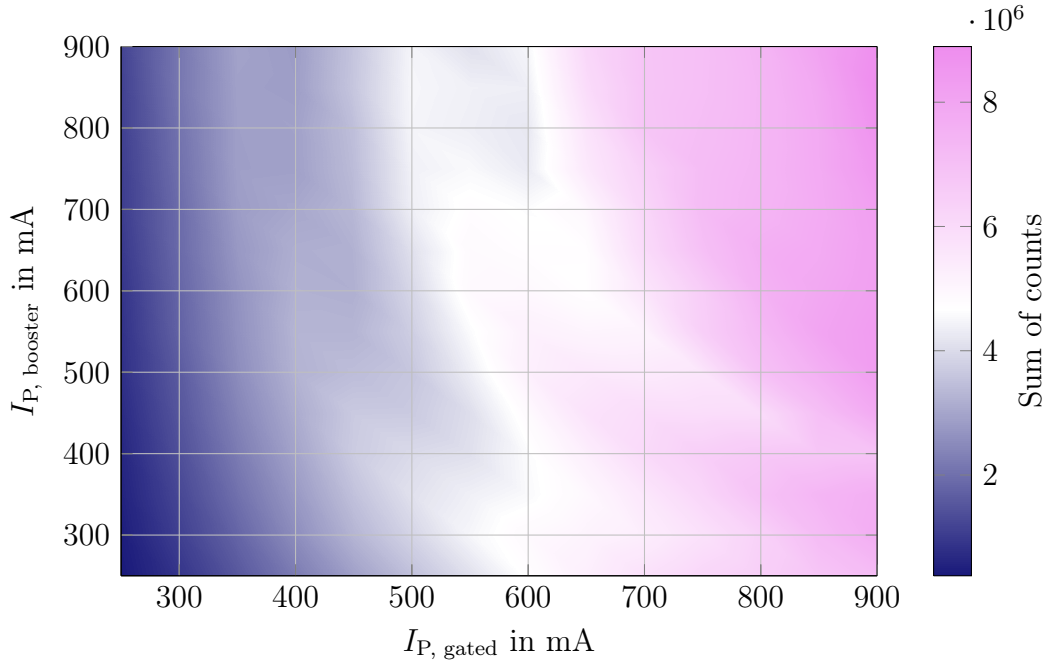

Figure 5.17: Sum of all counts over the whole detector range for different amplifier pump currents. The arc like shape is of unclear origin. For possible explanations see text.

One last plot from the pump current variation measurement can be found in fig. 5.17. It shows the sum of all counts over the different settings, that is, the camera acts like a photodiode and measures the total incoming light power. Interestingly, a wavy shape is acquired, that becomes more pronounced when the booster amplifier pump current is high. In this case the gated amplifier has to cope with higher input powers. This seems to lead to a large deviation from the exspected linear behaviour. Also, the arc shaped dip occurs at the very same pump settings as the peak of the shot-to-shot variations plot 5.15. If the pump current of the gated amplifier is restricted to about 400 mA, only a medium power can be extracted from the laser system, which can be tolerated as long as the pulse energy is sufficient for the electro-optic experiment ($\approx$ 5 nJ).

5.2.4 Amplifier Operation Settings

In conclusion, the trade-off between the pulse energy, the shot-to-shot variation and the spectral bandwidth has been found to be at $(I_{P,booster}, I_{P,gated}) = (600, 400)$ mA. A hard boundary is set by the shot-to-shot fluctuations that become very strong for high pump powers. As exspected, the pump current for the gated amplifier in which the nonlinearity is exploited for enhancement of the spectrum has the largest influence on the shot-to-shot variations as well as on the spectral broadening. However the found current set point offers a high enough usable bandwidth, the spectrum nearly completely fills the detector range. As this measurement has been conducted in the exact setup for electro-optic spectral decoding, all losses are already included, and the pulse energy is found to be sufficient.

This measurement has to be reiterated for different settings of the prechirper grating separation for a variation of the (negative) chirp of the input pulse of the gated amplifier. Here, the grating distance has been set to a large value (10 cm) as a smaller separation lead to a severe distortion of the optical spectrum even for small pump powers. A similar effect has been observed for lower intermediate frequencies of the gated amplifier. In this measurement, it has been set to 9 MHz which is the maximum gating frequency that can be achieved with this setup. By changing to lower frequencies (4.5 MHz, 3 MHz, 1 MHz and 500 kHz have been tested), the achieved optical spectra where fluctuating strongly. An explanation is that by going to very low intermediate gate frequencies a regime is encountered where the whole energy stored in the active fibre of the gated amplifier is delivered to less and less pulses. The dramatically increasing pulse energy while crossing over to that regime results in nonlinearities that can neither be controlled nor exploited with this setup.

Chapter 6

EO Measurements

6.1 EO at 140 m

The first step in conducting electro-optical experiments is to set up the temporal overlap of the laser pulse and the electron bunch. Therefore a fine timing scan of the laser with respect to the electron bunch needs to be conducted after the rough overlap has been set. Different readout setups for the timing scan where tested, however the temporal overlap has not been established at the EO setup at 140 m (EO@140m) where the self-build laser is located. In an attempt to solve this the initially built in 0.2 thin GaP crystal (measured thickness: 175 µm) was exchanged in the FLASH shutdown in autumn 2011 with a 0.5 mm thick GaP crystal. Two arguments lead to the decision - first, the old crystal might have been corrupted in earlier experiments, second, the well adapted wavelength of the YDFL laser allows for thicker crystals which in turn offers a better signal-to-noise ratio. An image of the old EO crystal pair in its holder can be seen in fig. 6.1, on the left side a 0.2 mm thick ZnTe crystal that has not been used in this thesis, on the right a 0.2 mm thick GaP crystal. In the beam pipe the holder is installed turned by 90° to the right and flipped. The magnified inset of the usual measurement location has a width of 0.4 mm. At this location four large dark spots can be seen (even with the bare eye), of these three are shown, and multiple smaller dark spots; the darkening does not only affect the crystal surfaces. These may originate from earlier measurements with high-power laser pulses (≈0.1 mJ) used for EOTD. The exposure to high-power laser pulses might have affected the crystal structure

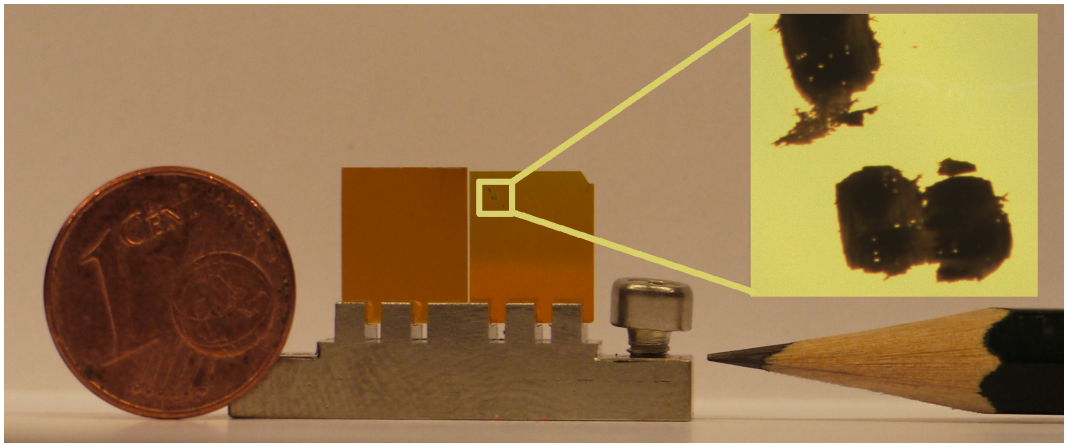

Figure 6.1: Photograph of EO crystals exchanged from the tunnel setup. To the right is the 0.2 mm thick GaP crystal used for EO experiment attempts. The magnification of the usual measurement spot has a width of about 0.4 mm.

severely, so that no induced polarisation change can be proved in the vicinity of these spots, making EO experiments impossible.

With the crystal exchanged, new scans were made to find the temporal overlap. A typical laser pulse duration for this task is 1.5 ps with a pulse energy of 5 nJ. The laser system repetition rate is set to 10 Hz. The critical trigger stability of the first gating stage (picking of a 9 MHz pulse train from the 108 MHz oscillator pulse train) has been stabilised using a new trigger generator with a 10%/90% rise time of 1.5 ns and a DESY built trigger stabilisation card that reduces the trigger jitter from 1 ns to 0.2 ns. The uncertainty of the rough timing setpoint as determinded with the pick-up antenna (see sec. 4.2) is about $\pm$ 1 ns, and the electron bunch length is typically 100 fs (rms). This restricts the stepwidth of a fine timing scan to not more than 1 ps. Using typically 100 averages for every time step, a 2 ns long scan takes about 8 hours at a data aquisition rate of 10 Hz. While a scan is conducted, several control variables are monitored to assure the laser stability and the accelerator performance, of which some are plotted in fig. 6.2. The most meaningful for the laser is the inloop timing jitter (see sec. 5.1.5). It can be seen that it stays below 60 fs for the complete duration of the scan. The center row shows the signal of the slow phase detector which is slowly changing as for the timing scan the 1.3 GHz reference is shifted against the 108 MHz reference of the slow phase detector.

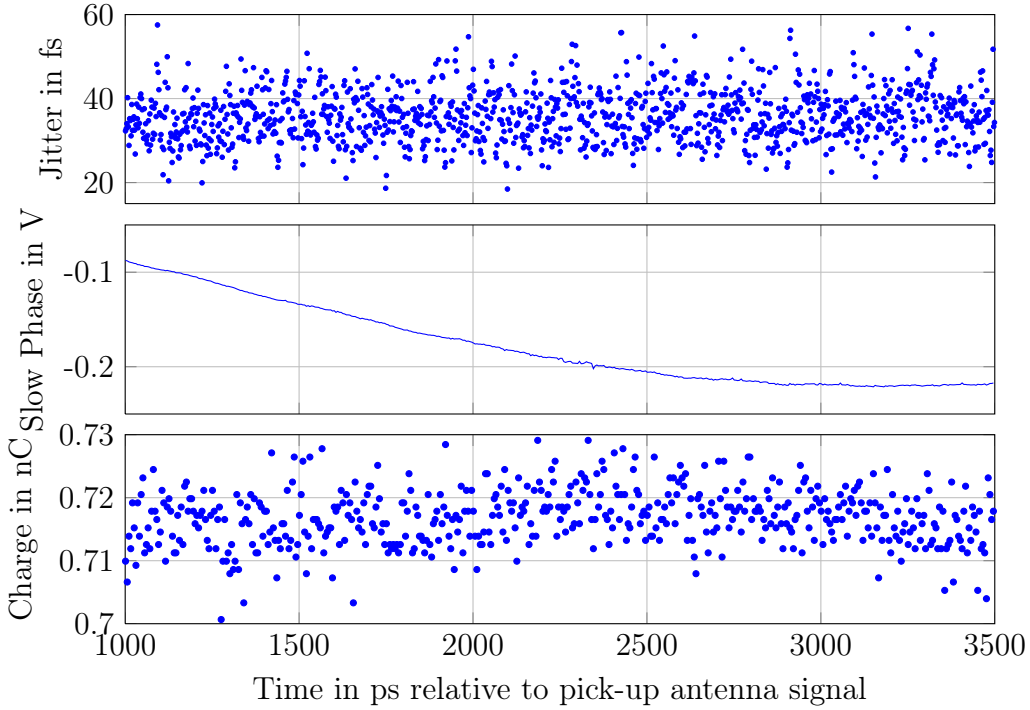

Figure 6.2: Inloop timing jitter (top row), slow phase detector signal (centre row), and electron bunch charge (bottom row) during a fine timing scan. The time $t = 0$ ps is defined by the overlap of the signals of the laser pulse and the electron bunch as transmitted by the pickup antenna cable.

In the bottom row the charge of the accelerator as read out by a toroid near the EO setup is plotted. It remains near the set value of 0.7 nC for the time of the scan.

The data evaluation for the fine timing scan using the line array camera equals the evaluation for the actual EO measurement. First, a background spectrum I_{Bg} without light on the detector is taken (the camera background). All further spectra taken are camera background substracted before further evaluation. Next, an averaged reference spectrum $I_{Ref} = I_{det}(\Gamma = 0)$ of the unmodulated laser pulse is acquired from which the laser intensity I_{Las} for each channel can be calculated. Then, one hundred spectra of possibly modulated laser pulses are taken for each time step. The spectra are averaged, and only the mean spectrum $I_{det,mod}$ and the rms variation of the spectra is saved. As only the intensity at the detector is accessible to measurements the reference spectrum has to be taken for every setting of the angle θ of the $\lambda/2$

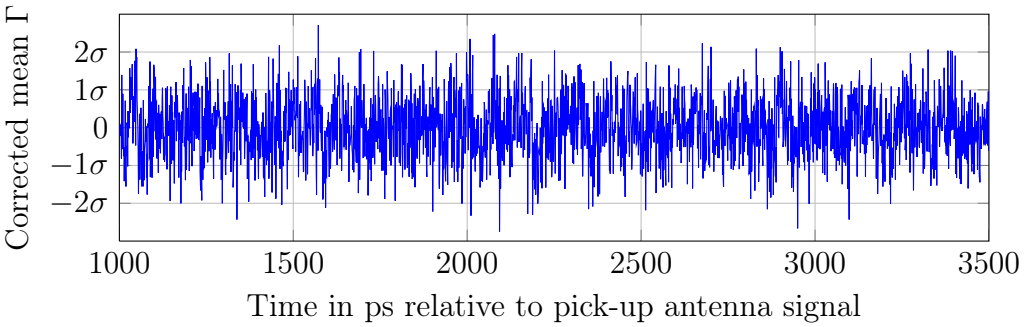

Figure 6.3: Fine timing scan to establish the temporal overlap of laser pulse and electron bunch. The stepwidth of the laser is 1 ps. A drift correction for the plotted data is applied. The standard deviation is $\sigma = 9.5 \cdot 10^{-4}$.

retarder waveplate. Rearranging (eq. 2.91b) and omitting the background term $s_{bg} I_{Laser}$, the phase advance Γ is given by a channel-wise calculation of

$$\Gamma(\theta, \psi = 0) = \cos^{-1}\left(1 - \frac{I_{det,mod}}{I_{det}} \cdot (1 - \cos(-4\theta))\right) - 4\theta. \tag{6.1}$$

The optimal $\lambda/2$ waveplate angle θ has to be determined experimentally after the overlap has been found, the sign of the phase advance and the signal-to-noise ratio depend on it. As an initial guess $\theta = 4°$ has been chosen as for this angle the intensity of the unmodulated laser spectrum varies strongly for small variations around θ. Only a central region of interest of about 45 nm width is regarded for the scan as at the spectrum edges the influence of fluctuations grows. The phase advance is calculated for every time step, averaged and plotted in fig. 6.3, where it already has been corrected for a slow drift that is visible in this data set. The y ticks indicate multiples of the rms deviation of the data with $\sigma = 9.5 \cdot 10^{-4}$ which originates from the averaged shot-to-shot laser noise (see fig. 5.15). Analysing the spectra corresponding to the few peaks exceeding the 2σ - proximity did not give hard proof of EO modulated laser pulses. A general problem is that the contrast of the modulated spectra over the unmodulated spectra is exspected to be very small. This is mainly due to the mismatch of the laser pulse length and the electron bunch length. Using longer laser pulses allows for less time steps and thus more averages at every step. On the other hand, the fraction of the laser spectrum that becomes modulated decreases as the chirp increases. With an

electron bunch duration of $1/10^{\text{th}}$ the laser pulse duration, the effect in the spectrum is restricted to a corresponding spectral width, and the total effect (by taking the mean modulation of each spectrum) lowers by a factor of ten. Furthermore, it is possible to have a positive and negative modulation when the near-crossed polariser setting is used, depending on the waveplate setting. The optimal waveplate settings can only be established once the EO signal has been found. Further scans with smaller stepwidth and shorter laser pulse duration at different settings for the angle θ of the $\lambda/2$ waveplate need to be conducted. This is a time-consuming matter as appropriate accelerator settings are needed for long times (charge > 0.5 nC, strong compression) and can be ideally done during user runs. However, with the now built-in thick GaP crystal there is a chance of finding the temporal overlap in order to conduct the long-planned electron bunch diagnostic experiments.

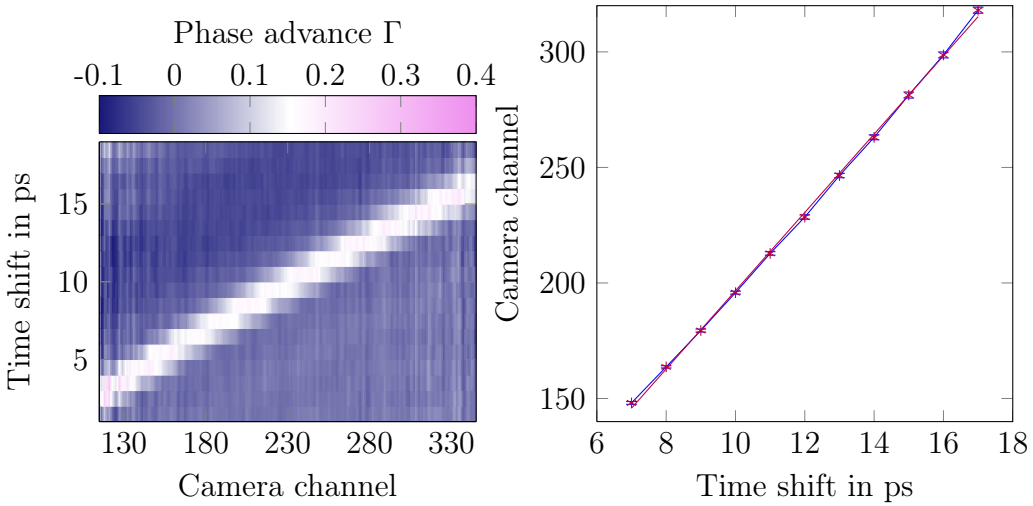

Figure 6.4: Time calibration of the upgraded EO monitor. A series of spectra was acquired with a temporal shift of 1 ps between successive shots. Left: Phase advance (in a.u.). Right: Horizontal position of maximum phase advance over time shift.

6.2 EO at BC2

Bunch shape meaurements using the electro-optic bunch shape monitor downstream BC2 were conducted to characterise the impact of the changes that were done after its initial comissioning (see sec. 4.3.3). These are exchanging the 0.5 mm thick GaP crystal with a 5 mm thick one and adding more chirp to the laser pulses by an additional piece of optical fibre. For details on the timing search and the data evaluation refer to [12], the procedure is similar as in sec. 6.1. Three anticipated effects of the upgrade are addressed by the measurements presented in this section. First, the temporal window for electron bunch analysis needs to be newly determined. Second, a higher phase advance than with the thinner crystal likely occurs. And third, the possibly negative effects of both changes on the temporal resolution need to be determined. The issues will be taken care of in this order.

6.2.1 Time Calibration

As the chirp of the laser pulse was changed while its spectral bandwidth remained unchanged, the mapping of the time information to the camera chan-

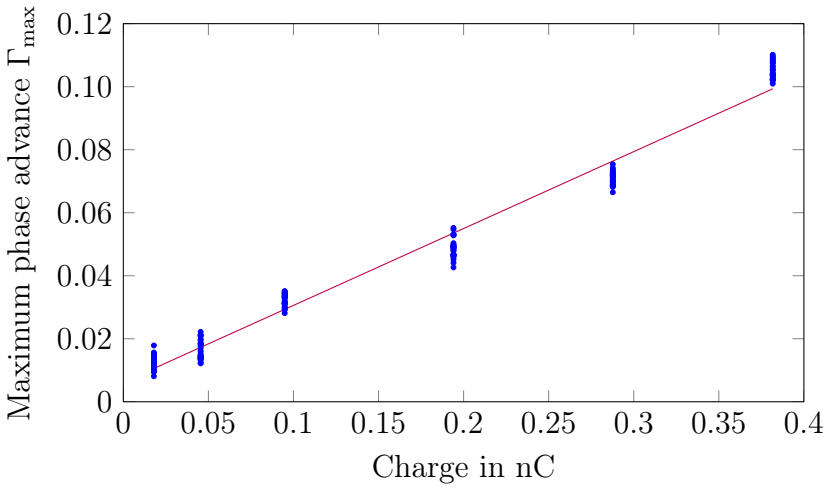

Figure 6.5: Maximum phase advance of 30 successive shots for 6 different charges, each. Purple: linear fit. The charge uncertainty is 0.04 nC.

nels changed and needed to be remeasured. A series of spectra was taken with the laser pulse shifted with respect to the electron bunch by 1 ps between the shots. The result is shown in fig. 6.4 on the left side. 18 successive spectra, shifted by one step, are plotted above the camera channels. The light region indicates the modulated part of the spectrum. For each time step, a gaussian was fit for the measured phase advance was made, whose maximum position is plotted over the camera channel (right). A calibration constant of 16.94 ±0.34 channels/ps or about 60 fs/channel is retrieved, changed from 28 channels/ps before the chirp was changed. The usable temporal range of the monitor was enhanced from 6.4 ps to 10.6 ps assuming the same usable bandwidth of the spectrum (for an approach to 'usable bandwidth' see 5.2.2).

6.2.2 Low Charge Ability

A series of measurements was conducted where the charge of the electron bunch was lowered to test the low charge capabilites of the upgraded monitor (fig. 6.5). For six different electron bunch charges spectra were taken. The maximum of a gaussian fit to the phase advance is plotted over the readback charge value from a toroid situated nearby the EO monitor for 30 spectra for each charge. A linear fit plotted to the data crosses the origin whithin the measurement accuracy. Note that the charge values have a considereable uncertainty

as the toroid resolution is essentially reached for the lowest charge. The absolute value of the phase advance is in gross agreement with the measurement conducted with the thinner EO crystal shown in [12] and thus in disagreement with the exspectation of an improved signal strength. This may be due to a different accelerator setting - the compression is not specified in the formerly taken data set - or due to a different data evaluation (for example, taking the maximum of the data set instead of the maximum of fitted curves which equals a smoothing). Another possible source may be systematic error, for example might the effect of the velocity mismatch of the THz field and the laser pulse enveloppe counteract the thicker crystal to a certain amount. Whatsoever the monitor can be used for bunch length analysis for low charges as long as the compression is high because the maximum spectral modulation is depending on the maximum current and not on the integrated bunch charge. To improve the signal-to-noise ratio it is then recommended to use many averages (100 or more). It needs to be stated that finding the EO signal using a fine timing scan was not possible at a bunch charge of 0.15 nC at high compression.

6.2.3 Electron Bunch Profile Measurements

In fig. 6.6 a measurement of electron bunches of differing length is shown. The bottom picture shows a measurement with a phase of 13.6° of ACC39 which corresponds to tits on-crest phase. In this setting the energy chirp of the elelctron bunch acquired in ACC1 (which is operated off crest) is not altered. This setting results in long electron bunches. The ACC39 phase has been stepwise decreased to linearise the phase space and thus producing shorter electron bunches after compression in the bunch compressor. The charge for all these measurements was 0.58 nC, and thirty averages were applied, except the uppermost one, where no averages are applied and the charge was 0.38 nC. The error shown is the deviation of fit widths for successive bunches.

One goal in increasing the chirp of the laser pulses was to allow for the measurement of on-crest electron bunches. As result of the time-camera mapping calibration (sec 6.2.1) it was found that the usable time window for measurements is now about 10 ps. This could be verified (fig. 6.6, bottom row). The available spectral range for measurements is just large enough to allow for a gaussian fit to determine the bunch length in this case. However, the signal

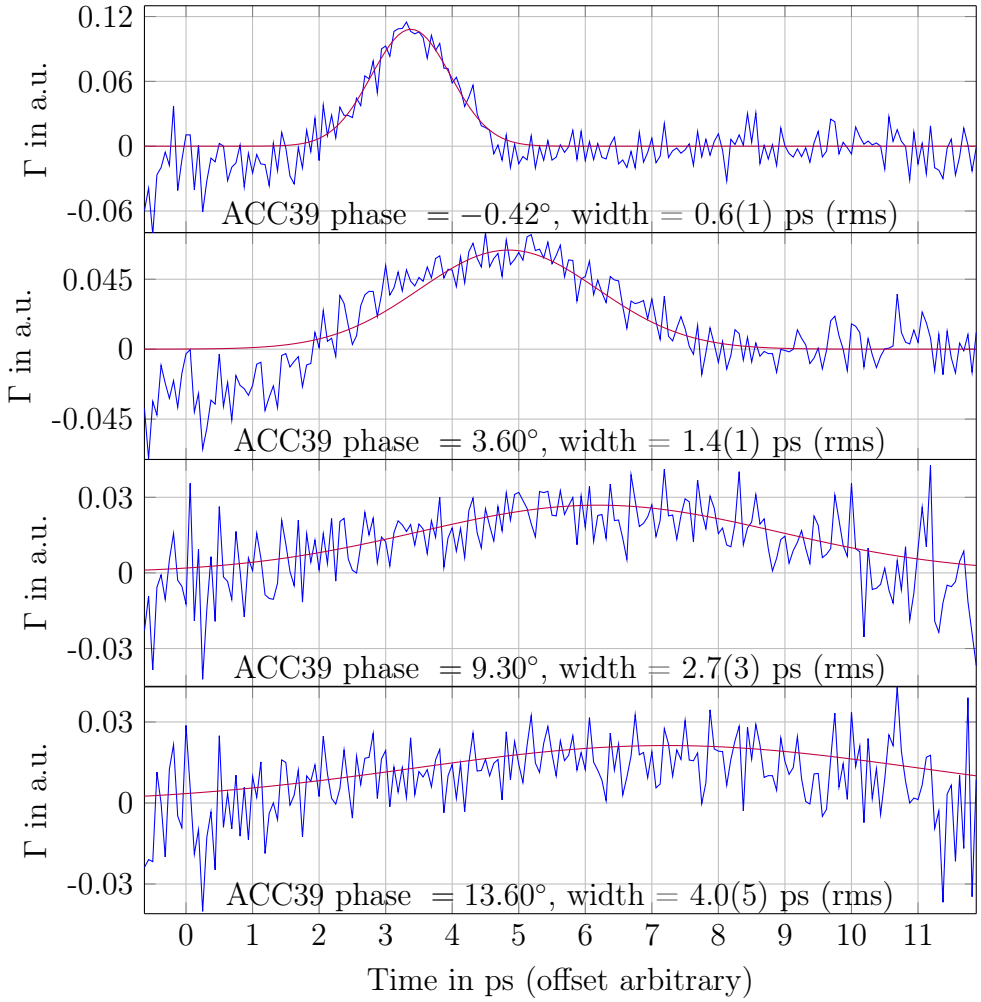

Figure 6.6: Measurement of electron bunches of different length using the EO monitor, 30 averages (blue), gaussian fit (red), ACC39 phase and rms width as derived from fit.

does not drop to zero on the sides of the usable range due to the applied normalisation. A single shot measurement might be only possible with higher bunch charges. Also it needs to be stated that the electron bunches can become even longer if BC2 is switched off or ACC1 is operated on-crest. Then the electron bunches arrive at the electro-optic monitor with a rms width of 6 ps as they are delivered by the electron gun, and accordingly the current lowers, further decreasing the signal-to noise ratio. For these exotic accelerator settings measurements can only be conducted with a high amount of averages. In normal operation with applied phase space linearisation shorter bunches

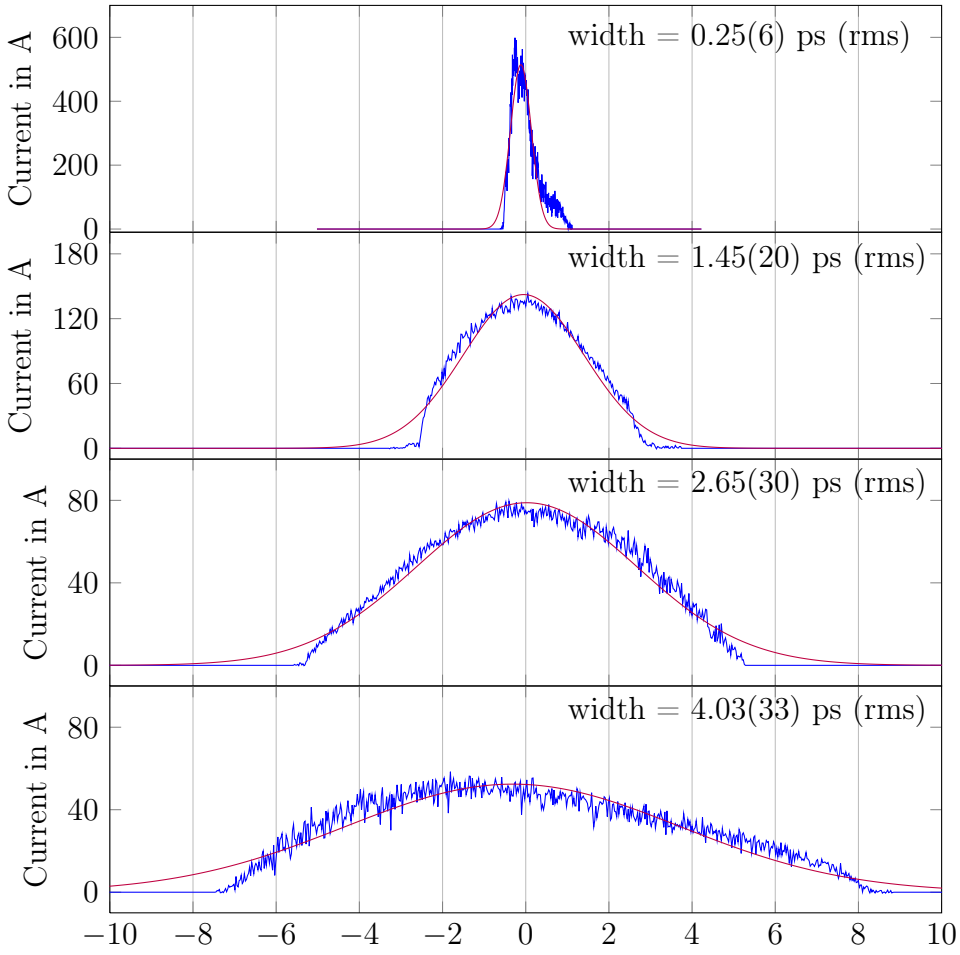

Figure 6.7: Measurement of electron bunches of different length using the transverse deflecting structure (LOLA) (blue), gaussian fit (red), ACC39 phase and rms width as derived from the fit for the same ACC39 phase settings as in fig.6.6.

corresponding to the two centre pictures in 6.6 are to be measured. It is of interest whether for these typical accelerator settings the EO monitor faithfully reconstructs the longitudinal electron bunch profile. Thus a comparison measurement using the most precise longitudinal bunch diagnostic tool, the transverse deflecting structure (LOLA), was done. To this end, all further accelerating structures were operated on crest, and the second bunch compressor (BC3) was turned off. In fig. 6.7, the current profiles as acquired by LOLA for the same settings as for the EO measurement in fig 6.6 are depicted, together with gaussian fits estimating their width (an inaccurate procedure chosen for

consistency with the EO bunch langth measurement). The errors shown are derived from the error estimation of the LOLA calibration. For medium long bunches, the deviation from gaussian bunches is not too large, while for the very strong compressed bunch (top picture) with its somewhat more structured shape this is particularly imprecise. The peak current grows significantly from the bottom plot to the top plot. Comparing the EO data and the LOLA data, one finds the length equivalence indicated by the fitted gaussians is very good for the lower three profiles, while the shape is only comparable for the two centre ones (which represent typical accelerator settings).

ACC39 phase	rms width by LOLA	rms width by EO
13.6°	4.03(33) ps	4.0(5) ps
9.3°	2.65(30) ps	2.7(3) ps
3.6°	1.45(20) ps	1.4(1) ps
-0.4°	0.25(6) ps	0.6(1) ps

Table 6.1: Comparison of the electron bunch width as acquired by LOLA and the EO monitor. The first ACC39 phase corresponds to an on crest setting. The widths are derived from gaussian plots for comparability. For the origin of the errors see text.

For a better comparison the bunch profiles as measured by the EO monitor and by LOLA are plotted into the same graph in fig. 6.8 for the used ACC39 phase settings. The LOLA current profiles are plotted in blue (flipped to have the leading part of the bunch on the right), the height adjusted EO data in green. The temporal resolution of the electro-optic bunch monitor is not sufficient to resolve the features of this short bunch, especially the steep leading edge on the right. It rises from 10% to 90% in 250 fs. The corresonding edge of the EO signal has a steepness of more than 1.5 ps. Estimating the resolution of the monitor using the approximation formula $\Delta t \approx 2.6\sqrt{T_0 T_C}$ leads to a value of 1.7 ps as the width of the shortest features that can be resolved using the EO monitor. To further investigate this, the bunch shape reconstruction by electro-optic spectral decoding was simulated for gaussian electron bunches of different rms length. The laser pulse initial width was assumed to be 50 fs (rms) (corresponding to the spectral width of 55 nm FWHM, and accounting for non transform-limited pulses) and the chirped laser pulse width was set to

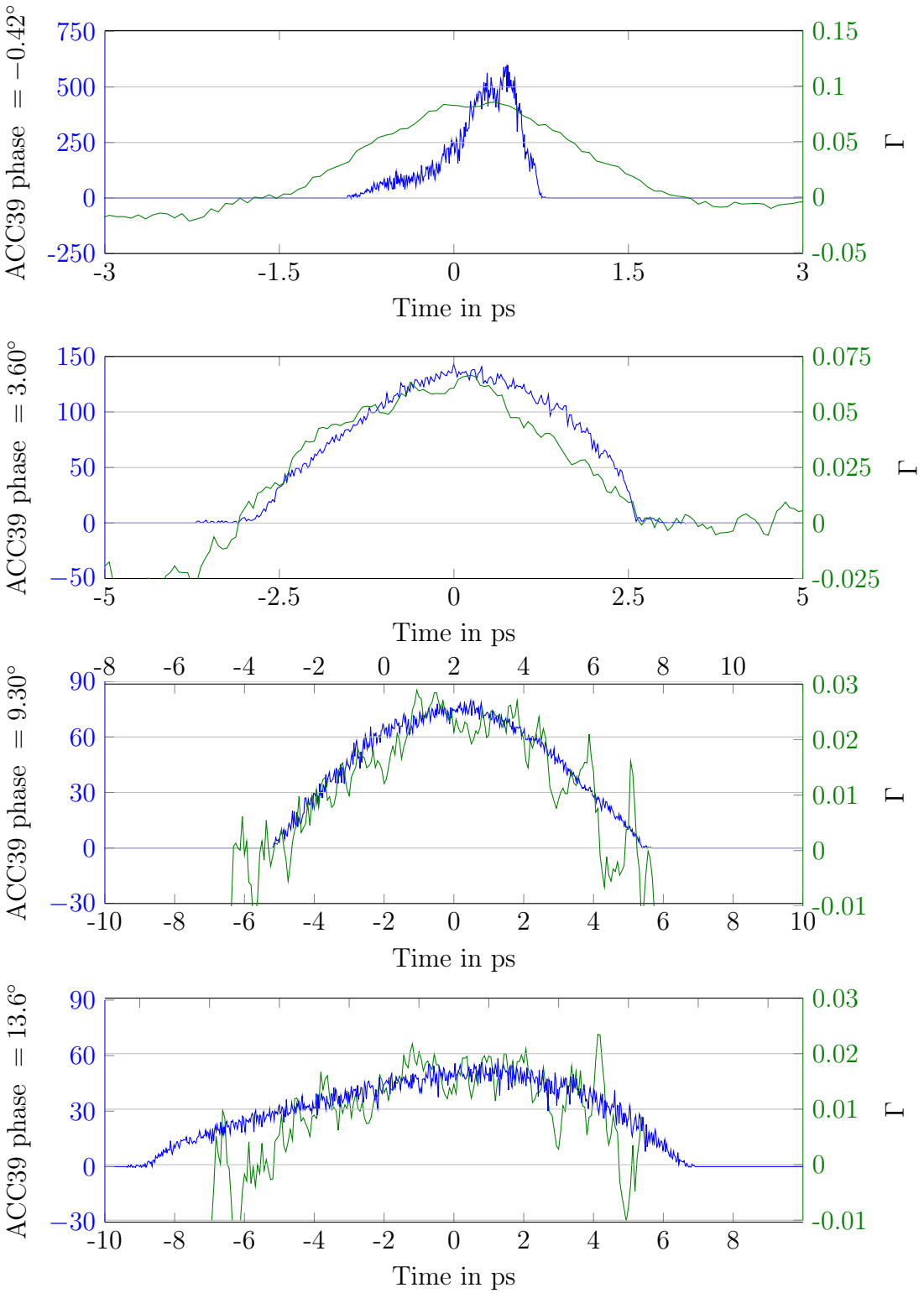

Figure 6.8: Direct comparison of LOLA (blue) and EO (green) measurements, same data as in the before two plots. The shortest bunch is not resolved by the EO monitor. Note the different scales.

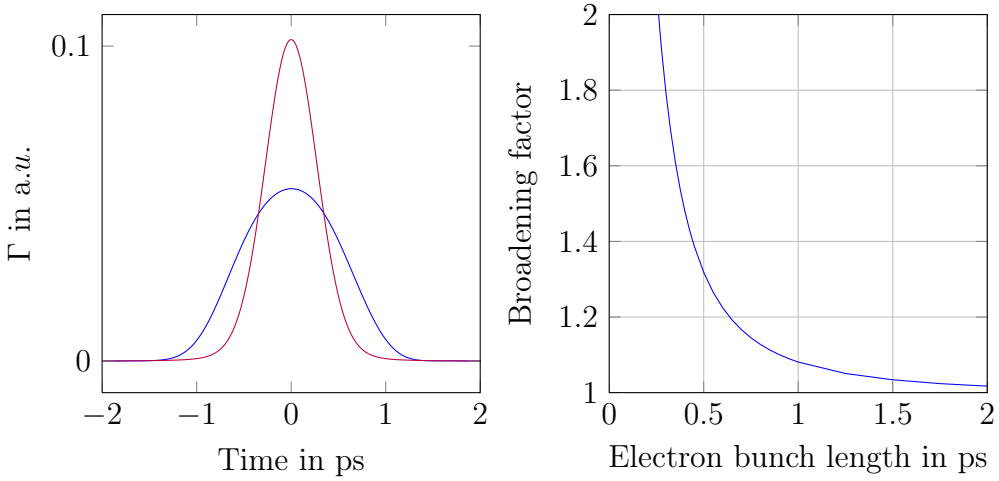

Figure 6.9: Left: calculated phase advance including broaening through frequency mixing (blue) for a gaussian electron bunch with 250 fs rms width. The calculated phase advance has a width of 517 fs rms. Right: Broadening factor by frequency mixing for input electron bunches of different width.

7.2 ps FWHM as measured for this setup. The broadening factor defined by the rms width of the spectral decoding signal divided by the input electron bunch length is plotted over the input electron bunch length. Applying the result of this calculation to the measurement shown above, we find a broadening factor of less than 1.05 for the second shortest electron bunch whose width was determined to 1.4(1) ps rms by the EO monitor in accordance with the LOLA measurement whithin erros bounds. For the shortest bunch we find a broadening factor of ≈ 2.07, which explains the great discrepancy for the EO and the LOLA width value. Interestingly, neither in the simulation nor in the measurement there is a sign of oscillations due to frequency mixing present for the shortest bunch shape reconstruction, in difference to the measurement with the thinner crystal, where bunch features like a rising edge with a steepness well below the resolution capability lead to strong oscillations in the EO signal. Concerning the signal strength a comparison with the equivalent measurement before the crystal exchange lead to grossly the same lower phase advances for a given current [12] as already found in sec. 6.2.2.

Chapter 7

Summary and Outlook

A robust ytterbium-doped fibre laser system with two amplifier stages has been built and commissioned. Besides fullfilling the main specifications of a sufficient pulse energy ($>$ 5 nJ) and spectral width ($>$60 nm), the laser system has proofed to operate with very low frequency noise ($<$200 fs integrated timing jitter in [10 Hz, 54 MHz] when RF locked to the accelerator reference) and amplitude noise (0.07% integrated RIN in [1Hz, 100kHz] before gated amplifier). The self-built laser oscillator is comparable with the purchased YDFL oscillator in terms of optical specifications, reliability and remote controllability. Through its staged amplifier design it is capable of delivering laser pulse trains of widely varying energy, pulse length, and pulse train repetition rate. A range of operating parameters suited for electro-optic spectral decoding experiments has been found maximising the usable spectral bandwidth and pulse energy while minimising the shot-to-shot variation.

A longitudinal electron bunch shape monitor using a commercially available YDFL oscillator has been upgraded and electron bunch measurements where conducted behind the first bunch compressor at FLASH. The usable time window for measurements has been expanded to more than 10 ps. The broadened response to unresolvable short electron bunches ($<$ 1 ps) was measured and is quantitatively understood to be caused by frequency mixing. After the exchange of a defect EO crystal at the EO setup at 140 m, it seems possible to start with electro-optical profile measurements of fully compressed bunches. This is an important step towards a second robust electron bunch monitor, which has originally been one goal of this thesis.

From an accelerator physics point of view, the electro-optic bunch profile measurements for fully compressed bunches are more interesting as these are going to emit light in the SASE process. However, the temporal resolution of spectral decoding setups may be not sufficient for short bunches as are now often desired by FEL users and can not easily be improved as frequency mixing becomes more problematic for shorter bunches. Historically, this approach has been chosen as spectral decoding is rather insensitive to electron bunch arrival time jitter. With the advent of the optical synchronisation system enabling an arrival time feedback acting on the linear accelerator, the arrival time is now stable on the order of 100 fs. Thus, different longitudinal diagnostic approaches using electro-optical methods may be reconsidered. Electro-optic sampling with its simple setup and possibility of balanced detection and high readout rate (photodiodes instead of a camera) may be an useful choice. However, such a setup requires short laser pulses (< 50 fs) that cannot easily be generated by fibre lasers, so the stability of the laser system needs to be adressed again.

In general every diagnostic method or experiment that requires a temporal overlap of the electron bunch with a laser pulse suffers from the problem of establishing this overlap and maintaining it. Diagnostics are especially needed when the accelerator needs to be set up again after a shutdown or a maintenance day. A diagnostic tool that first needs a stable machine to establish this overlap seems of small value. Furthermore the need for ever shorter electron bunches itself and especially the taken route to it using decreasing bunch charges makes it difficult to design electro-optic bunch diagnostics with a sufficient signal-to-noise ratio. Thus, frequency domain diagnostic tools like the CRISP4 THz spectrometer in combination with the TDS (for calibration) may be sufficient for longitudinal bunch profile measurements, even though parasitic measurements are not possible with these devices.

Bibliography

[1] Undulators for SASE FELs. In: *Nuclear Instruments and Methods in Physics Research Section A: Accelerators, Spectrometers, Detectors and Associated Equipment* 445 (2000), Nr. 1-3, S. 366 – 372. – ISSN 0168–9002

[2] Water diffusion and surface structural relaxation of silica glasses. In: *Journal of Non-Crystalline Solids* 288 (2001), Nr. 1â??3, S. 73 – 80. – ISSN 0022–3093

[3] Agrawal, Govind P.: Applications of Nonlinear Fiber Optics. In: *Nonlinear Fiber Optics*. Academic Press San Diego / London (Springer Tracts in Modern Physics). – ISBN 978–0–12–374302–2

[4] Agrawal, Govind P.: Nonlinear Fiber Optics. In: *Nonlinear Fiber Optics*. Academic Press San Diego / London (Springer Tracts in Modern Physics). – ISBN 978–0–12–369516–1

[5] Aune, B. ; Bandelmann, R. ; Bloess, D. ; Bonin, B. ; Bosotti, A. u. a.: The superconducting TESLA cavities. In: *Phys.Rev.ST Accel.Beams* 3 (2000), S. 092001. – Dedicated to the memory of Bjorn H. Wiik

[6] Azima, Armin: *An Electro-Optical Timing Diagnostic for Pump-Probe Experiments at the Free-Electron Laser in Hamburg FLASH*, University of Hamburg, DESY-THESIS-2009-027, June 2009. – Ph.D. thesis

[7] Bartholin, Erasmus: An Accompt of Sundry Experiments Made and Communicated by that Learn'd Mathematician, Dr. Erasmus Bartholin, upon a Chrystal-Like Body, Sent to Him Out of Island. In: *Phil. Trans.* 5 (1670), S. 2039–2048

[8] Bass, M. ; DeCusatis, C. ; Li, G. ; Mahajan, V.N. ; Enoch, J. ; Stryland, E.V. ; America, Optical S.: *Handbook of Optics: Optical properties of materials, nonlinear optics, quantum optics*. McGraw-Hill, 2009 (Handbook of Optics). – ISBN 9780071498920

[9] Baumgartl, M ; Ortaç, B ; Schreiber, T ; Limpert, J ; Tünnermann, A: Ultrashort pulse formation and evolution in mode-locked fiber lasers. In: *Applied Physics B* 104 (2011), Nr. 3, S. 523–536

[10] Behrens, C. ; Schmidt, B ; Wesch, S. ; Nicoletti, D.: Upgrade and Evaluation of the Bunch Compression Monitor at the Free-Electron Laser in Hamburg (FLASH). In: *Proceedings of the IPAC 2010, Kyoto* (2010), S. 912–914

[11] Berden, G. ; Gillespie, W. A. ; Jamison, S. P. ; Knabbe, E.-A. ; MacLeod, A. M. ; Meer, A. F. G. d. ; Phillips, P. J. ; Schlarb, H. ; Schmidt, B. ; Schmüser, P. ; Steffen, B.: Benchmarking of Electro-Optic Monitors for Femtosecond Electron Bunches. In: *Phys. Rev. Lett.* 99 (2007), Oct, S. 164801

[12] Breunlin, Jonas: *Commissioning of an Electro-Optic Bunch Length Monitor at FLASH*. May 2011 DESY-THESIS-2011-017

[13] Burrus, C. A. ; Stone, J.: Nd3+ doped SiO2 lasers in an end-pumped fiber geometry. In: *Applied Physics Letters* 23 (1973), Nr. 7, S. 388–389

[14] Casalbuoni, S. ; Schlarb, H. ; Schmidt, B. ; Schmüser, P. ; Steffen, B. ; Winter, A.: Numerical studies on the electro-optic detection of femtosecond electron bunches. In: *Phys. Rev. ST Accel. Beams* 11 (2008), Jul, S. 072802

[15] Casalbuoni, S. ; Schmidt, B. ; Schmüser, P. ; Arsov, V. ; Wesch, S.: Ultrabroadband terahertz source and beamline based on coherent transition radiation. In: *Phys. Rev. ST Accel. Beams* 12 (2009), Mar, S. 030705

[16] Casalbuoni, S. ; Schmidt, B. ; Schmüser, P. ; Steffen, B.: Far-Infrared Transition and Diffraction Radiation — Part I: Production,

Diffraction Effects and Optical Propagation / DESY (Germany). Hamburg DESY, 2005. – Forschungsbericht

[17] Catani, L. ; Cianchi, A. ; Di Pirro, G. ; Honkavaara, K.: A large distributed digital camera system for accelerator beam diagnostics. In: *Rev. Sci. Instrum.* 76 (2005), S. 073303

[18] Chen, Q. ; Tani, M. ; Jiang, Z. ; Zhang, X.-C.: Electro-optic transceivers for terahertz-wave applications. In: *J. Opt. Soc. Am. B* 18 (2001), Jun, Nr. 6, S. 823–831

[19] Chigusa, Y. ; Yamamoto, Y. ; Yokokawa, T. ; Sasaki, T. ; Taru, T. ; Hirano, M. ; Kakui, M. ; Onishi, M. ; Sasaoka, E.: Low-loss pure-silica-core fibers and their possible impact on transmission systems. In: *Lightwave Technology, Journal of* 23 (2005), nov., Nr. 11, S. 3541 – 3550

[20] Dohlus, M. ; Limberg, T. ; Emma, P.: Bunch compression for linac-based FEL's. Electron bunch length compression. In: *ICFA Beam Dyn. Newslett.* 38 (2005), S. 15–37

[21] Einstein, Albert: Zur Quantentheorie der Strahlung. In: *Phys. Z.* (1917), S. 121–128

[22] Etzel, H. W. ; Gandy, H. W. ; Ginther, R. J.: Stimulated Emission of Infrared Radiation from Ytterbium Activated Silicate Glass. In: *Appl. Opt.* 1 (1962), Jul, Nr. 4, S. 534–536

[23] Faust, W. L. ; Henry, Charles H.: Mixing of Visible and Near-Resonance Infrared Light in GaP. In: *Phys. Rev. Lett.* 17 (1966), Dec, S. 1265–1268

[24] Fiber optics for sale: *http://www.fiberoptics4sale.com/wordpress/basic-optics-for-optical-fiber/.* 2012

[25] Gerth, Ch. ; Wilhelm, A.: Synchroton Radiation Monitor for Bunch-Resolved Beam Energy Measurements at FLASH. In: *DIPAC 2009 Proceedings* (2009), S. 399–401

[26] Gurs, K. ; Müller, R.: Breitband-modulation durch Steuerung der Emission eines optischen Masers (Auskoppelmodulation). In: *Physics Letters* 5 (1963), Nr. 3, S. 179 – 181. – ISSN 0031–9163

[27] Hasegawa, Akira ; Matsumoto, Masayuki: Optical Solitons in Fibers. In: *Optical Solitons in Fibers* Bd. 9. Springer Berlin / Heidelberg, 2003. – ISBN 987–3–540–43695–9

[28] Haus, H.A.: Short pulse Generation. In: *Compact Sources of Ultrashort Pulses*. Cambridge University Press, 1995 (Cambridge Studies in Modern Physics). – ISBN 0–521–46192–8, S. 1–55

[29] Haus, H.A.: Mode-locking of lasers. In: *Selected Topics in Quantum Electronics, IEEE Journal of* 6 (2000), Nov/Dec, Nr. 6, S. 1173 –1185

[30] Haus, H.A. ; Mecozzi, A.: Noise of mode-locked lasers. In: *Quantum Electronics, IEEE Journal of* 29 (1993), mar, Nr. 3, S. 983 –996. – ISSN 0018–9197

[31] Hellwarth, R. W.: Theory of the Pulsation of Fluorescent Light From Ruby. In: *Phys. Rev. Lett.* 6 (1961), Jan, S. 9–12

[32] Hofer, M. ; Fermann, M. E. ; Haberl, F. ; Ober, M. H. ; Schmidt, A. J.: Mode locking with cross-phase and self-phase modulation. In: *Opt. Lett.* 16 (1991), Apr, Nr. 7, S. 502–504

[33] Hofer, M. ; Ober, M.H. ; Haberl, F. ; Fermann, M.E.: Characterization of ultrashort pulse formation in passively mode-locked fiber lasers. In: *Quantum Electronics, IEEE Journal of* 28 (1992), mar, Nr. 3, S. 720 –728

[34] Hoffmann, Matthias C. ; Schulz, Sebastian ; Wesch, Stephan ; Wunderlich, Steffen ; Cavalleri, Andrea ; Schmidt, Bernhard: Coherent single-cycle pulses with MV/cm field strengths from a relativistic transition radiation light source. In: *Opt. Lett.* 36 (2011), Dec, Nr. 23, S. 4473–4475

[35] Ilday, F. ; Buckley, J. ; Kuznetsova, L. ; Wise, F.: Generation of 36-femtosecond pulses from a ytterbium fiber laser. In: *Opt. Express* 11 (2003), Dec, Nr. 26, S. 3550–3554

[36] Ischebeck, Rasmus: *Transverse Coherence of a VUV Free Electron Laser*, University of Hamburg, Ph.D., 2003. – DESY-THESIS-2003-033

[37] Islam, M. N. ; Mollenauer, L. F. ; Stolen, R. H. ; Simpson, J. R. ; Shang, H. T.: Cross-phase modulation in optical fibers. In: *Opt. Lett.* 12 (1987), Aug, Nr. 8, S. 625–627

[38] Jamison, S. P. ; MacLeod, A. M. ; Berden, G. ; Jaroszynski, D. A. ; Gillespie, W. A.: Temporally resolved electro-optic effect. In: *Opt. Lett.* 31 (2006), Jun, Nr. 11, S. 1753–1755

[39] Jeong, Y. ; Sahu, J. ; Payne, D. ; Nilsson, J.: Ytterbium-doped large-core fiber laser with 1.36 kW continuous-wave output power. In: *Opt. Express* 12 (2004), Dec, Nr. 25, S. 6088–6092

[40] Kao, K. C. ; Hockham, G. A.: Dielectric-fibre surface waveguides for optical frequencies. In: *Proc. Inst. Elect. Eng.* (1966), Nr. 7, S. 1151–1158

[41] Komarov, Andrey ; Komarov, Konstantin ; Meshcheriakov, Dmitry ; Amrani, Foued: Polarization dynamics in nonlinear anisotropic fibers. In: *Phys. Rev. A* 82 (2010), Jul, S. 013813

[42] Lederer, S. ; Schreiber, S. ; Michelato, P.M ; Monaco, L. ; Sertore, D.: Photocathode Performance at FLASH. In: *Proceedings of the IPAC '10, TUPE006* (2010), Mar, S. 030705

[43] Leitenstorfer, A. ; Hunsche, S. ; Shah, J. ; Nuss, M. C. ; Knox, W. H.: Detectors and sources for ultrabroadband electro-optic sampling: Experiment and theory. In: *Applied Physics Letters* 74 (1999), Nr. 11, S. 1516–1518

[44] Lim, H. ; Ilday, F. ; Wise, F. W.: Generation of 2-nJ pulses from a femtosecond ytterbium fiber laser. In: *Opt. Lett.* 28 (2003), Apr, Nr. 8, S. 660–662

[45] Limpert, Jens ; Schreiber, T. ; Nolte, S. ; Zellmer, H. ; Tunnermann, T. ; Iliew, R. ; Lederer, F. ; Broeng, J. ; Vienne, G. ; Petersson, A. ; Jakobsen, C.: High-power air-clad large-mode-area photonic crystal fiber laser. In: *Opt. Express* 11 (2003), Apr, Nr. 7, S. 818–823

[46] Loew, G. A. ; Altenmueller, Otto H.: Design and Applications of RF Separator Structures at SLAC. (1965). – Paper presented at the fifth Int. Conf. on High-Energy Accelerators, Frascati, Italy, 1965

[47] Lohl, F. ; Schreiber, S. ; Castellano, M. ; Di Pirro, G. ; Catani, L. u. a.: Measurements of the transverse emittance at the FLASH injector at DESY. In: *Phys.Rev.ST Accel.Beams* 9 (2006), S. 092802

[48] MAIMAN, T. H.: Stimulated Optical Radiation in Ruby. In: *Nature* 187 (1960), S. 493–494

[49] Margalit, M. ; Orenstein, M.: Simulation of passively mode locked lasers, using natural boundary conditions: multi pulse evolution and ordering. In: *Optics Communications* 124 (1996), Nr. 5-6, S. 475–480. – ISSN 0030–4018

[50] Matlis, N. H. ; Bakeman, M. ; Geddes, C. G. R. ; Gonsalves, T. ; Lin, C. ; Nakamura, K. ; Osterhoff, J. ; Plateau, G. R. ; Schroeder, C. B. ; Shiraishi, S. ; Sokollik, T. ; Tilborg, J. van ; Toth, Cs. ; Leemans, W. P.: Ultrafast Diagnostics for Electron Beams from Laser Plasma Accelerators. In: *AIP Conference Proceedings* 1299 (2010), Nr. 1, S. 43–51

[51] Matlis, N. H. ; Plateau, G. R. ; Tilborg, J. van ; Leemans, W. P.: Single-shot spatiotemporal measurements of ultrashort THz waveforms using temporal electric-field cross correlation. In: *J. Opt. Soc. Am. B* 28 (2011), Jan, Nr. 1, S. 23–27

[52] Maurer, Robert D. ; Schultz, Peter C.: Fused Silica Optical Waveguide. (1972), May, Nr. 3659915

[53] McCumber, D. E.: Einstein Relations Connecting Broadband Emission and Absorption Spectra. In: *Phys. Rev.* 136 (1964), Nov, S. A954–A957

[54] McNeil, Brian W. ; Thompson, Neil R.: X-ray free-electron lasers. In: *Nat Photon* (2010), S. 814 – 821. – ISSN 0168–9002

[55] Mears, R. J. ; Reekie, L. ; Juancey, I. M. ; Payne, D. N.: Low-noise Erbium-doped fiber amplifier operating at 1.54 μm. In: *Electronics Letters* 23 (1987), Nr. 19, S. 1026–1028

[56] Mocker, Hans W. ; Collins, R. J.: Mode Competition and self Locking Effects in a Q-Switched Ruby Laser. In: *Applied Physics Letters* 7 (1965), nov, Nr. 10, S. 270–273. – ISSN 0003–6951

[57] Nasu, Hiroyuki ; Okamoto, Hideki ; Mito, Akihiro ; Matsuoka, Jun ; Kamiya, Kanichi: Influence of the OH Content on Second Harmonic Generation from Electrically Polarized SiO_2 Glasses. In: *Japanese Journal of Applied Physics* 32 (1993), Nr. Part 2, No. 3B, S. L406–L407

[58] Nelson, L.E. ; Jones, D.J. ; Tamura, K. ; Haus, H.A. ; Ippen, E.P.: Ultrashort-pulse fiber ring lasers. In: *Applied Physics B: Lasers and Optics* 65 (1997), S. 277–294. – ISSN 0946–2171

[59] Ortaç, B. ; Hideur, A. ; Brunel, M. ; Chartier, T. ; Salhi, M. ; Leblond, H. ; Sanchez, F.: Characterization of an ytterbium-doped double-clad fiber laser passively mode-locked by nonlinear polarization rotation. In: *Applied Physics B: Lasers and Optics* 77 (2003), S. 589–594. – ISSN 0946–2171

[60] Ortaç, B. ; Hideur, A. ; Brunel, M. ; Chédot, C. ; Limpert, J. ; Tünnermann, A. ; Ilday, F. ⋮ Generation of parabolic bound pulses from a Yb-fiber laser. In: *Opt. Express* 14 (2006), Jun, Nr. 13, S. 6075–6083

[61] Paschotta, R.: Noise of mode-locked lasers (Part II): timing jitter and other fluctuations. In: *Applied Physics B: Lasers and Optics* 79 (2004), S. 163–173. – ISSN 0946–2171

[62] Paschotta, R. ; Nilsson, J. ; Tropper, A.C. ; Hanna, D.C.: Ytterbium-doped fiber amplifiers. In: *Quantum Electronics, IEEE Journal of* 33 (1997), jul, Nr. 7, S. 1049 –1056. – ISSN 0018–9197

[63] Peng, Xiao-Yu ; Willi, Oswald ; Chen, Min ; Pukhov, Alexander: Optimal chirped probe pulse length for terahertz pulse measurement. In: *Opt. Express* 16 (2008), Aug, Nr. 16, S. 12342–12349

[64] Prochnow, O. ; Paschotta, R. ; Benkler, E. ; Morgner, U. ; Wandt, D. ; Kracht, D. ; Neumann, J.: Quantum-limited noise performance of an ultrafast Yb all-fiber laser. In: *Lasers and Electro-Optics 2009 and the European Quantum Electronics Conference. CLEO Europe - EQEC 2009. European Conference on*, 2009, S. 1

[65] Schmüser, Peter ; Dohlus, Martin ; Rossbach, Jörg: The Ultraviolet and Soft X-Ray FEL in Hamburg. In: *Ultraviolet and Soft X-Ray Free-Electron Lasers* Bd. 229. Springer Berlin / Heidelberg, 2009. – ISBN 978–3–540–79571–1, S. 1–28

[66] Schulz, Sebastian: *Implementation of the Laser-Based Femtosecond Precision Synchronisation System at FLASH*, Ph.D. thesis, To Be published

[67] Scott, R.P. ; Langrock, C. ; Kolner, B.H.: High-dynamic-range laser amplitude and phase noise measurement techniques. In: *Selected Topics in Quantum Electronics, IEEE Journal of* 7 (2001), jul/aug, Nr. 4, S. 641 –655. – ISSN 1077–260X

[68] Sharping, J.E. ; Fiorentino, M. ; Kumar, P. ; Windeler, R.S.: All-optical switching based on cross-phase modulation in microstructure fiber. In: *Photonics Technology Letters, IEEE* 14 (2002), jan., Nr. 1, S. 77 –79. – ISSN 1041–1135

[69] Snitzer, E.: Optical Maser Action in Nd3+ in a Barium crown Glass. In: *Physical Review Letters* 7 (1961), Nr. 12, S. 444–446

[70] Snitzer, E.: Proposed Fiber Cavities for Optical Masers. In: *Journal of Applied Physics* 32 (1961), Nr. 1, S. 36–39

[71] Snitzer, E. ; Tumminelli, R.: SiO2-clad fibers with selectively volatilized soft-glass cores. In: *Opt. Lett.* 14 (1989), Jul, Nr. 14, S. 757–759

[72] Song, Youjian ; Jung, Kwangyun ; Kim, Hyoji ; Kim, Jungwon: Attosecond-resolution timing jitter characterization of Yb-fiber lasers in

stretched-pulse and self-similar regimes. In: *Lasers and Electro-Optics (CLEO), 2011 Conference on*, 2011, S. 1 –2

[73] Song, Youjian ; Kim, Chur ; Jung, Kwangyun ; Kim, Hyoji ; Kim, Jungwon: Timing jitter optimization of mode-locked Yb-fiber lasers toward the attosecond regime. In: *Opt. Express* 19 (2011), Jul, Nr. 15, S. 14518–14525

[74] Steffen, B. ; Arsov, V. ; Berden, G. ; Gillespie, W. A. ; Jamison, S. P. ; MacLeod, A. M. ; Meer, A. F. G. d. ; Phillips, P. J. ; Schlarb, H. ; Schmidt, B. ; Schmüser, P.: Electro-optic time profile monitors for femtosecond electron bunches at the soft x-ray free-electron laser FLASH. In: *Phys. Rev. ST Accel. Beams* 12 (2009), Mar, S. 032802

[75] Steffen, Bernd: *Electro-Optic Methods for Longitudinal Bunch Diagnostics at FLASH*, University of Hamburg, Ph.D. thesis, 2007. – DESY-THESIS-2007-020

[76] Steffen, B., Müller, F. Schlott, V.: A Compact Single Shot Electro-Optical Bunch Length Monitor for the SwissFEL. In: *DIPAC 2009 Proceedings* (2009), S. 263

[77] Tamura, K. ; Ippen, E. P. ; Haus, H. A. ; Nelson, L. E.: 77-fs pulse generation from a stretched-pulse mode-locked all-fiber ring laser. In: *Opt. Lett.* 18 (1993), Jul, Nr. 13, S. 1080–1082

[78] Tilborg, J. van ; Bakker, D. J. ; Matlis, N. H. ; Leemans, W. P.: Spectral sidebands on a narrow-bandwidth optical probe as a broad-bandwidth THz pulse diagnostic. In: *Opt. Express* 19 (2011), Dec, Nr. 27, S. 26634–26644

[79] Vogel, E. ; Albrecht, C ; Baboi, N. ; Behrens, Ch. ; Delfs, T. ; Eschke, J. ; Gerth, C. ; Hoffmann, M.G. ; Hoffmann, M. ; Hüning, M. ; Jonas, R. ; Kahl, J. ; Kostin, D. ; Kreps, G. ; Ludwig, . F. ; Maschmann, W. ; MuellerC. ; Nommsen, P. ; Rothenburg, J. ; Schlarb, H. ; Schmidt, Ch. ; Sekutowicz, J.K. ; Edwards, H.T. ; Harms, E.R. ; Hocker, A. ; Khabiboulline, T.N. ; Kuhn, M.: Test

and Comissioning of the Thrid Harmonic RF System for FLASH. In: *DIPAC 2010 Proceedings* (2010), S. 3

[80] Wesch, S. ; Schmidt, B. ; Behrens, C. ; Delsim-Hashemi, H. ; Schmüser, P.: A multi-channel THz and infrared spectrometer for femtosecond electron bunch diagnostics by single-shot spectroscopy of coherent radiation. In: *Nuclear Instruments and Methods in Physics Research A* 665 (2011), feb, S. 40–47

[81] Wijnen, Frans J. P. ; Berden, Giel ; Jongma, Rienk T.: A simple optical spectral calibration technique for pulsed THz sources. In: *Opt. Express* 18 (2010), Dec, Nr. 25, S. 26517–26524

[82] Will, Ingo ; Templin, Horst I. ; Schreiber, Siegfried ; Sandner, Wolfgang: Photoinjector drive laser of the FLASH FEL. In: *Opt. Express* 19 (2011), Nov, Nr. 24, S. 23770–23781

[83] Winter, Axel ; Ilday, Ömer F. ; Steffen, Bernd: Femtosecond Yb-Doped Fiber Laser System at 1 μm of Wavelength with 100-nm Bandwidth and Variable Pulse Structure for Accelerator Diagnostics. In: *conference proceedings of the DIPAC 2007, Venice, Italy* (2007)

[84] Wu, Q. ; Zhang, X.-C.: 7 terahertz broadband GaP electro-optic sensor. In: *Applied Physics Letters* 70 (1997), Nr. 14, S. 1784–1786

[85] Wunderlich, Steffen: *Electro-optic sampling of THz pulses at the CTR source at FLASH.* 2012 (tbp)

[86] Zhao, B. ; Tang, D. Y. ; Zhao, L. M. ; Shum, P. ; Tam, H. Y.: Pulse-train nonuniformity in a fiber soliton ring laser mode-locked by using the nonlinear polarization rotation technique. In: *Phys. Rev. A* 69 (2004), Apr, S. 043808

[87] Zhou, Xiangyu ; Yoshitomi, Dai ; Kobayashi, Yohei ; Torizuka, Kenji: Generation of 28-fs pulses from a mode-locked ytterbium fiber oscillator. In: *Opt. Express* 16 (2008), May, Nr. 10, S. 7055–7059

Acknowledgement

Many persons have been involved in this work in the course of the years. I would like to begin with Dr. Bernhard Schmidt, the FLA group leader, who gave me the opportunity to work at FLASH, introduced me to the machine and accelerators in general. He was always helpful and gave guidance to me throughout my time at DESY. I also remember countless discussions with him, as well as with Prof. Dr. Jörg Rossbach and Prof. Dr. Peter Schmüser, that were of great help. Dr. Axel Winter showed me the fibre laser basics to start with, and Dr. Vladimir Arsov helped me making first steps in the field of electro-optic bunch detection, while Dr. Florian Löhl told me much about accelerators in general and laser synchronisation in particular.

The technical staff was of uttermost importance for this experimental work. The FLA technicians Matthias Hoffmann and Albert Schleiermacher, assisted by Karol and Amir, lead by the group's engineer Kai Ludwig, did great work on several occasions (as well as Bernd Beyer in the first year). Problems with cameras and servers were solved fast and reliable by Vladimir Rybnikov and Gerhard Schlesselmann. Support in many ways came from Ingrid Nikodem, who always knew how to address DESY difficulties, Ursula Djuanda, who cared about computer and network problems, and Iris Kerkhoff, who often helped. Thanks go to Dr. Axel Knabbe for him insisting on laser safety issues but even more for interesting after-dinner discussions.

Thanks also go to the LBSynch team (Laser Based Synchronisation) under the lead of Dr. Holger Schlarb. I benefited from their knowledge on hardware, from their software, and their understanding of optical fibres. I would like to mention Karl-Heinz Matthiesen (piezo driver), Patrick Gessler and Pavel Predki (RF lock server), Thorsten Lamb and Matthias Felber (Lots of things) seperately.

Working together with the FLASH team is a great thing itself, I would like to thank Dr. Siegfried Schreiber and Dr. Katja Honkavaara as representatives for the many others that make the machine operation possible and that are always open for questions and discussions. I owe much to my FLA PhD fellows, Sebastian Schulz in particular, Marie-Kristin Bock, Stephan Wesch, Christopher Behrens, Eugen Hass, and Steffen Wunderlich. We shared quite a time here. Special thanks go to my EO fellows, Dr. Bernd Steffen, without whom this work would not exist, and Jonas Breunlin, with whom I enjoyed a productive and interesting time.

As it came to finish this thesis I have to thank Dr. Bernhard Schmidt and Prof. Dr. Günther Huber for their rendered expert opinion on the thesis, again Dr. Bernhard Schmidt and Dr. Jens Osterhoff for their delivered expert opinion on the thesis defense, and Dr. Georg Steinbrück, the leader of the thesis defense examination comittee.

There is not only work in life, and I want to thank my parents who supported my little family and me during this time. It made a great difference. Tremendous support came from my wife. She endured the ups and downs, respected odd working times, and was always willing to take care of our children when I needed to be at FLASH. Our wonderful daughters where my main motivation to keep on track and to finish this PhD thesis.